On the Modelization of Optical Devices

From Dielectric Cavities to Radiating Structures

Mémoire

Joey Dumont

Maîtrise en physique
Maître ès sciences (M.Sc.)

Québec, Canada

Résumé

Premièrement, nous allons explorer la modélisation des cavités diélectriques bidimensionnelles. Plus spécifiquement, nous allons développer différentes méthodes de modélisation valides pour des cavités diélectriques à géométrie et profil d'indice de réfraction arbitraires. Ce degré de liberté supplémentaire pourra être utilisé dans le design de microcavités pour des applications spécifiques. Un formalisme de diffusion permettra de définir les modes caractéristiques de ce type de structure et d'en calculer les résonances. Une analyse numérique des équations résultantes montrera que les méthodes intégrales sont possiblement meilleures que les méthodes différentielles.

Deuxièmement, nous discuterons de la modélisation de structures radiatives. Nous utiliserons les méthodes développées dans la section précédente pour modéliser les propriétés lasers des microcavités bidimensionnelles prédites par la théorie SALT. Nous aborderons aussi la modélisation de fibres-antennes RF, plus particulièrement les câbles coaxiaux à perte radiative, dans le but d'intégrer des fonctionnalités radio dans un textile de manière transparente à l'utilisateur.

Abstract

In this essay, we will develop different modelization techniques valid for bidimensional dielectric cavities having arbitrary geometries and refractive index profiles and provide a way to accurately compute the resonances of such structures. The refractive index thus becomes an additional design variable for dielectric cavities. A numerical analysis of of the underlying equations of the theory will reveal that perhaps it is best to forego differential equations in favour of integral ones for the scattering problem.

In the second part, we will discuss the modelization of radiating structures. Using the formalism developed in the previous section, we will study the lasing properties of bidimensional cavities using the newly developed *self-consistent* ab initio *laser theory* (SALT). We will also touch on the modelization of the class of antenna known as *leaky coax* antennas, whose purpose are to be seamlessly integrate radio functionality onto textile.

Table of Contents

List of Figures

List of Tables

Dedicated to my wife, Jessica, for all her love.

education, *n*. That which discloses to the wise and disguises from the foolish their lack of understanding.

The Devil's Dictionary
Ambrose Bierce

Notation

Mathematical Operators

Symbol	Definition
$\sum_m$	Sum over all angular momenta in two dimensions, $m = -\infty \dots \infty$.
$\sum_{\ell,m}$	Sum over all angular momenta in three dimensions, $\ell = 0 \dots \infty$, $m = -\ell \dots \ell$.
$\sum_{\sigma,\ell,m}$	Sum over all spinorial angular momenta in three dimensions.
$\operatorname*{\mathbin{\mathrm{K}}}_{m=1}^{\infty}\left(\frac{a_m}{b_m}\right)$	Continued fraction expansion with coefficients a_m and b_m.
$\lfloor x \rfloor$	Floor function. Maps x to the largest previous integer.
$\lceil x \rceil$	Ceiling function. Maps x to the smallest following integer.
$\langle x \rangle$	Average value of quantity between brackets.
$\mathrm{corr}(X, Y)$	Pearson correlation between samples X and Y.

Vectors and Matrices

Symbol	Definition
$\boldsymbol{V}$, $\boldsymbol{\nu}$	Vectors (bold and italic, uppercase and lowercase).
V_i, ν_i	ith component of vector.
$\langle\alpha\vert$, $\vert\beta\rangle$	Bra-ket notation. Roughly equivalent to row and column vectors, respectively.
$\mathbf{M}$	Matrix (bold uppercase)
M_{ij}	Element on ith row and jth column. $(j + iN)$th element of matrix (row-major ordering) where N is the number of columns. The indices start at 0.
$S_{mm'}$, $Q_{mm'}$	Element of matrices in the 2D angular momentum basis. Indices span $m, m' \in \{-M_{\max} \dots M_{\max}\}$.
$g_{\mu\nu}$	Metric tensor. Indices span only the spatial coordinates, i.e. no time coordinate.
$[\alpha\beta, \gamma]$	Christoffel symbol of the first kind.
$\Gamma^{\alpha}{}_{\beta\gamma}$	Christoffel symbol of the second kind.

Electromagnetism

Symbol	Definition
$\boldsymbol{E}$, $\boldsymbol{D}$, $\boldsymbol{P}$	Electric field, electric displacement and polarization.
$\boldsymbol{H}$, $\boldsymbol{B}$, $\boldsymbol{M}$	Magnetic field, magnetic induction and magnetization.
$\boldsymbol{j}$, ρ	Current and charge densities.
$\boldsymbol{\chi}_{e,m}(\boldsymbol{r}, \boldsymbol{r}', t, t')$	Electric/magnetic tensorial susceptibility.
$\epsilon = \epsilon' + i\epsilon''$	Electric permittivity of a material. We often separate its real and imaginary parts as shown.
μ	Magnetic permeability of a material.
$n = \sqrt{\epsilon\mu}$	Refractive index of a material.
σ_e	Electric conductivity of a material.

Special Functions

Symbol	Definition
$J_\nu(z)$	Bessel function of the first kind of order ν.
$Y_\nu(z)$	Bessel function of the second kind of order ν.
$H_\nu^{(\pm)}(z)$, $H_\nu^{(\omega)}(z)$	Hankel functions of the first and second kind of order ν ($\omega = \pm$).
$j_\nu, y_\nu, h_\nu^{(\omega)}$	Spherical Bessel functions. Given by $c_\nu(z) = \sqrt{\pi/2z}C_{n+1/2}(z)$, where $C_\nu(z)$ is any Bessel function.
$U(a, b, z)$	Kummer's function, also known as the confluent hypergeometric function of the first kind, with parameters a, b.
$P_\ell^m(z)$	Legendre polynomials. Eigenfunctions of the azimuthal part of the free Helmholtz equation.
$Y_{jm}^{\ell S}$	Tensor spherical harmonics. Eigenfunction of the angular part of the free Helmholtz equation for the scattering of spin-S particles.
$\boldsymbol{Y}_{jm}^{\ell}$	Vector spherical harmonics. Eigenfunction of the angular part of the free Helmholtz equation for the scattering of photons.
$C^{j_3 m_3}_{j_1 m_1, j_2 m_2}$	Clebsch-Gordan coefficients.
$\begin{pmatrix} j_1 & j_2 & j_3 \\ m_1 & m_2 & m_3 \end{pmatrix}$	Wigner $3j$-symbols.
$\begin{Bmatrix} j_1 & j_2 & j_3 \\ j_4 & j_5 & j_6 \end{Bmatrix}$	Wigner $6j$-symbols.

Angular Momentum

Ordering of angular momentum in 2D. We consider both positive and negative angular momentum, so the matrices have size $2M+1 \times 2M+1$ where M is the maximum angular momentum.

$$\mathbf{V}\boldsymbol{\psi} = \begin{array}{c} \\ - \\ m\ 0 \\ + \end{array} \overset{\overset{m'}{\overset{-\quad 0 \quad +}{\longleftrightarrow}}}{\begin{pmatrix} \ddots & & \iddots \\ & V_{-1-1}\ V_{-10}\ V_{-11} & \\ & V_{0-1}\ V_{00}\ V_{01} & \\ & V_{1-1}\ V_{10}\ V_{11} & \\ \iddots & & \ddots \end{pmatrix}} \begin{pmatrix} \vdots \\ \psi_{-1} \\ \psi_0 \\ \psi_1 \\ \vdots \end{pmatrix}$$

Ordering of angular momenta ℓ, m in 3D. This block structure allows the product

$$\sum_{\ell'=0}^{\infty} \sum_{m'=-\ell'}^{\ell'} V_{\ell m,\ell' m'} \psi_{\ell' m'}$$

to be written using a single index $\nu = (\ell, m)$. The matrices have size $(\ell_{\max}+1)^2 \times (\ell_{\max}+1)^2$.

$$\mathbf{V}\boldsymbol{\psi} = \begin{array}{c} \\ \ell=0 \\ \ell=1 \end{array} \overset{\overset{\overbrace{\ell'=0}\quad \overbrace{m'=-\ell',\ldots,\ell'}}{}}{\begin{pmatrix} V_{00,00} & V_{00,1-1} & V_{00,10} & V_{00,11} \\ V_{1-1,00} & V_{1-1,1-1} & \vdots & \vdots \\ V_{10,00} & \cdots & \ddots & \vdots \\ V_{11,00} & \cdots & \cdots & \ddots \end{pmatrix}} \begin{pmatrix} \psi_{00} \\ \psi_{1-1} \\ \psi_{10} \\ \psi_{11} \\ \vdots \end{pmatrix}$$

Glossary

Boundary conditions Conditions on the values of the solution and its normal derivative on specific parts of the domain of definition of the solution. They are necessary to make the PDE well-posed and thus uniquely solvable.

Dirichlet The value of the solution is specified on the boundary of the domain. 2

Robin A linear combination of the solution and its normal derivative is specified on the boundary of the domain. 3

calibration phase (algorithms) Wherein a numerical algorithm is tested against a problem with a known solution. Oftentimes, convergence properties of the algorithm are determined using this (usually) trivial scenario. 29

Gerschgorin circles Gerschgorin's theorem states that the eigenvalues of a matrix $\mathbf{A} \in \mathbb{C}^{n\times n}$ fall inside the circles whose centers are the diagonal elements of the matrix $\mathbf{A}$ and whose radii are given either the sums of the absolute values of the associated non-diagonal row/column elements, whichever is smallest. See main text for details. 24

last scattering surface (LSS) Fictitious surface that encloses the scattering potential. In quantum scattering, since the potential usually decreases as $r^{-1-\epsilon}$, it is a sphere whose radius tends to infinity. In electromagnetic scattering, the potential is zero outside the cavity region; the LSS is then the smallest sphere that encloses the cavity region. The LSS can be any closed surface, but it is easier to work with spheres, as the differential equations usually separate on this surface first. 13, 14, 16, 48, 53, 76, 84, 88

Q-matrix (**Q**-matrix) Time-delay matrix. Related to the scattering matrix. It describes the energy derivative of the phase shift between the incoming and outgoing field, which can be linked to a time delay due to the interaction with the scatterer. 7, 11, 17, 19, 20, 35, 36, 43, 67, 76

S-matrix (**S**-matrix) Scattering matrix. In quantum scattering, relates the asymptotes of the incoming field to the asymptotes of the scattered field. For real potentials, this amounts to the phase shifts between them. In electromagnetic scattering, relates the outgoing parts of the field to the incoming parts of it outside a *last scattering surface* which encloses the whole of the scatterer. It thus contains both near- and far-field information. 3, 7, 11, 14, 15, 19, 20, 23, 28, 29, 41, 42, 67, 68, 84

Acronyms

ARC asymmetric resonant cavity. 4, 32, 34

FDTD finite-difference time-domain. 47, 52

FEM finite element method. 5, 37, 47, 52

LCX leaky coax antenna. xi, 5, 37, 49, 51–53, 59

PDE partial differential equation. 42

RWA rotating wave approximation. 40

SALT steady-state *ab initio* laser theory. 4, 15, 37, 38, 40

SIA stationary inversion approximation. 40

SQA the **S**- and **Q**-matrix algorithm. 20, 21, 30, 36, 38, 76

SVEA slowly varying envelope approximation. 40

Foreword

This essay, even though the front page claims that it is mine alone, is actually the product of a number of people without who it could not have existed[†]. First and foremost, I must acknowledge the constant support and trust of Pr. Louis J. Dubé, the head of our little research group we lovingly call Dynamica. Without his calm disposition, sharp mind and seemingly infinite knowledge, I could not have done it. In the two years I have been part of the group, he has helped me grow both personally and intellectually. I also thank my co-supervisor, Younès Messaddeq, for making this essay possible. Lastly, I wish to thank Pr. Reinhold Blümel; his infectious enthusiasm and deep understanding of physics have spawned many great ideas.

I also want to thank a former member of Dynamica, Guillaume Painchaud-April, whose footsteps I have tried to follow. Despite the fact that he had already left the group when I joined, the conversations we had have helped make it through this journey. Denis Gagnon deserves a special mention for teaching me all the tricks in the trade of being a student researcher. His quick wit, his determination to see things through (however trivial they might be) and his friendly demeanour have made him both an excellent tutor and a fast friend. It goes without saying that all the other members of Dynamica have been instrumental in the making of this essay, and I thank them each individually: Antoine Allard, Jean-Luc Déziel, Laurent Hébert-Dufresne, Edward Laurence and Jean-Gabriel Young, thank you.

These acknowledgments would not be complete without mentioning my family. I want to thank my parents for their understanding, their support and for encouraging my never-ending curiosity. I also want to thank my parents-in-law, whose support have enabled the completion of many a crazy project, including this work. Most of all, however, I want to thank my wife, Jessica Cournoyer, whose support and understanding have been heavily solicited in the last few years. Your love and support have been invaluable in the writing of these words.

Joey Dumont
July 10th, 2014

[†]Of course, any issue that comes up is fully mine!

Contributions This short section humbly presents my contributions to the literature in the form of both conference proceedings and peer-reviewed journal articles.

Peer-Reviewed Journal Articles

[1] J.-L. Déziel, **J. Dumont**, D. Gagnon, L. J. Dubé, S. Messaddeq and Y. Messaddeq, "Toward the formation of cross-superposed laser-induced periodic surface structures," arXiv:1410.0583.

[2] D. Gagnon, **J. Dumont**, J.-L. Déziel and L. J. Dubé, "Optimization of integrated polarization filters," Opt. Lett. **39**, 5768–5771 (2014). doi:10.1364/OL.39.005768.

[3] D. Gagnon, **J. Dumont**, J.-L. Déziel and L. J. Dubé, "Ab initio investigation of lasing thesholds in photonic molecules," J. Opt. Soc. Am. B **31**, 1867–1873 (2014). doi:10.1364/JOSAB.31.001867.

[4] D. Gagnon, **J. Dumont** and L. J. Dubé, "Multiobjective optimization in integrated photonics design," Opt. Lett. **38**, 2181–2184 (2013). doi:10.1364/OL.38002181.

[5] D. Gagnon, **J. Dumont** and L. J. Dubé, "Beam shaping using genetically optimized two-dimensional photonic crystals," J. Opt. Soc. Am. A **29**, 2673–2678 (2012). doi:10.1364/JOSAA.29.002673

Conference Proceedings

[6] D. Gagnon, **J. Dumont**, J.-L. Déziel and L. J. Dubé[i],
"Adding SALT to coupled microcavities: the making of active photonic molecule lasers,"
in IEEE Proceedings of the 16th International Conference on Transparent Optical Networks (ICTON 2014). arXiv:1405.0168

[7] G. Painchaud-April, **J. Dumont**[ii], D. Gagnon and L. J. Dubé,
"*S* and *Q* matrices reloaded: applications to open, inhomogeneous, and complex cavities,"
in IEEE Proceedings of the 15th International Conference on Transparent Optical Networks (ICTON 2013). doi:ICTON.2013.6602811.

[8] D. Gagnon[iii], **J. Dumont** and L. J. Dubé,
"Coherent beam shaping using two-dimensional photonic crystals,"
in IEEE Proceedings of the 15th International Conference on Transparent Optical Networks (ICTON 2013). doi:ICTON.2013.6602751.

[9] D. Gagnon[iv], **J. Dumont** and L. J. Dubé,
"Optimization in optical systems revisited: beyond genetic algorithms,"
in Bull. Am. Phys. Soc., **58**(6), 2013. BAPS.2013.DAMOP.D1.14

[i] Speaker at this invited talk.
[ii] Speaker at this invited talk.
[iii] Speaker at this regular talk.
[iv] Poster presentation

Chapter 1

Introduction

Ipsa scientia potestas est.

Sir Francis Bacon

Our story begins, as most stories do, with a simple premise. Circa 1878, John William Strutt, Third Baron Rayleigh – Lord Rayleigh, for short – observed a peculiar phenomena in St Paul's Cathedral: a small whisper, uttered from one side of the circular gallery, could be heard quite clearly by anyone seated along the outer edge of the gallery and even travel back to the ears of the whisperer. To explain his observation, Lord Rayleigh borrowed from geometrical optics and modeled the sound waves as packets, or particles, of sound that undergo specular reflection upon contact with the wall [10, §287]. This picture, akin to the trajectories of billiard balls, allowed him to conclude that "sonorous vibrations have a tendency to cling to a concave surface". His billiard analysis is later complemented by a complete wave analysis wherein he shows that the equation of aerial vibrations, essentially Helmholtz's equation, admit solutions of the form

$$\psi_n(r,\theta,t) = J_n(kr)\cos(kat - n\theta)$$

and that most of the amplitude, for a certain range of parameters (specifically, $n \gg kr$), is concentrated within an annulus near the boundary of the gallery [11], further proving his explanation. He also noted that his derivation held for electrical waves if the walls were perfect conductors. He termed this phenomenon the whispering-gallery phenomenon and, today, we call this type of waves whispering-gallery waves.

Our journey thus begins on the wings of the whisper, forever gliding along the concave surface of a perfectly smooth wall. However, no journey worth recounting happens without any bumps in the road.

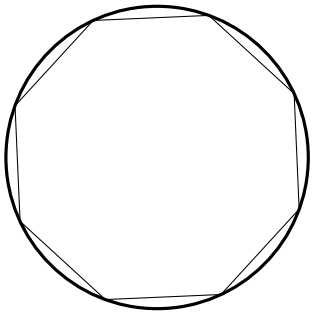

(a) Closed cavity with a WGM of quantum number $m = 8$.

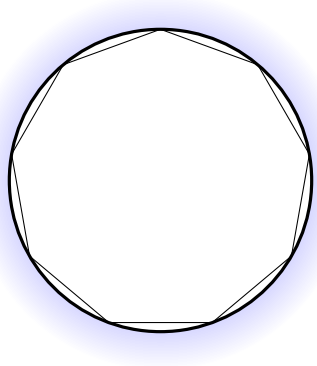

(b) Open cavity with a WGM of quantum number $m = 9$.

Figure 1.1 – Schematic representation of whispering-gallery modes in closed and open resonators. In closed resonators, WGMs have infinite lifetimes as they cannot interact with the external world. In open cavities, evanescent leakage (represented by the blue glow), implies interaction with the environment, which implies finite modal lifetime.

1.1 The Study of Passive Dielectric Microcavities

For the better part of the 20$^{\text{th}}$ century, the whispering-gallery phenomenon remained only a matter of curiosity [12]. It was brought back to light in the mid-1980s when it was realized that *dielectric resonators* had the potential to attain unparalleled electromagnetic energy storage capabilities via the use of whispering-gallery modes (WGM) [13]. Research in this area increased exponentially when their application as extremely sensitive biosensors was theoretically explored and later experimentally achieved [14–18].

The whispering-gallery phenomenon in dielectric media can be explained via the same basic physics as the whispering gallery of St Paul's Cathedral, but with a crucial difference: the mechanism by which the light (or sound) is confined. Both the cathedral and the metallic sphere described by Lord Rayleigh as known as *closed cavities*: the whisper does not leave the interior of the gallery, as the electric field does not leave the confines of its metallic prison due to the perfect reflections at the boundary. The walls of the cavity do not allow the waves to penetrate their depth. On the other hand, dielectric cavities retain light by way of *total internal reflection*, which implies the existence of an evanescent wave normal to the boundary, which in turn allows the wave to leak, or couple, to the exterior of the cavity. This has multiple experimental and theoretical consequences, which we will explore in this essay.

Mathematically, closed cavities usually obey Helmholtz's equation

$$\left[\nabla^2 + k^2\right]\psi = 0 \qquad \psi(\boldsymbol{r} \in \mathscr{C}) = 0 \tag{1.1}$$

where ψ is the oscillation (pressure field, electric field, etc.) and $\mathscr{C}$ is the boundary of the cavity. This partial differential equation, together with the Dirichlet boundary condition, translate to an

eigenvalue problem: solutions only exist for a discrete set of eigenvalues k_n. These closed cavities have been a testbed for theoretical and experimental endeavours in the last three decades, as can be seen from the great amount of work done in the fields of quantum chaos and random matrix theory (RMT), for instance. Quantum chaos attempts to classify the chaotic eigenstates of systems with non-separable Schrödinger equations using the underlying (semi-)classical mechanics of the cavity [19, 20]. The associated billiard of these systems may be regular or chaotic, depending on the particular form that the boundary of the system, $\mathscr{C}$, takes. Research in this area helps to define the classical-quantum transition. Level-spacing statistics of closed cavities also provides a way to classify the eigenstates, depending on the statistical ensemble the cavity falls into.

Closed cavities, are, however, an idealization of the much more realistic open cavity. The discrete states of the former exist indefinitely inside the cavity; they have an infinite lifetime. They thus have infinite energy storage capabilities, but are impossible to generate. Open cavities, which also obey Helmholtz equation, but with the Sommerfeld radiation condition (a Robin boundary condition)

$$\lim_{r\to\infty} r^{\frac{d-1}{2}}\left(\frac{\partial}{\partial r} - ik\right)\psi = 0 \tag{1.2}$$

have a continuum of solutions. A countably infinite set of resonances can be defined for those cavities. These resonances have finite lifetimes. The lifetimes are usually quantitatively described by the quality factor, or Q-factor, which is defined via the positions of the resonances in the complex k-plane

$$Q = \frac{\mathrm{Re}\left\{k_p\right\}}{\left|2\mathrm{Im}\left\{k_p\right\}\right|} \tag{1.3}$$

and can be interpreted as the time it takes the light to escape the cavity. Experimentally, it is related to the finesse of the resonance. In an experimental scattering event, the transmission spectrum shows a Lorentzian dip of width $\delta\lambda$. The Q-factor can thence also be written

$$Q = \frac{\delta\lambda}{\lambda}. \tag{1.4}$$

An incoming field from infinity can interact with the modes of the cavity and then escape the confines of the cavity. The *time-delay* introduced by the interaction is linked to the lifetime of the modes of the cavity.

This rather pictorial viewpoint can be made formal by the use of *scattering theory*, in which we suppose that a field, coming from infinity, suffers some changes due to its interaction with the cavity and escapes to infinity once again. The object that we will consider is the scattering matrix, which describes the relationship between the field after the interaction and the field before the interaction, i.e. it describes the effect of the potential on an incoming field. The scattering approach allows us to define the modes of open cavities, a problem that is perhaps more complicated that it seems [21–23].

Open dielectric cavities also allow a semi-classical approximation, mathematically obtained by letting the wavelength λ to be very small compared to the characteristic lengths involved in the

system, or $k \to \infty$. The resulting open billiard can and has been used to engineer the cavities to specific purposes [24]. The fact that the resulting system is Hamiltonian (but not necessarily Hermitian) has been used to study open quantum systems and non-Hermitian quantum mechanics experimentally [25–31]. This stems from the similarities between the Helmholtz and Schrödinger equations. Since the billiard system is Hamiltonian, one can set up a phase space with Birkhoff coordinates [32, 33]. Using the Husimi [34] transform, this can be used to test the phase-space formulation of quantum mechanics [35].

Most applications of open dielectric cavities urge the use of very high Q resonances. In WGM biosensors, the Q value dictates the performance of the sensor via (1.4); in microlasers, it means a better field enhancement; in cavity QED, higher Q and lower mode volumes make it possible to study the quantum effects of light-matter interaction. It is possible to experimentally obtain values of $Q \sim 10^7 - 10^9$ using highly symmetrical cavity designs [16, 36, 37]. This symmetry implies that the far-field emission is also symmetric: it is isotropic. For some applications, such as some designs of WGM biosensors, this may be fine. However, for lasing applications, one would like to have, simultaneously, high-Q and directionality in the far-field emission. The duality of those two concepts is one of the many facets of the study of asymmetric resonant cavities (ARCs), dielectric cavities that are parametrically deformed versions of the circular cavity. This allows a certain degree of freedom in the design of microcavities and has lead to interesting phenomena, such as exceptional points [38–41], avoided crossings [42], Goos-Hänchel shift [43] and Anderson localization [44] among others.

In this essay, we will use a second degree of freedom in the design by allowing the refractive index distribution to be completely arbitrary inside the cavity. This new degree of freedom can be realized experimentally by the use of nematics [45]. Moreover, we will see that the numerical methods developed in this context could also be used to better model the lasing operation of active dielectric cavities.

The metaphorical "bumps in the road" become literal bumps in the boundary $\mathscr{C}$ of the cavity and in the refractive index profile inside the cavity.

1.2 Onwards to Radiating Structures

The expertise developed in the study of dielectric cavities is then extended to lasing cavities and proposed for arbitrary 3D structures. We will touch upon the modelization of active dielectric cavities with the use of steady-state *ab initio* laser theory (SALT) which, as its name hints, provides a steady-state model for the behaviour of the active medium. The particular set of approximations used allow to model the population dynamics of quantum N-level systems as a static, but possibly spatially-varying and non-linear, modification of the refractive index of the passive cavity. In the linear case, basis expansions methods (such as the ones we use) can be applied. We will develop a more stable numerical method based on the Lippmann-Schwinger version of Helmholtz's equation.

We will also discuss the application of the method to arbitrary 3D structures. We will attempt to model a type of antennae called LCXs. Their highly non-trivial geometry and the specifics of their experimental realization will make our method rather hard to implement in that case. We will thus use all-numerical methods to extract the necessary information. Proper introduction to this project will be given later.

1.3 Content of this Essay

In first chapter of this essay, we detail our work on open dielectric cavities with arbitrary refractive index profiles. We generalize a scattering method by G.P.-A. [46] for complex refractive indices and TE polarization. We first describe the analytical formalism and develop some of the scattering theory that is needed. We then discuss the development and numerical implementation of the solution of Helmholtz's equation in inhomogeneous cavities. We then showcase the method by analyzing a circular microcavity with a Gaussian deformation of its refractive index.

The second chapter discuss the extension to lasing structures and briefly discusses the Lippmann-Schwinger method. We then model a family of LCXs with the finite element method (FEM). Most of the work done aims at conciliating the experimental and theoretical data sets, mainly by explaining the source of the discrepancy. The effects of several physical parameters were thus explored.

Chapter 2

Passive Media

> Le savant n'étudie pas la nature parce que cela est utile; il l'étudie parce qu'il y prend plaisir et il y prend plaisir parce qu'elle est belle. Si la nature n'était pas belle, elle ne vaudrait pas la peine d'être connue, la vie ne vaudrait pas la peine d'être vécue.
>
> Henri Poincaré, Science et méthode, 1908.

This chapter is devoted to the study of light propagation in dielectric bidimensional cavities. Starting from Maxwell's equations, we derive approximate differential equations that govern the wave behaviour in cavities having spatially-varying refractive index profiles (henceforth referred to as *inhomogeneous cavities*). This set of reduced equations serves as the basis for a semi-analytical solution method that uses the quantum machinery of the scattering matrix **S**-matrix and its associated time-delay matrix (**Q**-matrix) to yield information about the cavity modes. The numerical implementation of the method is discussed and and is then demonstrated for a selected set of microcavities.

2.1 Maxwell's Equations for Bidimensional Cavities: Reduction from 3D to 2D

2.1.1 Setting the Stage

As with any problem in optics, we start from Maxwell's equations. Although this specific chapter focuses on dielectric cavities, we will show Maxwell's equations in their full generality, as we will later study problems with currents and sources. We use the Lorentz-Heaviside set of units with the speed of light, c, equal to 1 to obtain [47]

$$\nabla \times \boldsymbol{E}(\boldsymbol{r},t) + \frac{\partial \boldsymbol{B}(\boldsymbol{r},t)}{\partial t} = 0 \tag{2.1a}$$

$$\nabla \times \boldsymbol{H}(\boldsymbol{r},t) - \frac{\partial \boldsymbol{D}(\boldsymbol{r},t)}{\partial t} = \boldsymbol{j}_s(\boldsymbol{r},t) + \boldsymbol{j}_c(\boldsymbol{r},t) \tag{2.1b}$$

$$\nabla \cdot \boldsymbol{D}(\boldsymbol{r},t) = \rho(\boldsymbol{r},t) \tag{2.1c}$$

$$\nabla \cdot \boldsymbol{B}(\boldsymbol{r},t) = 0 \tag{2.1d}$$

where $\boldsymbol{E}$ is the electric field, $\boldsymbol{D}$ the electric displacement, $\boldsymbol{H}$ the magnetic field, $\boldsymbol{B}$ the magnetic induction and where $\boldsymbol{j}$ and ρ are the current and charge densities, respectively. The distinction between a source current, $\boldsymbol{j}_s$ and an induced conduction current, $\boldsymbol{j}_c$, is arbitrary but will prove conceptually useful when dealing with radiating structures. In this essay, we will generally take $\rho = 0$ and $\boldsymbol{j}_s = \boldsymbol{0}$ as there will be no physical charges/currents in our problems.

This very general set of equations does not make any assumption on the properties of the medium in which the fields exist: it is, therefore, almost impossible to solve. To properly model the effect of different media, we introduce the usual constitutive relations:

$$\boldsymbol{D}(\boldsymbol{r},t) = \boldsymbol{E}(\boldsymbol{r},t) + \boldsymbol{P}(\boldsymbol{r},t) \tag{2.2a}$$

$$\boldsymbol{B}(\boldsymbol{r},t) = \boldsymbol{H}(\boldsymbol{r},t) + \boldsymbol{M}(\boldsymbol{r},t) \tag{2.2b}$$

where the effects of the medium are accounted for in $\boldsymbol{P}$ and $\boldsymbol{M}$, the polarization and magnetization fields, respectively. In the time domain, the effect of the electric (magnetic) field on the polarization (magnetization) can be written as

$$\boldsymbol{P} = \iiiint \boldsymbol{\chi}_e(\boldsymbol{r},\boldsymbol{r}',t,t';\boldsymbol{E}) \cdot \boldsymbol{E}(\boldsymbol{r}',t') d^3\boldsymbol{r}' dt' + \boldsymbol{P}^{NL} \tag{2.3a}$$

$$\boldsymbol{j}_c = \iiiint \boldsymbol{\sigma}_e(\boldsymbol{r},\boldsymbol{r}',t,t';\boldsymbol{E}) \cdot \boldsymbol{E}(\boldsymbol{r}',t') d^3\boldsymbol{r}' dt' + \boldsymbol{j}_c^{NL} \tag{2.3b}$$

$$\boldsymbol{M} = \iiiint \boldsymbol{\chi}_m(\boldsymbol{r},\boldsymbol{r}',t,t';\boldsymbol{H}) \cdot \boldsymbol{H}(\boldsymbol{r}',t') d^3\boldsymbol{r}' dt' + \boldsymbol{M}^{NL} \tag{2.3c}$$

where $\boldsymbol{\chi}_{e,m}$ are the electric and magnetic tensorial susceptibilities and $\boldsymbol{\sigma}_e$ the tensorial electric conductivity. They are written here as (possibly non-linear) response functions. We will take the

nonlinear magnetization and induced current, $\boldsymbol{M}^{NL}$ and $\boldsymbol{j}_c^{NL}$, to be identically zero. While $\boldsymbol{P}^{NL}$ is usually reserved for the nonlinear polarization, we will use it to denote the effect of a gain medium, whether it is nonlinear or not.

While it is possible to compute these quantities from first principles using statistical mechanics techniques, this is a highly complicated topic that we will not delve into. We will consider local, causal and isotropic (although possibly spatially varying) responses. The tensorial response functions become scalar and their spatial dependence is given by a three dimensional Dirac δ-function. This allows us to write the constitutive relations in the much simpler form

$$\boldsymbol{P} = \int_0^\infty \chi_e(\boldsymbol{r}, t')\boldsymbol{E}(\boldsymbol{r}, t-t')dt' + \boldsymbol{P}^{NL} \tag{2.4a}$$

$$\boldsymbol{j}_c = \int_0^\infty \sigma_e(\boldsymbol{r}, t')\boldsymbol{E}(\boldsymbol{r}, t-t')dt' \tag{2.4b}$$

$$\boldsymbol{M} = \int_0^\infty \chi_m(\boldsymbol{r}, t')\boldsymbol{H}(\boldsymbol{r}, t-t')dt' \tag{2.4c}$$

where the integration limits follow from the causality requirement. Substituting these results into the Maxwell equations and and using the Fourier transform yields the set[1]

$$\nabla \times \boldsymbol{E}(\boldsymbol{r}, \omega) - i\omega\mu(\boldsymbol{r}, \omega)\boldsymbol{H}(\boldsymbol{r}, \omega) = 0 \tag{2.5a}$$

$$\nabla \times \boldsymbol{H}(\boldsymbol{r}, \omega) + i\omega\epsilon(\boldsymbol{r}, \omega)\boldsymbol{E}(\boldsymbol{r}, \omega) = -i\omega\boldsymbol{P}^{NL}(\boldsymbol{r}, \omega) \tag{2.5b}$$

where $\mu = 1 + \chi_m$ is the permeability and $\epsilon = 1 + \chi_e - \sigma/i\omega$ the permittivity. In the remainder of this essay, we will concerned by the solution of this precise set of equations. We also recall the *electromagnetic boundary conditions* associated with a discontinuous jump in the permeability or permittivity [48, 49]

$$\hat{\boldsymbol{n}} \cdot (\boldsymbol{B}_2 - \boldsymbol{B}_1) = 0, \qquad \hat{\boldsymbol{n}} \times (\boldsymbol{E}_2 - \boldsymbol{E}_1) = 0, \tag{2.5c}$$

$$\hat{\boldsymbol{n}} \times (\boldsymbol{H}_2 - \boldsymbol{H}_1) = \boldsymbol{K}, \qquad \hat{\boldsymbol{n}} \cdot (\boldsymbol{D}_2 - \boldsymbol{D}_1) = \Sigma \tag{2.5d}$$

where $\boldsymbol{K}$ and Σ are current and charge surface densities, respectively. These types of boundary conditions are known as *transmission conditions* [50].

2.1.2 Dimension Reduction

In this section we derive the differential equations for the electromagnetic field in an infinitely long dielectric cylinder of arbitrary cross-section and arbitrary physical parameters ϵ and μ. There is no gain medium. Consequently, $\boldsymbol{P}^{NL} = \boldsymbol{K} = \Sigma \equiv 0$ in our previous equations. We also require longitudinal symmetry, i.e. that the geometry and physical parameters do not depend on z.

[1] Notice that, in our system of units, $\omega = k$ and thus we will make use of frequency and wavenumber interchangeably. We will also suppress all explicit frequency dependence from our notation, as it rapidly becomes cumbersome. Also, even though the $\boldsymbol{H}$ field was introduced as an auxiliary field to take into account the effect of an applied magnetic field to the material, we take it as the fundamental field as it leads to more easily solvable equations and is a completely equivalent choice.

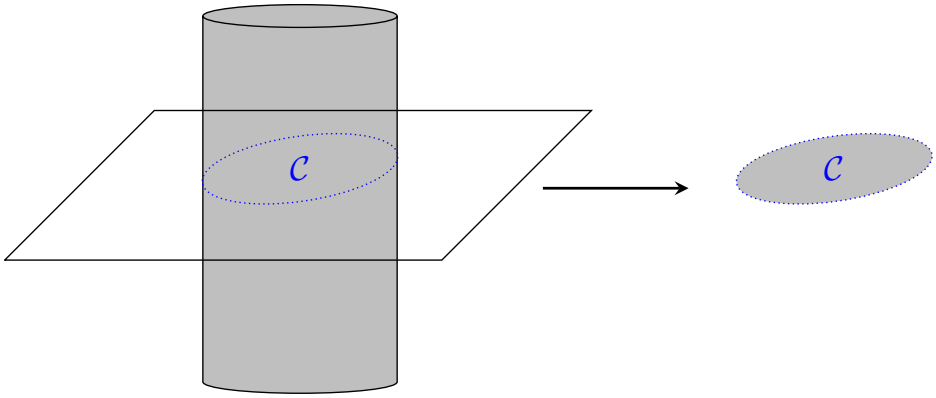

Figure 2.1 – Our set of equations will be valid for infinitely long cylinders of arbitrary cross-sections (shown on the left) and arbitrary physical parameters ϵ and μ. Our cavities, however, are bidimensional (shown on the right). The dimension reduction thus consists in postulating independence of the fields and physical and geometrical parameters of the cavity with regards to the longitudinal coordinate and choosing a particular plane $\partial\Omega$.

To this effect, it will be useful to separate the field in transverse and longitudinal components. Following [49, 51], we suppose that the fields can be written as

$$\begin{Bmatrix} \boldsymbol{E}(\boldsymbol{r}_\perp, z) \\ \boldsymbol{H}(\boldsymbol{r}_\perp, z) \end{Bmatrix} = \begin{Bmatrix} \boldsymbol{E}(\boldsymbol{r}_\perp) \\ \boldsymbol{H}(\boldsymbol{r}_\perp) \end{Bmatrix} e^{i\beta z} \tag{2.6}$$

and we will also separate the fields and differential operators in two parts

$$\boldsymbol{E}(\boldsymbol{r}_\perp) = \boldsymbol{E}_\perp + E_z\hat{\boldsymbol{z}}; \qquad \nabla = \nabla_\perp + \hat{\boldsymbol{z}}\frac{d}{dz}. \tag{2.7}$$

Substitution in (2.5a) yields

$$ik\mu H_z = (\nabla_\perp \times \boldsymbol{E}_\perp)_z \qquad -ik\epsilon E_z = (\nabla_\perp \times \boldsymbol{H}_\perp)_z \tag{2.8}$$

$$ik\mu \boldsymbol{H}_\perp = (-i\beta \boldsymbol{E}_\perp + \nabla_\perp E_z) \times \hat{\boldsymbol{z}} \qquad -ik\epsilon \boldsymbol{E}_\perp = (-i\beta \boldsymbol{H}_\perp + \nabla_\perp H_z) \times \hat{\boldsymbol{z}} \tag{2.9}$$

The symmetry of these equations allow the decoupling of the tranverse and longitudinal components. Solving the system (2.9) shows that the scalar components H_z and E_z are the fundamental ones, as we can write the tranverse fields as a function of the longitudinal ones:

$$\boldsymbol{E}_\perp = \frac{i}{k^2n^2 - \beta^2}\left[\beta\nabla_\perp E_z + k\mu\nabla_\perp H_z \times \hat{\boldsymbol{z}}\right] \tag{2.10a}$$

$$\boldsymbol{H}_\perp = \frac{i}{k^2n^2 - \beta^2}\left[-k\epsilon\nabla_\perp E_z \times \hat{\boldsymbol{z}} + \beta\nabla_\perp H_z\right]. \tag{2.10b}$$

Derivation of the differential equation for E_z and H_z can be done via equations (2.8), but is quite cumbersome. The details are thus not shown in this essay.

More specific boundary conditions can be derived with the use of these equations. Applying the tranverse and longitudinal decomposition on (2.5c) yields the six boundary conditions

$$E_{z1} = E_{z2} \qquad H_{z1} = H_{z2}$$
$$E_{t1} = E_{t2} \qquad H_{t1} = H_{t2}$$
$$\epsilon_1 E_{n1} = \epsilon_2 E_{n2} \qquad \mu_1 H_{n1} = \mu_2 H_{n2}$$

We seek to write the boundary conditions as a function of H_z and E_z, given that they are the fundamental fields. This can be done by taking the projections of the transverse fields:

$$E_t = \hat{\boldsymbol{t}} \cdot \boldsymbol{E}_\perp = \frac{i}{\gamma^2}\left[\beta \partial_t E_z - k\mu \partial_n H_z\right] \tag{2.11a}$$
$$E_n = \hat{\boldsymbol{n}} \cdot \boldsymbol{E}_\perp = \frac{i}{\gamma^2}\left[\beta \partial_n E_z + k\mu \partial_t H_z\right] \tag{2.11b}$$
$$H_t = \hat{\boldsymbol{t}} \cdot \boldsymbol{H}_\perp = \frac{i}{\gamma^2}\left[k\epsilon \partial_n E_z + \beta \partial_t H_z\right] \tag{2.11c}$$
$$H_n = \hat{\boldsymbol{n}} \cdot \boldsymbol{H}_\perp = \frac{i}{\gamma^2}\left[-k\epsilon \partial_t E_z + \beta \partial_n H_z\right] \tag{2.11d}$$

where $\partial_{t,n}$ are the transverse and normal derivatives, respectively, and $\gamma^2 = k^2 n^2 - \beta^2$. Substituting these results in the boundary conditions for the transverse and normal components, we can derive the conditions $\partial_t E_{z1} = \partial_t E_{z2}$, $\partial_t H_{z1} = \partial_t H_{z2}$, which can shown to be equivalent to the continuity of the longitudinal components, *viz.* (2.11a) [51]. Combining all our previous results yields the four independent boundary conditions:

$$E_{z1} = E_{z2} \tag{2.12a}$$
$$H_{z1} = H_{z2} \tag{2.12b}$$
$$\frac{k\mu_1}{\gamma_1^2}\frac{\partial H_{z1}}{\partial n} - \frac{k\mu_2}{\gamma_2^2}\frac{\partial H_{z2}}{\partial n} = \beta\left(\frac{1}{\gamma_1^2} - \frac{1}{\gamma_2^2}\right)\frac{\partial E_{z1}}{\partial t} \tag{2.12c}$$
$$\frac{k\epsilon_1}{\gamma_1^2}\frac{\partial E_{z1}}{\partial n} - \frac{k\epsilon_2}{\gamma_2^2}\frac{\partial E_{z2}}{\partial n} = -\beta\left(\frac{1}{\gamma_1^2} - \frac{1}{\gamma_2^2}\right)\frac{\partial H_{z1}}{\partial t}. \tag{2.12d}$$

Notice that the propagation constant couples the electric and magnetic fields, regardless of the physical and geometrical parameters of the cavity.

2.2 Scattering Matrix Formalism

The previous section has provided us with the differential equations that we will need to solve to properly model bidimensional cavities. In this section, we will set up a scattering matrix (**S**-matrix) formalism, augmented by the time-delay matrix (**Q**-*matrix*) that will allow us to quantify the response of the cavities to an applied field and provide us with a novel way to determine their resonances. The numerical implementation of the method, being somewhat problematic, will be discussed at length.

2.2.1 **S** and **Q** Matrices Reloaded

In dielectric cavities, we need to solve the following equations

$$\left\{\nabla^2+k^2n^2\left[1-\left(\frac{\beta}{kn}\right)^2\right]\right\}\begin{Bmatrix}H_z\\E_z\end{Bmatrix}=\frac{1}{1-\left(\frac{\beta}{kn}\right)^2}\left[\frac{1}{\epsilon}\begin{Bmatrix}\nabla H_z\\\nabla E_z\end{Bmatrix}\cdot\nabla\epsilon+\frac{1}{\mu}\begin{Bmatrix}\nabla H_z\\\nabla E_z\end{Bmatrix}\cdot\nabla\mu\right]$$
$$-\begin{pmatrix}\frac{1}{\mu}&0\\0&\frac{1}{\epsilon}\end{pmatrix}\begin{Bmatrix}\nabla H_z\cdot\nabla\mu\\\nabla E_z\cdot\nabla\epsilon\end{Bmatrix}+\frac{\beta/kn}{1-\left(\frac{\beta}{kn}\right)^2}\left[\left(\sqrt{\frac{\mu}{\epsilon}}+\sqrt{\frac{\epsilon}{\mu}}\right)\begin{pmatrix}0&-\frac{1}{\mu}\\\frac{1}{\epsilon}&0\end{pmatrix}\begin{Bmatrix}\nabla H_z\times\nabla\mu\\\nabla E_z\times\nabla\epsilon\end{Bmatrix}\right] \tag{2.13}$$

where β is the propagation constant in the longitudinal direction. Inhomogeneous cavities do not obey Helmholtz's equation like homogeneous cavities do, but depend upon the first-order derivatives of the fields and physical properties of the medium. The two longitudinal fields couple through the last term, where an anti-diagonal matrix appears.

In fact, this set of equations describe the propagation of light in optical fibers of arbitrary cross-section and arbitrary refractive index profiles. However, we are interested in the modes that are confined on a two-dimensional surface, the cavity modes. These modes must be independent of z and we therefore take $\beta=0$. This is the main approximation of our model. It has been shown to hold only approximately in experimental conditions [25, 52], but we take the resulting equations to be the exact ones. This allows a simpler analysis for qualitative exploration; quantitative agreement could be reached via perturbation methods or by using the integral method we flesh out in Appendix B.2. This approximation has the much appreciated benefit of decoupling both the field equations and the boundary conditions (see (2.12)).

Additionally exploiting the fact that we will only consider non-magnetic media ($\mu=1$, $\epsilon=n^2$), our equation set becomes

$$\left[\nabla^2+k^2n^2\right]H_z=\frac{2}{n}\nabla H_z\cdot\nabla n \tag{2.14a}$$
$$\left[\nabla^2+k^2n^2\right]E_z=0. \tag{2.14b}$$

In the following, it will be advantageous to form the field $\boldsymbol{h}=\boldsymbol{H}/n$ [38]. This yields the equation [38, 46]

$$\left[\nabla^2+k^2n^2-\frac{2(\nabla n)^2}{n^2}+\frac{\left(\nabla^2 n\right)}{n}\right]h_z=0 \tag{2.14a'}$$

which is nothing but Helmholtz equation with an additional potential term.

(a) The Quantum Connection Before putting forward the scattering formalism, it is interesting to digress a little and explore the connection between the optical world and the quantum world. Specifically, the scalar version of Maxwell's equations, the Helmholtz equations above, can be written as a Schrödinger equation

$$\left[\nabla^2+k^2\right]\psi=k^2\left(n_0^2-n_c^2(r,\theta)\right)\psi-V(\boldsymbol{r}) \tag{2.15}$$

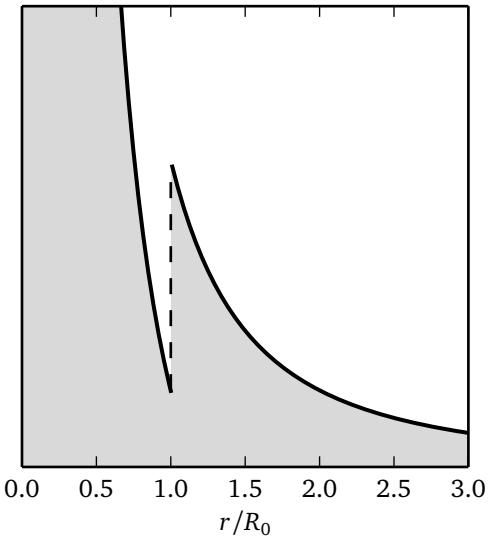

Figure 2.2 – Effective radial potential associated with the homogeneous, circular cavity. We show the potential for $kR_0 = 5$, $m = 10$ and $n_c = 2$.

where $V(\boldsymbol{r})$ is the additional potential term just mentioned. If the r.h.s. is such that equation is amenable to a solution by separation of variables, one obtains a radial potential of the form

$$V_{\text{eff}}(r) = k^2(n_0^2 - n_c^2(r)) + \frac{m^2 - 1/4}{r^2} - V(r). \tag{2.16}$$

For instance, the homogeneous, circular cavity yields a potential as seen in Fig. 2.2. The jump at the boundary allows the existence of quasi-bound (QB) states inside the cavity, as opposed to bound states, as the light can tunnel outside the potential barrier.

It is worth mentioning that the TM polarized waves behave exactly as quantum wavefunctions do, the field and its normal derivative being continuous at the interface, while the TE waves are akin to sonorous vibrations, as they may also obey "jump" conditions at an interface [50]. Because of this, the TM polarization is more present in the microcavities literature than the TE one.

We now return to the solution of the differential equations. We will adopt a scattering viewpoint. Imagine that the dielectric cavity with boundary $\mathscr{C}$ an refractive index profile $n_c = n_c(r, \theta)$ inside $\mathscr{C}$ is embedded in an infinite medium of constant refractive index $n_o = \sqrt{\epsilon\mu}$, as seen in Fig. 2.3. Outside the cavity, $\boldsymbol{r} \notin \mathscr{C}$, the r.h.s. of (2.14) vanish. We call the surface that bounds the support of the function $n_o^2 - n_c^2$ the last scattering surface (LSS). The resulting equations are Helmholtz's and therefore have the well-known solution

$$\psi = \sum_m \left[A_m H_m^{(-)}(nkr) + B_m H_m^{(+)}(nkr)\right] e^{im\theta} \qquad (r > R_0). \tag{2.17}$$

where $H_m^{(\pm)}(z)$ are the Hankel functions of the first and second kind. The Hankel functions are chosen in lieu of their usual homologues $J_m(z)$ and $Y_m(z)$ as their asymptotic forms have incom-

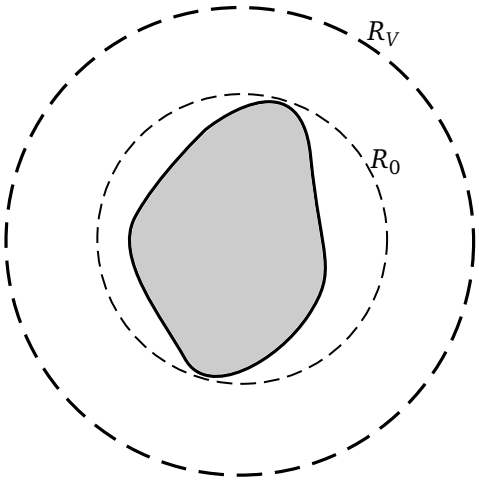

Figure 2.3 – Geometry of a dimensional cavity. R_0 is the radius of the smallest circle that encloses the physical microcavity, i.e. the last scattering surface. R_V is the radius of a fictitious circle that we will take to go to infinity.

ing/outgoing cylindrical wave character, $H_m^{(\pm)} \propto \exp(\pm ikr)/\sqrt{r}$, thus ensuring that the Sommerfeld radiation condition is fulfilled. The scattering viewpoint essentially describes the relationship between the outgoing coefficients, B_m, and the incoming coefficients, A_m, via the *scattering matrix*

$$B_m = \sum_{m'} S_{mm'} A_{m'}. \tag{2.18}$$

Much like its quantum-mechanical counterpart, the electromagnetic scattering matrix can be interpreted as a phase shift acquired by the incoming waves through interaction with the potential. This is most easily seen by considering a central potential $V(r)$ where the **S**-matrix is diagonal. In that case, the mth component of the far-field can be written as

$$\psi_m^{\mathrm{FF}} \propto \frac{1}{\sqrt{r}} \left[e^{-ikr} + e^{i\delta_m} e^{ikr} \right] \tag{2.19}$$

where we have written $S_{mm} = e^{i\delta_m}$ with $\delta_m \in \mathbb{R}$ as per the unitarity condition. The non-diagonal elements $S_{mm'}$ describe the coupling between angular momenta $m \to m'$ and can be interpreted as transition probabilities.

When the **S**-matrix is defined by the pair (2.17) and (2.18), it contains all near- and far-field information. This is sharp contrast with the usual quantum scattering matrix, which is usually defined for a last scattering surface having $r \to \infty$, i.e. in the far-field [53–55]. In the scattering off dielectric structures, the potential $n_0^2 - n_c^2$ has compact support in $\mathbb{R}^d$ and the last scattering surface is taken to be a $(d-1)$-sphere containing the support of the potential.

In most applications (see the Introduction), we wish to find the *resonances* of the cavity. This is usually done by enforcing Sommerfeld radiation conditions on Helmholtz's equation and looking for solutions of

$$\mathbf{S}^{-1}\boldsymbol{B} = 0; \tag{2.20}$$

for which a solution exists only if $|\det \mathbf{S}(k)| \to \infty$, i.e. at a pole of the **S**-matrix. For real potentials, there cannot exist a solution on the real k line because of the flux conservation (unitarity) property of the **S**-matrix. We must extend the search to the complex k plane.

Equation (2.20) shows that the cavity *creates* energy from nothing. In more physical terms, the cavity has an infinite response to an infinitesimal energy input. This definition of a resonance implies that we should look in the $\mathrm{Im}\{k\} < 0$ half-plane for the poles of the **S**-matrix. The solutions to this equation are known as QB states as their intensity is usually larger in the vicinity of the cavity and, contrary to their truly bound counterparts, have a small but non-zero value outside it. The ever so slowly decaying wavefunction is thus non-normalizable (i.e. $\psi \notin L^2$). In this formulation, the field even has the following non-physical behaviour in the far-field

$$\begin{aligned}\psi_{\mathrm{FF}}(\boldsymbol{r},t) &= \psi(\boldsymbol{r})e^{-i\omega t} \\ &\propto \exp\left[i(k'-ik'')r\right]\exp\left[-i(k'-ik'')t\right]\exp[im\theta] \\ |\psi_{\mathrm{FF}}(\boldsymbol{r},t)|^2 &\propto e^{2k''r}e^{-2k''t}\end{aligned}$$

where $k = k'-ik''$. The field thus exponentially increases with r, but exponentially *decreases* with t. We can see, however, that the time scale of the exponential decrease is linked to the imaginary part of the wavenumber by $\tau = \left(2k''\right)^{-1}$. We will use this relationship later in this essay.

It is interesting to note that the kind of resonances supported by dielectric cavities are of the same kind as those supported by a forced, undamped harmonic oscillator. The incoming wave field plays the part of the applied force. In the treatment of harmonic oscillators, it is usually noticed that adding a friction term in the equations curbs the infinities that the model otherwise yields. A parallel situation occurs in dielectric cavities. When there is no absorption losses (friction), the response of the cavity to an incoming wave field is a result of the cumulative effect of the experimentally unattainable complex poles of the scattering matrix. However, when losses/gain are added into the model, the poles of the scattering matrix begin to move in the complex plane; loss of unitarity implies that it is possible that these poles may eventually move to the real k-line, making them experimentally feasible. This is in fact the backbone of the SALT [56, 57].

Instead of directly looking for the poles, we will look for the signatures of these poles on the real k line by computing the *energy* of the modes and their complex coupling. This part of the formalism was initially developed by G.P.-A. [46]: we will repeat only what is necessary.

Recall that the average electromagnetic energy of a field in a given volume V

$$\mathscr{E}^V = \frac{1}{2}\iiint_V \left[\epsilon \boldsymbol{E}^* \cdot \boldsymbol{E} + \mu \boldsymbol{H}^* \cdot \boldsymbol{H}\right] d^3\boldsymbol{r}. \tag{2.21}$$

We form the energy matrix

$$\mathscr{E}^V_{mm'} = \frac{1}{2}\iiint_V \left[\epsilon \boldsymbol{E}^*_m \cdot \boldsymbol{E}_{m'} + \mu \boldsymbol{H}^*_m \cdot \boldsymbol{H}_{m'}\right] d^3\boldsymbol{r}. \tag{2.22}$$

We will carry out the rest of the computation for the TM mode ($H_z = E_r = E_\theta = 0$); the argument holds for TE polarization *mutatis mutandis* because of the k-independence of the additional potential term in (2.14a') and also because $\boldsymbol{h} \propto \boldsymbol{H}$ outside the last scattering surface. We thus have

$$\boldsymbol{E} = \psi \hat{\boldsymbol{z}}$$
$$\boldsymbol{H} = \frac{1}{ik} \nabla \times \boldsymbol{E}$$

and the energy matrix becomes

$$\mathscr{E}^V_{mm'} = \frac{1}{2} \iiint_V \left[n^2 \psi^*_m \psi_{m'} + \frac{1}{k^2} (\nabla \times \psi_m \hat{\boldsymbol{z}}) \cdot \left(\nabla \times \psi^*_{m'} \hat{\boldsymbol{z}} \right) \right] d^3 \boldsymbol{r} . \tag{2.23}$$

Taking the parametric derivative of Helmholtz' equation, we get the following relations

$$\left[\nabla^2 + n^2 k^2 \right] \psi = 0 \tag{2.24a}$$
$$\left[\nabla^2 + n^2 k^2 \right] \psi^* = 0 \tag{2.24b}$$
$$\nabla^2 \frac{\partial \psi}{\partial k} + 2kn^2 \psi + n^2 k^2 \frac{\partial \psi}{\partial k} = 0 \tag{2.24c}$$

where we assume a real potential. Forming the product[2]

$$\begin{aligned} \frac{1}{2k} \nabla \cdot \left[\frac{\partial \psi}{\partial k} \nabla \psi^* - \psi^* \nabla \frac{\partial \psi}{\partial k} \right] &= \frac{1}{2k} \left[\nabla \psi^* \cdot \nabla \frac{\partial \psi}{\partial k} + \frac{\partial \psi}{\partial k} \nabla^2 \psi^* - \nabla \frac{\partial \psi}{\partial k} \cdot \nabla \psi^* - \psi^* \nabla^2 \frac{\partial \psi}{\partial k} \right] \\ &= \frac{1}{2k} \left[n^2 \psi^* \left(2k\psi + k^2 \frac{\partial \psi}{\partial k} \right) - \frac{\partial \psi}{\partial k} n^2 k^2 \psi^* \right] \\ &= n^2 \psi^* \psi \end{aligned}$$

to write the energy matrix as

$$\mathscr{E}^V_{mm'} = \frac{1}{4k} \int_V \nabla \cdot \left\{ \frac{\partial \psi_{m'}}{\partial k} \nabla \psi^*_m - \psi^*_m \nabla \frac{\partial \psi_{m'}}{\partial k} + \frac{2}{k} \left[\psi_{m'} \hat{\boldsymbol{z}} \times \nabla \times \psi^*_m \hat{\boldsymbol{z}} \right] \right\} d^3 \boldsymbol{r}$$

Using the divergence theorem, noting that the normal vector is the radial vector, we obtain

$$\mathscr{E}^V_{mm'} = \frac{wR_V}{4k} \int_0^{2\pi} \left(\frac{\partial \psi_{m'}}{\partial k} \frac{\partial \psi^*_m}{\partial r} - \psi^*_m \frac{\partial^2 \psi_{m'}}{\partial k \partial r} \right) d\theta + \frac{wR_V}{2k} \int_0^{2\pi} \psi_{m'} \frac{\partial \psi^*_m}{\partial r} d\theta$$

[2] We use the identities [48, Appendix II]

$$\nabla \cdot (\phi \boldsymbol{A}) = \boldsymbol{A} \cdot \nabla \phi + \phi \nabla \cdot \boldsymbol{A}.$$

and

$$(\boldsymbol{a} \times \boldsymbol{b}) \cdot (\boldsymbol{c} \times \boldsymbol{d}) = \boldsymbol{a} \cdot [\boldsymbol{b} \times (\boldsymbol{c} \times \boldsymbol{d})] .$$

Using the exterior solution for ψ_m and using the asymptotic expressions (A.16c) for the Hankel functions, we get (after some algebra)

$$\mathscr{E}^{\infty}_{mm'} = \lim_{R_V \to \infty} \left[\frac{4n_0 w R_V}{k} + \mathscr{O}(R_V^{-1}) \right] \delta_{mm'} + \frac{4w}{k} \left(-i \sum_{\ell} S^*_{\ell m} \frac{\partial S_{\ell m'}}{\partial k} \right) \tag{2.25}$$

where w is the thickness of the cavity. The first term is the diverging energy of the beam. Given that the incoming and outgoing waves are of infinite extent, this divergence is only natural. The second term, however, depends only the potential and can be interpreted as an excess energy due to the cavity [46]. In matrix notation, we have

$$\mathbf{Q} = -i\mathbf{S}^{\dagger} \frac{d\mathbf{S}}{dk}. \tag{2.26}$$

This result coincides with the **Q**-matrix of quantum mechanics [58]. The interpretation of this matrix is facilitated by (2.19). Using the central potential, we can write

$$Q_{mm} = -ie^{-i\delta_m} \left(i \frac{\partial \delta_m}{\partial k} \right) e^{i\delta_m} = \frac{\partial \delta_m}{\partial k}. \tag{2.27}$$

The **Q**-matrix thus corresponds to the energy derivative of the phase shift, which has long been associated with the time-delay introduced by the potential [58–63].

The keen reader will have noticed that the above derivation fails for complex potentials. The author has not found a proper derivation for the extension to complex potentials. However, an expression can be found by this heuristic argument: when the potential is complex, the phase shift δ_m becomes a complex function of k. In the preceding expression, we should take the inverse of the scattering matrix, not its Hermitian transpose, to reproduce the energy derivative of the phase shift. We thus have

$$\mathbf{Q} = -i\mathbf{S}^{-1} \frac{d\mathbf{S}}{dk} \tag{2.28}$$

as the proper generalization. This form was also used by Smith in [58]. It is possible to arrive at this result with our derivation, but with the extra term

$$-ik \iint_{\mathscr{C}} \mathrm{Im}\left\{ n^2(r,\theta) \right\} \psi^*_m \frac{\partial \psi_{m'}}{\partial k} d^2\boldsymbol{r} \tag{2.29}$$

where $\mathscr{C}$ is the cavity region and the support of $\mathrm{Im}\left\{ n^2(r,\theta) \right\}$. A similar result was obtained in [64] where it was shown that this augmented **Q**-matrix shares some properties of the Wigner-Smith time-delay matrix (2.26). We will derive some of these properties below.

2.2.2 Properties of the **S** and **Q** matrices

The **S**-matrix has multiple symmetries which can be used either to verify numerical implementations or to help tame numerical divergence issues. Most of the symmetries we will expose in this thesis will concern the analytical continuation of the scattering matrix in the complex k plane.

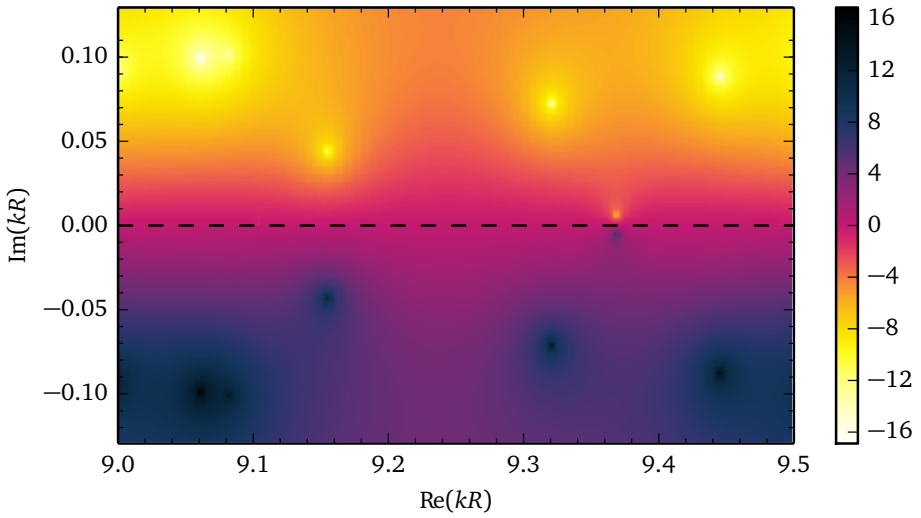

Figure 2.4 – Mirror symmetry of the scattering matrix. For this example, we computed $\log|\det \mathbf{S}(k)|$ for the scattering matrix of the circular, homogeneous cavity with $n_c = 3.2$ and $n_o = 1$.

It is well known that the $\mathbf{S}$-matrix is unitary for real values of n and k [55, 65]. However, it loses this important property when we extend it to the complex plane [66]. Looking at the complex conjugated versions of our equation set, we see that we have

$$B_m = S_{mm'}(n,k)A_{m'}$$
$$A_m^* = S_{mm'}(n^*,k^*)B_{m'}^*$$

we can obtain the relation

$$\mathbf{S}^{-1}(n^*,k^*) = \mathbf{S}^\dagger(n,k) \tag{2.30}$$

which reduces to the unitarity condition when n and k are real.

Following [46], we set up the following scattering "experiment":

$$H_m^{(-)}(z)e^{im\theta} \to \sum_{m'} S_{m'm}(n,k)H_{m'}^{(+)}(z)e^{im'\theta} \qquad \text{(initial reaction)}$$
$$\sum_m S_{m'm}^*(n^*,k^*)H_m^{(-)}(z)e^{im\theta} \to H_{m'}^{(+)}(z)e^{im'\theta} \qquad \text{(relation (2.30))}$$
$$\sum_m S_{m'm}(n^*,k^*)\overline{H_m^{(-)}(z)}e^{-im\theta} \leftarrow \overline{H_{m'}^{(+)}(z)}e^{-im'\theta}. \qquad \text{(complex conjugate (time reversal))}$$

Use of (A.8c) leads to the relation, valid only when $k \in \mathbb{R}$

$$S_{m'm}(n,k) = (-1)^{m'}S_{-m-m'}(n^*,k)(-1)^m. \tag{2.31}$$

We can also write this in matrix form

$$\mathbf{S}(n,k) = \mathbf{P}\mathbf{S}(n^*,k)^T\mathbf{P} \tag{2.32}$$

where $[\mathbf{P}]_{mm'} = (-1)^m \delta_{-mm'}$. This relationship will be incredibly useful in the numerical implementation.

The **Q**-matrix also has some interesting properties. For real potentials, it is Hermitian. This is a direct consequence of the unitarity of the **S**-matrix as

$$\frac{d\mathbf{S}^\dagger \mathbf{S}}{dk} = \frac{d\mathbf{S}^\dagger}{dk}\mathbf{S} + \mathbf{S}^\dagger \frac{d\mathbf{S}}{dk} = 0 \tag{2.33}$$

and

$$\mathbf{Q}^\dagger = i\frac{d\mathbf{S}^\dagger}{dk}\mathbf{S} = -i\mathbf{S}^\dagger \frac{d\mathbf{S}}{dk} = \mathbf{Q} \tag{2.34}$$

The delays associated with the potential are thus always real and the delay eigenstates form a complete basis. Perhaps the most interesting, and important, result concerning the **Q**-matrix is its connection with the complex poles of the scattering matrix. It can be shown (see [46, 67, 68]) that we can seperate the scattering matrix in *resonance channels* $\{|p_j\rangle\}$ and arrive at Simonius' form [69]

$$\mathbf{S}(k) = \prod_{j=1}^{\infty} \mathbf{S}_j(k) \tag{2.35}$$

where

$$\mathbf{S}_j(k)\left|p_j\right\rangle = \frac{k-k_j^*}{k-k_j}\left|p_j\right\rangle. \tag{2.36}$$

Notice that this unitary expansion on the basis of the resonance channels contains the mirror-symmetry of the poles and zeros of the scattering matrix. Fig. 2.4 shows this symmetry in the case of the scattering matrix of the circular disk.

Using Simonius' expansion and the definition of the **Q**-matrix, we can obtain that the eigendelays q_p of each resonance channel have the form

$$q_p \propto \sum_j \frac{\Gamma_j}{\left(k - \mathrm{Re}\left\{k_j\right\}\right)^2 - \Gamma_j^2/4}. \tag{2.37}$$

When the potential is real, it can be shown that

$$\mathbf{Q}\boldsymbol{A}^p = \tau_p \boldsymbol{A}^p \qquad\qquad \mathbf{Q}\left(\mathbf{S}^\dagger \mathbf{P}\boldsymbol{A}^{p*}\right) = \tau_p \left(\mathbf{S}^\dagger \mathbf{P}\boldsymbol{A}^{p*}\right) \tag{2.38}$$

share the same spectrum. Moreover, since **S** is unitary, we have $\left\|\mathbf{S}^\dagger \mathbf{P}\right\| = 1$ such that normalization is conserved. We can conclude that both sets of eigenvectors are related through a simple phase factor such that

$$\left[\psi_{\mathrm{in}}^p\right]^* = e^{-i\theta_p}\psi_{\mathrm{out}}^p. \tag{2.39}$$

In general, interaction with a potential changes the combination of angular momenta of the incoming field (essentially the coefficients of the Fourier-Bessel expansion, in our case) to a different one, forming a distinct outgoing field. The eigenvectors of the **Q**-matrix form *self-replicating modes*, as the interaction with the cavity leave the angular momentum distribution unchanged

(up to a phase shift). In turn, the energy derivative of this phase shift gives information about the time-delay introduced by the interaction in the form of (2.37).

In the complex case, things become more complicated. Simonius' expansion is no more valid, as the poles and zeros are not longer symmetric along the real axis. The symmetry line is shifted upward in the complex plane [70, 71]. Evaluating the **Q**-matrix along this line yields a spectrum of real eigenvalues, referred to as the proper delay times. However, when the absorption is dispersive, the amount by which the symmetry line depends on $\mathrm{Re}\{k\}$. We must thus evaluate the **Q**-matrix along a curve in the complex k-plane. This shift depends non-trivially on the absorption. It thus becomes rather hard to extract any meaningful information for the **Q**-matrix for a general, complex, potential.

The **S**-matrix also suffers some dramatic changes in its pole structure [72–74], but the fact remains that the poles can still be interpreted as the resonances of the cavity, and that the complex positions yield information about the lifetimes of those resonances. Taking everything into consideration, it seems that, for complex potentials, it is easier to work directly with the scattering matrix than to deal with the **Q**-matrix.

In short, we have used a scattering formalism to solve the differential equations governing the behaviour of bidimensional dielectric cavities. It was shown that the poles of the scattering matrix, which lie in the complex k-plane for real potentials, correspond to the resonances of the structures. Finding the resonances is of vital importance, as they form the backbone of the impulse response of the cavities. Instead of directly computing these poles, we use the time-delay matrix to find the signatures of the poles onto the real k-line. The spectrum of this matrix is composed of a superposition of Lorentzian curves and the maxima of these curves, of which there is a countably finite number, correspond to the poles of the scattering matrix. The eigenvectors of the time-delay matrix define the modes of the cavity as a set of *self-replicating modes*. The use of this matrix in the general case (when the potential is complex) is complicated by a number of factors, most notably the sudden and major change to the pole structure of the scattering matrix. We thus conclude that, in this case, it is best to directly compute the poles of the scattering matrix.

2.3 Numerical Method I: SQA

The numerical computation of the scattering matrix depends on two constructs: a polar discretization scheme colloquially denoted the onion discretization, and interior scattering matrices. We choose, for the former, a rather standard radial discretization (see Fig. 2.5). For easier reference, we dub the method the **S**- and **Q**-matrix algorithm (SQA).

The latter relate the solutions inside each radial shell to its neighboring shell. The final interior scattering matrix relates the solution in the last shell to the exterior solution, which is analytically known and is related to the **S**-matrix of the cavity.

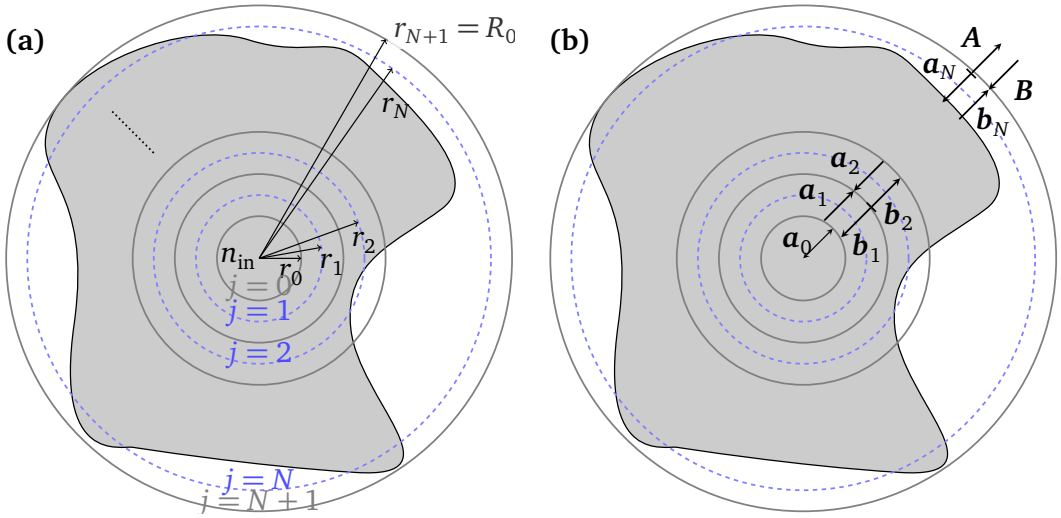

Figure 2.5 – Radial discretization of the cavity for use in SQA. The inner circle is assumed to have a constant refractive index denoted n_{in}. The full grey lines represent the physical boundaries of each shell while the dotted blue lines represent their center. **(a)** The central radius r_j is the radial position at which the refractive index is sampled. The boundary conditions are enforced at $r = r_j \pm \epsilon$. **(b)** Note the alternating propagation directions of the solutions inside each shell. This reflects the local definition of "incoming" vs "outgoing waves" for each r_j.

Our method is based on an algorithm originally developed by Rahachou and Zozoulenko [75] and extended by [46]. We generalize the method to accept complex refractive index profiles n.

2.3.1 *Divide et impera*

We wish to solve the Hellholtz equation[3]

$$\left[\nabla^2 + k^2 n^2\right]\psi = 0 \tag{2.40}$$

inside the cavity. For $r > R_0$, the radius of the smallest circle that encloses the whole dielectric, the solution is (2.17). We apply the discretization of Fig. 2.5. We define a set of radii $\{r_j\}_{j=0}^{N+1}$ that denote the positions of the center of the different shells. As such, $r_j - r_{j-1} = 2\epsilon$ for the inner shells. The cases $j = 0$ and $j = N+1$ are different in that r_0 and r_{N+1} denote the outer and inner limits of the domains, respectively. Moreover, $r_{N+1} - r_N = r_1 - r_0 = \epsilon \neq 2\epsilon$. As our first approximation, we suppose that the refractive index inside the inner circle is constant and call it n_{in}. The Helmholtz equation then merely becomes the Bessel equation (A.1). Enforcing finiteness of the field at $r = 0$, we have the solution[4]

$$|\psi(r)\rangle = \sum_{m=-\infty}^{\infty} 2a_m^0 J_m(n_{\text{in}} kr)\left|\Phi_m^0\right\rangle \qquad (r < r_0) \tag{2.41}$$

[3] The main text focuses on the TM polarization; TE is treated in Appendix B.1.

[4] Even though all summations are formally infinite, we will truncate them to a maximum momentum M in the numerical implementation. The summations will thus contain $2M+1$ terms and will run from $m = -M$ to $m = M$.

where we have introduced bra-ket notation for the angular part of the solution. In that case,

$$\left\langle \theta \middle| \Phi_m^0 \right\rangle = e^{im\theta}. \tag{2.42}$$

In the shells $j > 0$, the differential equation to solve is rather

$$\left[\frac{d^2}{dr^2} + \frac{1}{r}\frac{d}{dr} + \frac{1}{r^2}\frac{d^2}{d\theta^2} + k^2 n^2(r,\theta)\right]\psi = 0. \tag{2.43}$$

Inside each shell, we suppose that the potential strength depends only on the angular variable, i.e. $k^2 r^2 n^2(r,\theta) \mapsto k^2 r_j^2 n^2(r_j,\theta)$ such that the angular sampling of the refractive index is done at $r = r_j$ for each shell. (2.43) is then amenable to a separation of variables

$$\left[\rho_j^2 \frac{d^2}{d\rho_j^2} + \rho_j \frac{d}{d\rho_j} - \xi^j\right]\mathscr{R}^j = 0 \tag{2.44a}$$

$$\left[\frac{d}{d\theta^2} + \left(k^2 n^2(r_j,\theta) r_j^2 + \xi^j\right)\right]\Phi^j = 0 \tag{2.44b}$$

where $\rho_j = r/r_j$ is the scaled radial variable of the shell. These equations can readily be solved by noticing that $\Phi^j(\theta + 2\pi) = \Phi^j(\theta)$. We expand the solution in a Fourier series

$$\left\langle \theta \middle| \Phi_\mu^j \right\rangle = \frac{1}{\sqrt{2\pi}} \sum_{m=-\infty}^{\infty} c_{\mu m}^j e^{im\theta} \tag{2.45}$$

Projecting onto $\left|\Phi_m'^0\right\rangle$ yields

$$\sum_{m=-\infty}^{\infty} \left[-m^2 \left\langle \Phi_{m'}^0 \middle| \Phi_m^j \right\rangle + \xi^j \left\langle \Phi_{m'}^0 \middle| \Phi_m^j \right\rangle + k^2 r_j^2 \left\langle \Phi_{m'}^0 \middle| n^2(r_j,\theta) \middle| \Phi_m^j \right\rangle\right] = 0 \tag{2.46}$$

Noticing that

$$\left\langle \Phi_{m'}^0 \middle| \Phi_m^j \right\rangle = \sum_{m=-\infty}^{\infty} c_{\mu m}^j \delta_{mm'} \tag{2.47}$$

we can write

$$\sum_m \left[-m^2 \delta_{mm'} + \xi^j \delta_{mm'} + \frac{k^2 r_j^2}{2\pi} \int_0^{2\pi} n^2(r,\theta) e^{i(m-m')\theta} d\theta\right] c_{\mu m}^j = 0. \tag{2.48}$$

Using this last equation, we can set up an eigenvalue problem for the separation constant and the Fourier coefficients

$$\mathbf{L}^j \boldsymbol{c}_\mu^j = \xi_\mu^j \boldsymbol{c}_\mu^j \tag{2.49}$$

with

$$L_{mm'}^j = m^2 \delta_{mm'} - \frac{k^2 r_j^2}{2\pi} \int_0^{2\pi} n^2(r_j,\theta) e^{i(m-m')\theta} d\theta. \tag{2.50}$$

The particular form and additional properties of this matrix are discussed in Appendix B.1.

Now that we know the set of eigenvalues $\{\xi_\mu^j\}$, we can solve the radial equation (2.44a). It is instantly recognized as a Cauchy-Euler equation. Given its coefficients, one can write the solution as [76, p. 118-119]

$$\mathscr{R}_\mu^j(r) = a_\mu^j \rho_j^{+\sqrt{\xi_\mu^j}} + b_\mu^j \rho_j^{-\sqrt{\xi_\mu^j}}. \tag{2.51}$$

Solving the N eigenvalue problems (2.49) gives the solution in all space. We can now apply the boundary conditions (2.12) at the interface of each shell $j \to j+1$. The process generates two sets of equations

$$\sum_\mu \left[a_\mu^j \rho_j^{+\sqrt{\xi_\mu^j}} + b_\mu^j \rho_j^{-\sqrt{\xi_\mu^j}} \right] \left| \Phi_\mu^j \right\rangle = \sum_\mu \left[b_\mu^{j+1} \rho_{j+1}^{+\sqrt{\xi_\mu^{j+1}}} + a_\mu^{j+1} \rho_{j+1}^{-\sqrt{\xi_\mu^{j+1}}} \right] \left| \Phi_\mu^{j+1} \right\rangle \tag{2.52a}$$

$$\frac{d}{dr} \sum_\mu \left[a_\mu^j \rho_j^{+\sqrt{\xi_\mu^j}} + b_\mu^j \rho_j^{-\sqrt{\xi_\mu^j}} \right] \left| \Phi_\mu^j \right\rangle = \frac{d}{dr} \sum_\mu \left[b_\mu^{j+1} \rho_{j+1}^{+\sqrt{\xi_\mu^{j+1}}} + b_\mu^{j+1} \rho_{j+1}^{-\sqrt{\xi_\mu^{j+1}}} \right] \left| \Phi_\mu^{j+1} \right\rangle \tag{2.52b}$$

The interior scattering matrices are constructed via pre-multiplying by the left eigenvectors $\left\langle \tilde{\Phi}_\mu^j \right|$ on each side. Combining both resulting equations leads to the linear system

$$\begin{pmatrix} \mathbf{A} & \mathbf{B} \\ \mathbf{C} & \mathbf{D} \end{pmatrix} \begin{pmatrix} \boldsymbol{a}^j \\ \boldsymbol{a}^{j+1} \end{pmatrix} = \begin{pmatrix} \mathbf{E} & \mathbf{F} \\ \mathbf{G} & \mathbf{H} \end{pmatrix} \begin{pmatrix} \boldsymbol{b}^j \\ \boldsymbol{b}^{j+1} \end{pmatrix} \tag{2.53}$$

which can be inverted using Schur's complements [77, p. 123] to yield a relationship between the $\boldsymbol{a}$ and $\boldsymbol{b}$ coefficients, i.e.

$$\mathbf{S}_j = \begin{pmatrix} \mathbf{E} & \mathbf{F} \\ \mathbf{G} & \mathbf{H} \end{pmatrix}^{-1} \begin{pmatrix} \mathbf{A} & \mathbf{B} \\ \mathbf{C} & \mathbf{D} \end{pmatrix}. \tag{2.54}$$

Physically, the $\mathbf{S}_j$ matrix relates the locally incoming waves from shell $j+1$ in shell j to the locally outgoing from shell j to shell $j+1$. The last necessary breakthrough is to realize that we can connect the solutions from shell j to those of the shell $j+2$, then $j+3$ and so on. When started from $j=0$, this iterative process yields the relationship

$$\begin{pmatrix} \boldsymbol{a}^0 \\ \boldsymbol{B} \end{pmatrix} = \mathbf{S}^{0,N} \begin{pmatrix} \boldsymbol{a}^0 \\ \boldsymbol{A} \end{pmatrix} \tag{2.55}$$

such that the $\mathbf{S}$-matrix of the system is the block $\mathbf{S}_{22}^{0,N}$. More details can be found in Appendix B.1.

2.3.2 Numerical Analysis and Calibration

While numerical analysis has been heavily formalized in recent years, it is still as much an art as a science. In implementing the algorithm, we thus came across two potential problems: the inversion of the $\mathbf{K}$ matrix (defined below) and the final Hadamard product $\mathscr{H} \circ \mathbf{S}_{22}^{0,N}$. We analyze the two issues and provide solutions to the instabilities they cause. We also calibrate the method with the homogeneous circular cavity and also compare our method to results obtained in the literature.

2.3.2.1 Numerical Back and Forth

For the computation of each $\mathbf{S}_j$, we must invert a matrix of the form

$$\mathbf{K}^{j,j+1} = \left(\frac{r_j - \epsilon}{r_j + \epsilon}\right)^{\Lambda^j} - \tilde{\mathbf{S}}_{11}^{j+1}\left(\frac{r_j + \epsilon}{r_j - \epsilon}\right)^{\Lambda^j}\tilde{\mathbf{S}}_{22}^{0,j} \tag{2.56}$$

where the $\tilde{\mathbf{S}}$ are internal scattering matrices, defined in Appendix B.1. Given that the elements of this matrix highly depend upon the discretization parameter ϵ, the half-width of the shells, we can use the condition number W of this matrix as an indicator of the quality of the discretization. It can be grossly estimated by the ratio of the maximum and minimum elements of the matrix. By assuming that there is no amplification in the system, all interior scattering matrices have $||\mathbf{S}|| \leq 1$ and we can approximate

$$W \sim \left(\frac{r_j + \epsilon}{r_j - \epsilon}\right)^{2\lambda_{\max}} \sim 1 + \frac{4\lambda_{\max}\epsilon}{r_j} \tag{2.57}$$

according to the binomial expansion. To evaluate the $\lambda_{\max}$ parameter, we will have to take a detour and introduce the concept of *Gerschgorin circles* and some obscure properties of Fourier series.

(a) Gerschgorin Circles Gerschgorin circles provide a way to bound the spectrum of square matrices by simply examining its entries.

Theorem 2.1 (Gerschgorin circles [77, p. 498]). *The eigenvalues of a matrix $\mathbf{A} \in \mathbb{C}^{n\times n}$ are contained within the intersection $\mathscr{G}_r \cap \mathscr{G}_c$ of the sets of row and column Gerschgorin circles, defined respectively as*

$$\mathscr{G}_r = \left\{ |z - a_{ii}| \leq \sum_{\substack{j=0 \\ j\neq i}}^{n-1} |a_{ij}|; \quad \forall i \right\} \qquad \mathscr{G}_c = \left\{ |z - a_{jj}| \leq \sum_{\substack{i=0 \\ i\neq j}}^{n-1} |a_{ij}|; \quad \forall j \right\},$$

or, in a slightly more algorithmically-friendly form:

$$\mathscr{G}_r \cap \mathscr{G}_c = \left\{ |z - a_{ii}| \leq \min\left(\sum_{\substack{j=0 \\ j\neq i}}^{n-1} |a_{ij}|, \sum_{\substack{j=0 \\ j\neq i}}^{n-1} |a_{ji}| \right); \quad \forall i \right\}. \tag{2.58}$$

Corrolary 2.2. *Diagonally dominant matrices are non-singular.*

Proof. Diagonally dominant matrices, by definition, have

$$|a_{ii}| > \max\left(\sum_{\substack{j=0 \\ j\neq i}}^{n-1} |a_{ij}|, \sum_{\substack{j=0 \\ j\neq i}}^{n-1} |a_{ji}| \right) \tag{2.59}$$

and, by Gerschgorin's theorem, do not have 0 as an eigenvalue, $0 \notin \sigma(\mathbf{A})$, and therefore are non-singular. □

Example 2.1. Consider the matrix [77, p. 499]

$$\mathbf{A} = \begin{pmatrix} 5 & 1 & 1 \\ 0 & 6 & 1 \\ 1 & 0 & -5 \end{pmatrix}. \tag{2.60}$$

Its associated Gerschgorin circles are shown in Fig. 2.6. We see that the row and column circles give different bounds on the eigenvalues and their intersection yields the best possible approximations for the eigenvalues.

We now apply the Gerschgorin circles to our $\mathbf{L}^j$ matrix. In Appendix B.1, we show that a proper choice for M is $M = 2kR_0\sqrt{\max_{(r,\theta)}(n^2(r,\theta))}$. This criterion ensures that we sample the refractive index above the Nyquist frequency. The largest diagonal element (the farthest Gerschgorin circle) corresponds to the highest angular momentum and has a magnitude of $4k^2R_0^2\max_{(r,\theta)}\left(n^2(r,\theta)\right) - k^2R_0^2n^2(r,\theta) \sim 3k^2R_0^2n^2$. The radius is more complicated to estimate, as it is given by the sum of the norm of the Fourier coefficients of $n^2(r,\theta)$, which we call n_m:

$$r = \sum_{m=1}^{M} |n_m|. \tag{2.61}$$

It can be shown that there exists an upper bound for the value of the Fourier coefficients [78]

$$|n_m| \leq \frac{V}{2m\pi} \tag{2.62}$$

where V is the variation of the refractive index and is defined as

$$V(r) = \int_0^{2\pi} \left|\partial_\theta n^2(r,\theta)\right| d\theta. \tag{2.63}$$

To go further, we must realize the mixed blessing of the logarithmic divergence of the harmonic series[5]. We estimate the radius of the Gerschgorin circle by taking $M = 500$, an arbitrary bound that is unattainable by our algorithm[6] such that the upper bound for the radius becomes $r \leq 3V/\pi$. Taking the annular cavity, a circular cavity of constant refractive index of which a circular hole as been cut [79], as an example, the variation is approximately given by $2n^2$. Pulling everything together, this yields an approximate upper bound for the largest eigenvalue as

$$|\lambda_{\max}| < 3nkR_0 \tag{2.64}$$

A good choice of ϵ is thus

$$\epsilon \ll \frac{1}{12nk} \ll \frac{\lambda}{2n} \tag{2.65}$$

which mirrors the conventional wisdom. This empirical rule is applied in every computation in this essay.

[5] A better bound could be obtained, but requires more stringent conditions on the behaviour of $n^2(r,\theta)$ that the author is not comfortable assuming, given typical experimental conditions.

[6] The Bessel functions overflow the `double` floating-point representation at approximately $M \sim 250$, rendering the algorithm useless.

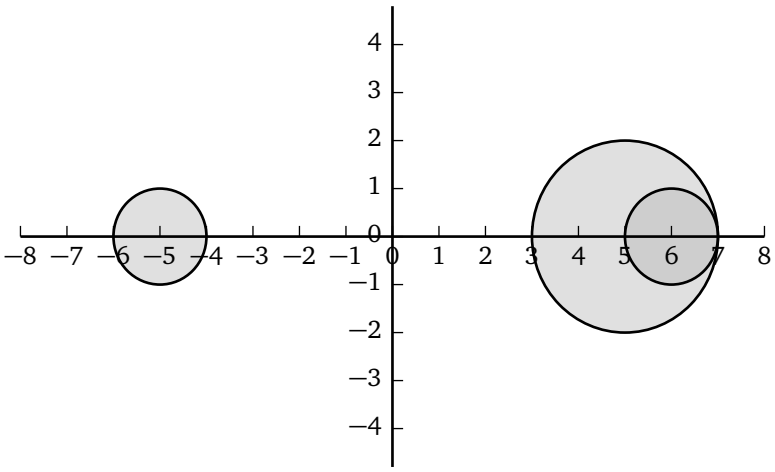

(a) Row Gerschgorin circles

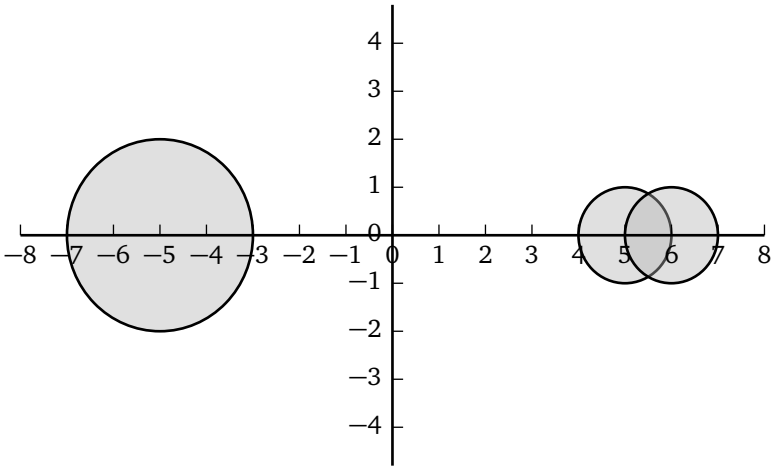

(b) Column Gerschgorin circles

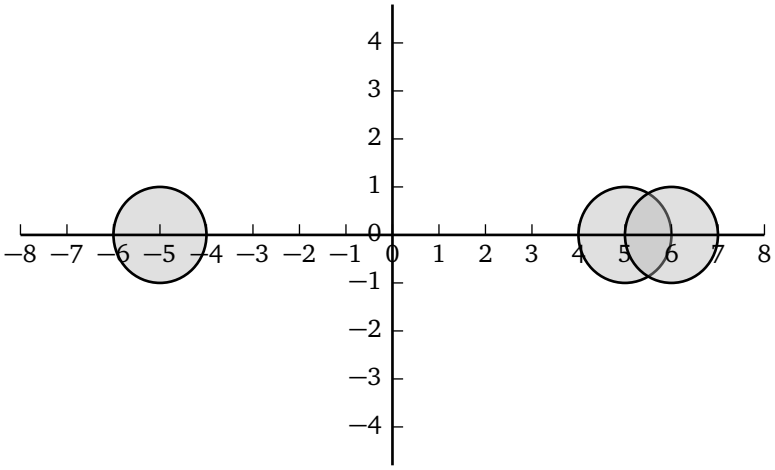

(c) Intersection of both previous sets

Figure 2.6 – Gerschgorin circles of the matrix defined in (2.60). Notice that the matrix is non-singular by Corrolary 2.2.

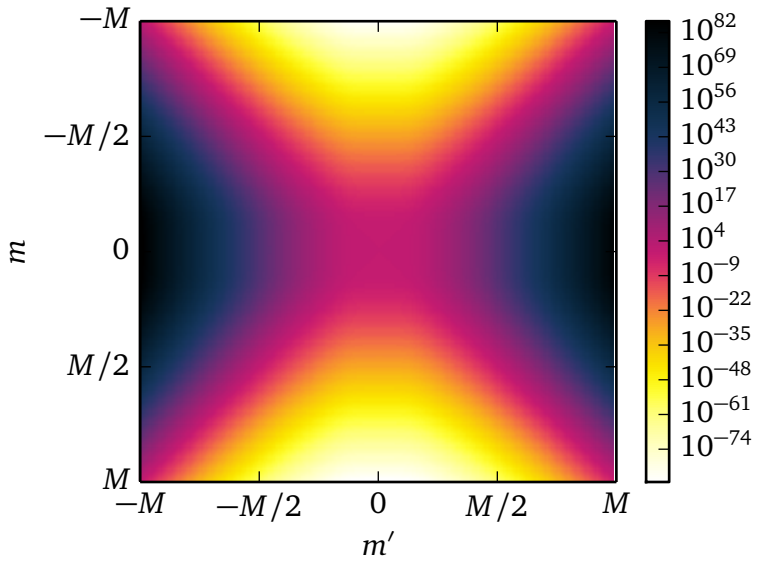

Figure 2.7 – General form of absolute value of the Hankel matrix $\mathscr{H}$. We have used the parameters $z = 10$ and $M = 100$, but the pattern scales with M and z.

2.3.2.2 Hadamard Product

Like Frodo before Mount Doom, we must face a final challenge before conquering upon all evil, or, in our case, computing the scattering matrix. Our final demon takes the form of the product

$$\mathbf{S} = \left[\mathbf{H}^{(+)}\right]^{-1} \mathbf{S}_{22}^{0,N} \mathbf{H}^{(-)} \tag{2.66}$$

where the $\mathbf{H}$ are diagonal matrices with entries $H_m^{(\pm)}(n_o k R_0)$. We recast the matrix product as a Hadamard (element-wise) product

$$\mathbf{S} = \mathscr{H} \circ \mathbf{S}_{22}^{0,N} \tag{2.67}$$

with $\mathscr{H}_{mm'} = H_m^{(-)}(n_o k R_0)/H_{m'}^{(+)}(n_o k R_0)$. A quick peek at Fig. 2.7 announces the disaster. The region $|m'| > |m|$ increases exponentially with $|m'| - |m|$. This wouldn't be an issue if the corresponding elements of the block scattering matrix $\mathbf{S}_{22}^{0,N}$ were exponentially decreasing (as we physically expect them to); however, the numerical construction of this matrix implies the addition and subtraction of $\mathscr{O}(1)$ floating-point numbers, limiting their range to about 10^{-15}, the decimal accuracy associated with `double` precision arithmetic. Consequently, the final Hadamard product yields scattering matrices with unphysically large off-diagonal elements.

Several solutions to this numerical artefact have been considered, e.g. the use of matrix masks and of higher precision arithmetic. The latter was swiftly abandoned due to the difficulty of the implementation[7], even though it could help stabilize the numerical algorithm [80, §5.8.4]. The

[7] Even if we disregard the fact that no C++ compiler support the IEEE 754 `binary128` quadruple precision floating-point representation, we would still need to find numerical libraries that extend the BLAS and LAPACK libraries to work at higher precision.

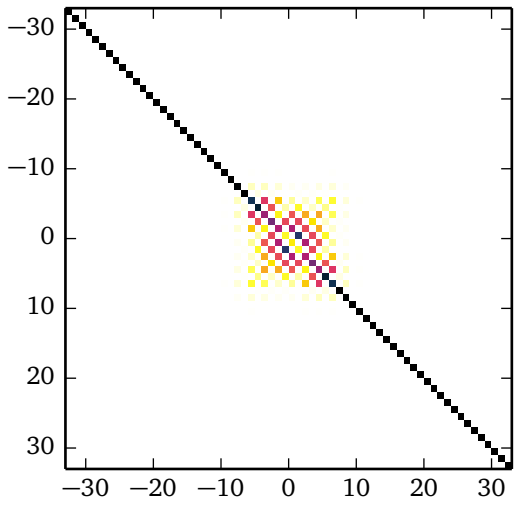

Figure 2.8 – Scattering matrix of the elliptical cavity with $n_c = 3.3$, $a = 1$ and $b = 0.53477$, giving $e = 0.845$. Recall that $r(\theta) = ab/\sqrt{(b\cos\theta)^2 + (a\sin\theta)^2}$. Notice that the non-vanishing elements have a banded form: they decrease with the distance from the diagonal and eventually go to zero. Beyond a particular value of the angular momentum ($M_{\text{max}} = 6$, in this case), the scattering matrix is diagonal: there is no mixing of angular momenta. The value of M_{max} depends on the inhomogeneity of both the boundary of the cavity and that of its refractive index. It could be inferred from the Fourier transform of the refractive index.

use of matrix masks is made possible by noting that the cavity cannot convert arbitrarily high angular momenta. The maximum angular momentum it can affect, M_{max} is a function of its "degree of inhomogeneity", characterized by the absolute size of the Fourier components of the refractive index (which also depends on the geometry of the cavity). This gives the **S**-matrix a banded form (see Fig. 2.8 for an example using the elliptical cavity). The width of this band could be detected in $\mathbf{S}_{22}^{0,N}$ before taking the Hadamard product, or inferred from the coefficients of the Fourier transform of $n^2(r,\theta)$. After the product, all elements outside this band could be set to zero. The interested reader might want to go through Türeci's discussion of the banded form and the numerical problems associated with the Hankel matrices [81, §3.4].

We have, however, chosen a different path. It turns out that relation (2.31) precisely relates the diverging parts of the Hankel matrix to its vanishing one. Imposing this symmetry on the numerical scattering matrix allows the algorithm to return physical scattering matrices. This limits the scope of our method to real energies (k) and has a high computational cost for complex refractive indices. This limitation, coupled to the fragility of the generalization to $n \in \mathbb{C}$[8] suggests the use of other methods for complex energies and potentials.

[8] We discuss this fragility in more detail in Appendix B.1.

2.3.2.3 Calibration

One of the most important step in algorithmic creation is the *calibration phase*. We calibrate the method using the analytical form of the **S**-matrix for the homogeneous, circular cavity and compare the results from the literature.

(a) Homogeneous, Circular Cavity The scattering matrix of the homogeneous circular cavity is trivially obtained. Assuming that the refractive index inside the cavity is n_c and n_o outside, the solution inside the cavity is given by

$$\psi^c = \sum_m a_m^c J_m(n_o k r) e^{im\theta} \tag{2.68}$$

while the solution outside the cavity is given by (2.17). Imposing the electromagnetic boundary conditions yields two infinite sets of equations for three sets of coefficients. Solving yields a linear relationship between the A_m and B_m sets, *viz.* the scattering matrix

$$S_{mm'}^{\mathrm{HD}} = -\frac{\eta_{co} J_m'(Z_c) H_m^{(-)}(Z_o) - J_m(Z_c) H_m^{(-)'}(Z_o)}{\eta_{co} J_m'(Z_c) H_m^{(+)}(Z_o) - J_m(Z_c) H_m^{(+)'}(Z_o)} \delta_{mm'}. \tag{2.69}$$

where $Z_c = n_c k R_0$, $Z_o = n_o k R_0$ and $\eta_{co} = n_c/n_o$ (n_o/n_c) in TM (or TE) polarization.

Before, we showed the correspondence between the poles of the scattering matrix and its associated time delay spectrum analytically (see p. 19). In Fig. 2.9, we show the time delay spectrum of the homogeneous disk. The corresponding poles of the **S**-matrix are denoted by squares[9]. There seems to be a problem with the very high-Q ones, but this is only due to the fact that we have not used a sufficiently small discretization Δk. The other ones line up perfectly with the peaks of the time delay.

In Fig. 2.10, we compare the analytical scattering matrix to the one computed via SQA. We use

$$E = \max\left[\mathbf{S}_{\mathrm{ana}} - \mathbf{S}_{\mathrm{SQA}}\right] \tag{2.70}$$

as a function of the discretization size $kR_0 2\epsilon$ to measure the error. Notice that the convergence speed is the same for all curves, regardless of the value of kR_0. Convergence does not depend on the value of M as the homogeneous, circular cavity has a diagonal scattering matrix.

(b) Comparison to other methods To make sure we can blindly accept the results of our numerical technique, we apply it to non-integrable geometries that have been studied by other means in the literature. Table 2.1 shows a comparison of the positions of the certain resonances for a set of selected geometries. Fig. 2.11 shows the time delay spectrum of the square cavity. The higher-delay mode, highlighted in the figure, has a field profile (inset) that resembles a WGM. The

[9] The poles are computed via the zeros of the denominator of (2.69) using a Newton-Raphson algorithm. The initial guesses are provided by the asymptotic ($kR_0 \gg m$) zeros of the denominator. See [82, Annexe A.2.4] for a derivation.

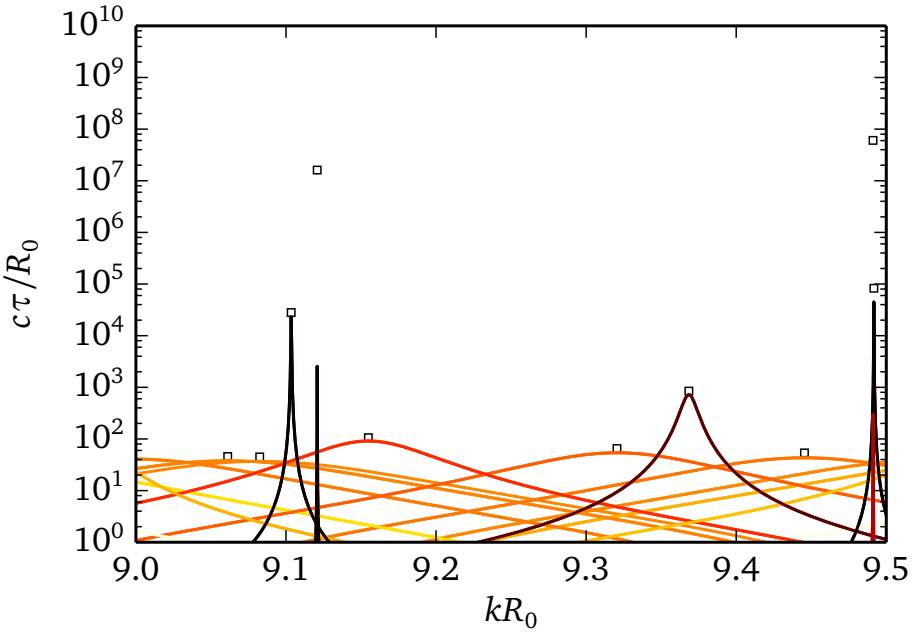

Figure 2.9 – Time delay spectrum of a circular cavity with $n_c = 3.2$ and $n_o = 1$ in TM polarization. The squares represent the complex position of the poles of the scattering matrix. The equivalent time delay is computed using $c\tau/R_0 = -\mathrm{Re}\{kR_0\}/2\mathrm{Im}\{kR_0\}$.

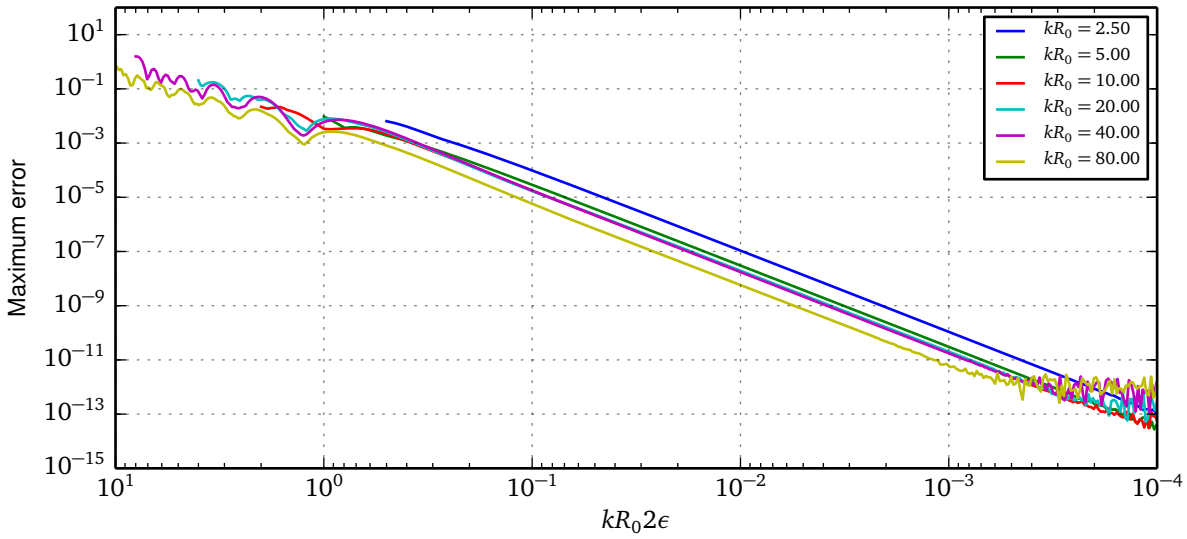

Figure 2.10 – Calibration of SQA against the homogeneous disk. The cavity has refractive index $n_c = 1.5$ and is embedded in air $n_o = 1$. The exterior radius is set to $R_0 = 1$ and we take the number of shells to be $N = 2$. The error approximately follows a cubic power-law behaviour in the discretization size.

Cavity	SQA		Emission Viewpoint		Source
	kR_0	$2R_0/c\tau$	$\mathrm{Re}\{kR_0\}$	$\lvert\mathrm{Im}\{kR_0\}\rvert$	
Square	4.53	1.06×10^{-4}	4.54	1.05×10^{-4}	[84]
Stadium	4.89	0.052	4.89	0.055	[85]
Ellipse	6.499	0.029	6.50	0.032	[43]
Annular	10.266	0.083	10.268	0.081	[46]

Table 2.1 – Real and imaginary parts of the resonant frequencies computed with SQA compared with results from the literature.

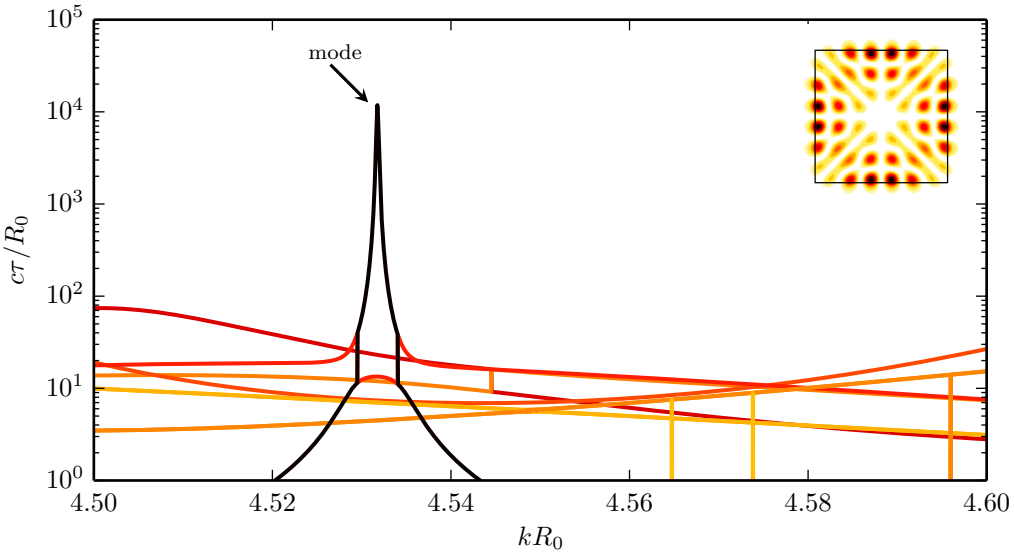

Figure 2.11 – Delay spectrum of the square cavity. The highlighted mode has a high Q-factor, which can be explained by its WGM-like field recirculation. The inset of the figure shows the actual field profile of the mode. It was computed using COMSOL by G.P.-A. [46].

localization of light in square cavities has since been confirmed experimentally [83] and observed in other geometries [42].

We also notice that the resonance at $k = 4.53$ is degenerate. The highlighted mode has a high delay, but it coexists with a low delay mode. In practice, when there are imperfections, this might become a problem, as the high-Q modes are highly sensitive to perturbations [75]. Another interesting feature can be seen at $k \sim 4.545$, where two modes show an avoided crossing. The vertical line the spectrum corresponds to where the modes "switch".

2.4 Case Study: Gaussian Deformation of the Refractive Index

As an academic demonstration of the power of the method, we present a study of a circular cavity whose refractive index has a Gaussian shape

$$n(r,\theta) = n_0 + \delta n \exp\left[-\frac{r^2 + 2dr\cos(\Theta-\theta) + d^2}{2w^2}\right], \tag{2.71}$$

where n_0 is the background refractive index, δ_n the deformation amplitude, w its half-width and (d,Θ) its position relative to the center of the cavity.

As previously noted by G. P-A. [46], a peculiar duality exists between high-Q resonances and directional emission. Working with a cavity similar to the annular one, it stands to reason that we will recover the same pattern. This study will be used as a stepping stone for our inquiries in the realm of non-uniformly pumped active microcavities.

2.4.1 Loss of Integrability and the KAM Scenario

When $d = 0$, the potential is central and angular momentum is conserved. If the system is also unitary (no absorption nor gain), it can be shown that the system is integrable[10]. This conservation of angular momentum in turn implies circular symmetry of the fields and hence of the far-field radiation pattern. Since most applications (particularly lasers) require a certain directionality in the emission, our goal is to break the circular symmetry in such a way as to minimize the degradation of the Q-factor and maximizing the output directionality. Historically, this goal has spawned the research field of ARCs [23, 79, 86–89] wherein the boundary of the circular cavity is parametrically deformed to yield limaçon, stadium, elliptical, quadrupolar, and other shapes.

The underlying classical mechanics of ARCs follow the KAM scenario as the geometry is perturbed away from a perfect circle. In phase space, regularity yields to the chaotic sea, dividing it into regions of regular motion and regions of ergodic motion. The Hamiltonian nature of the dynamics has been thoroughly studied and has been used to tame the animosity of directionality and high-Q emission [24, 90]

In our case, we do not deform the boundary, leaving it a perfect circle, but use a deformation of the refractive index. This particular deformation – the Gaussian one – is of theoretical and practical interest, as it can easily be induced by shining light on the dielectric from above. This refractive index profile is also obtained when pumping a microcavity laser with another laser.

[10] The covariant form of Maxwell's equation and their associated Euler-Lagrange equation make this conservation perfectly clear.

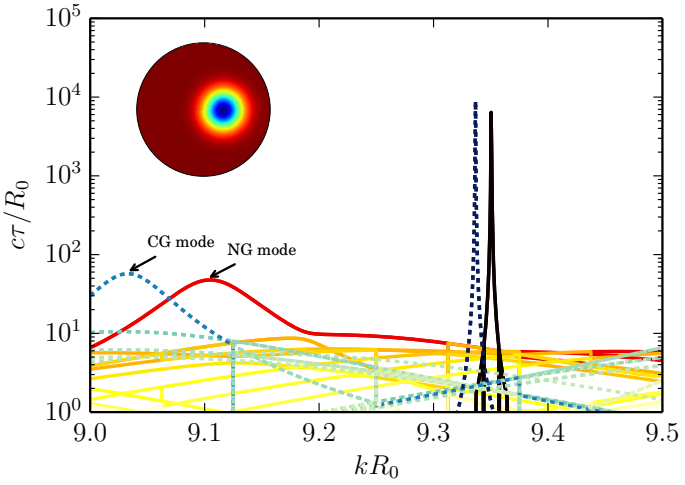

(a) Delay spectrum of the gaussian microcavity. The dotted blue lines show the spectrum for the integrable case of the deformation, i.e. $d = \Theta = 0$ (CG mode). The full red lines show the spectrum for the deformation centered at $d = 0.3R_0$ and $\Theta = 0$ (NG mode).

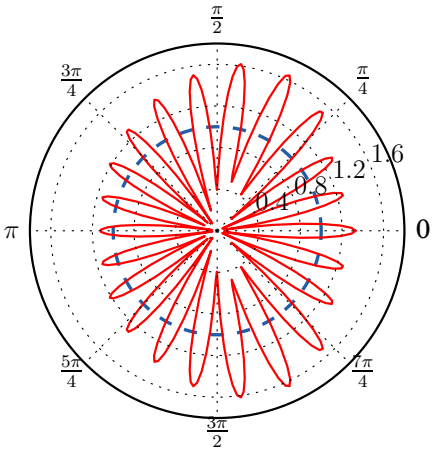

(b) Far-fields of both CG (dotted blue) and NG (full red) modes. The isotropy is broken when the potential loses its circular symmetry. The NG mode has mild directionality in the directions $\theta = \pm 65°$, owing to the diverging lens effect of the deformation.

Figure 2.12 – Delay spectrum and far-field. **(a)** Delay spectrum of cavity with the Gaussian deformation with parameters $n_0 = 2$, $\delta n = -1$ and $w = 0.2R_0$. **(b)** shows the far-field of the both the CG and NG modes. Notice the mild directionality of the NG mode.

2.4.2 Numerical Results

Fig. 2.12(b) shows our primary result, i.e. that loss of symmetry may introduce directionality in the far-field. The directionality is mild in our example, but the cavity serves as a proof-of-concept. In Fig. 2.12(a), the dotted blue lines show the delay spectrum of the centered Gaussian (CG) deformation, an integrable cavity, and the full red lines the spectrum of the non-centered Gaussian (NG) deformation. Notice that the higher-delay modes are barely affected by the inhomogeneity. While we do not know the field profile, it is safe to assume the two high-delay modes behave like WGMs. Although it is not shown, both modes have isotropic far-fields. The rather small shift in wavenumber can be understood by the slight rarefaction of the medium near the deformation. The field must "evade" being caught by the deformation to retain its WGM properties, which results in slight positive increase in k (smaller wavelength).

The lower delay modes, the highlighted ones in 2.12(a) are more affected by the inhomogeneity, as their field must be more extended in the dielectric. The field thus "feels" a greater rarefaction of the medium and the mode suffers both a greater Δk and a pronounced change in its emission properties. The angular momentum mixing is such that that the "backscattering" $|\psi_{\mathrm{FF}}(\theta = \pi)|$ is minimized and that the scattering in directions $\theta \sim \pm 3\pi/8$ is favoured. This directionality may somewhat be explained by a ray analysis of the system, as the deformation acts as a diverging

lens. The next section will explain this in more detail.

2.4.3 Geodesics and Ray Analysis[11]

While our numerical method allows us tu perform full-wave simulations of cavities, it is often useful to consider the associated billiard system, which is the small wavelength approximation of Helmholtz's equation. In homogeneous ARCs, photons follow straight path trajectories and are specularly reflected at the interfaces. In inhomogeneous ARCs, photons follow curved trajectories that obey Fermat's principle. The general equations defining those *geodesic* paths can be found by using the metric

$$(dt)^2 = g_{\mu\nu} dx^\mu dx^\nu. \tag{2.72}$$

For photons, the metric is simply given by the optical length of the medium, $g_{\mu\nu} = n^2(\boldsymbol{r})\delta_{\mu\nu}$. The time it takes to travel a particular trajectory is given by

$$t = \int_{\lambda_0}^{\lambda_1} \sqrt{g_{\mu\nu}\dot{x}^\mu \dot{x}^\nu}\, d\lambda \tag{2.73}$$

where λ is a parameter of the curve. By Fermat's principle, photon trajectories minimize the time of flight. We thus apply the Euler-Lagrange equation

$$\frac{\partial L}{\partial x^\alpha} - \frac{d}{d\lambda}\frac{\partial L}{\partial \dot{x}^\alpha} = 0 \tag{2.74}$$

on the functional $L = \sqrt{w} = \sqrt{g_{\mu\nu}\dot{x}^\mu \dot{x}^\nu}\, d\lambda$ Evaluating the derivatives

$$\begin{aligned} 0 &= \frac{\partial\left(\sqrt{w}\right)}{\partial x^\alpha} - \frac{d}{d\lambda}\frac{\partial\left(\sqrt{w}\right)}{\partial \dot{x}^\alpha} \\ &= \frac{\partial w}{\partial x^\alpha} + \frac{1}{2\sqrt{w}}\frac{dw}{d\lambda}\frac{\partial w}{\partial \dot{x}^\alpha} - \frac{d}{d\lambda}\frac{\partial w}{\partial \dot{x}^\alpha} \end{aligned}$$

When λ is an affine parameter, the derivative $dw/d\lambda$ vanishes [91, 92] and the Euler-Lagrange equation becomes

$$\begin{aligned} \frac{\partial w}{\partial x^\alpha} &= \frac{d}{d\lambda}\frac{\partial w}{\partial \dot{x}^\alpha} \\ g_{\mu\nu,\alpha}\dot{x}^\mu \dot{x}^\nu &= \frac{d}{d\lambda}\left[g_{\mu\nu}\delta_\alpha{}^\mu \dot{x}^\nu + g_{\mu\nu}\delta_\alpha{}^\nu \dot{x}^\mu\right] \\ &= \frac{d}{d\lambda}\left[g_{\alpha\nu}\dot{x}^\nu + g_{\mu\alpha}\dot{x}^\mu\right] \\ &= g_{\alpha\nu,\lambda}\dot{x}^\lambda \dot{x}^\nu + g_{\alpha\nu}\ddot{x}^\nu + g_{\mu\alpha,\lambda}\dot{x}^\lambda \dot{x}^\mu + g_{\mu\alpha}\ddot{x}^\mu \qquad \text{(chain rule: } \tfrac{dg_{\mu\nu}}{d\lambda} = \tfrac{\partial g_{\mu\nu}}{\partial x^\lambda}\tfrac{dx^\lambda}{d\lambda}\text{)} \\ g_{\alpha\nu}\ddot{x}^\nu + g_{\mu\alpha}\ddot{x}^\mu &= \dot{x}^\mu \dot{x}^\nu\left[g_{\mu\nu,\alpha} - g_{\alpha\nu,\mu} - g_{\mu\alpha,\nu}\right] \qquad \text{(collecting differentiation orders)} \\ \delta^\sigma{}_\mu \ddot{x}^\mu &= \frac{1}{2}g^{\sigma\alpha}\left[g_{\mu\nu,\alpha} - g_{\alpha\nu,\mu} - g_{\alpha\mu,\nu}\right]\dot{x}^\mu \dot{x}^\nu \qquad \text{(symmetry of } g_{\mu\nu} \text{ and } \times g^{\sigma\alpha}\text{)} \end{aligned}$$

[11] We use Schutz's [91] notation in this section. Repeated indices are summed over; $g_{\alpha\beta}$ is the metric tensor; the notation $M_{\alpha\beta,\gamma}$ indicates differentiation with respect to γ. The contravariant tensor $g^{\alpha\beta}$ is the inverse of $g_{\alpha\beta}$, i.e. $g^{\alpha\beta}g_{\beta\gamma} = \delta^\alpha{}_\gamma$. Note that the Greek indices run over the spatial dimensions only.

This finally yields the equation

$$\ddot{x}^{\sigma} + \Gamma^{\sigma}{}_{\mu\nu}\dot{x}^{\mu}\dot{x}^{\nu} = 0 \tag{2.75}$$

where $\Gamma^{\sigma}{}_{\mu\nu}$ are the Christoffel symbols of the second kind.

This last equation describes the trajectories of classical photons in any media. At interfaces, where the optical parameters have a jump discontinuity, one must use Fresnel's laws, and possibly their generalization for curved interfaces [93].

We will now obtain the equations for our Gaussian deformation. The author of this essay would have expected that an analytical solution be available for the central Gaussian potential, but the non-linearity of the equations spoil the symmetry and the hopes of finding a solution. We will thus solve the equations in Cartesian coordinates for the centered formation:

$$n(x,y) = n_0 + \delta n \exp\left[-\frac{x^2+y^2}{2w^2}\right]. \tag{2.76}$$

In Cartesian coordinates, the six independent Christoffel symbols have value

$$\begin{aligned} \Gamma^{x}{}_{xx} &= \frac{n_x}{n} & \Gamma^{y}{}_{xx} &= -\frac{n_y}{n} \\ \Gamma^{x}{}_{xy} = \Gamma^{x}{}_{yx} &= \frac{n_y}{n} & \Gamma^{y}{}_{xy} = \Gamma^{y}{}_{yx} &= \frac{n_x}{n} \\ \Gamma^{x}{}_{yy} &= -\frac{n_x}{n} & \Gamma^{y}{}_{yy} &= \frac{n_y}{n} \end{aligned}$$

which yield the equations

$$\ddot{x} = \frac{x/w^2}{1+\frac{n_0}{\delta n}\exp\left[\frac{x^2+y^2}{2w^2}\right]}\left(\dot{x}^2-\dot{y}^2\right) + \frac{2y/w^2}{1+\frac{n_0}{\delta n}\exp\left[\frac{x^2+y^2}{2w^2}\right]}\dot{x}\dot{y} \tag{2.77a}$$

$$\ddot{y} = \frac{y/w^2}{1+\frac{n_0}{\delta n}\exp\left[\frac{x^2+y^2}{2w^2}\right]}\left(\dot{y}^2-\dot{x}^2\right) + \frac{2x/w^2}{1+\frac{n_0}{\delta n}\exp\left[\frac{x^2+y^2}{2w^2}\right]}\dot{x}\dot{y}. \tag{2.77b}$$

We seperate the two second-order equations in four first-order equations by defining $p_x = \dot{x}$ and $p_y = \dot{y}$. We solve the equations for photons coming in from $x(0) \to -\infty$ with $p_x(0) = \text{const}$ and $p_y(0) = 0$ for different values of the impact parameters $y(0) = b$. The results are shown in Fig. 2.13 and from this simple analysis we see that the deformation acts as a diverging lens.

From these equations, a more sophisticated algorithm could be developed to study the associated classical mechanics of inhomogeneous billiard systems, as was done in [94]. The algorithm would need to include collision detection with the boundary of the billiard as well as formulas for the reflection and transmission coefficients at this boundary.

2.5 Conclusion and Perspectives

This section solved the scattering problem of bidimensional dielectric cavities. Using information on the real k-line, the **Q**-matrix allows for the computation of the complex poles of the scattering

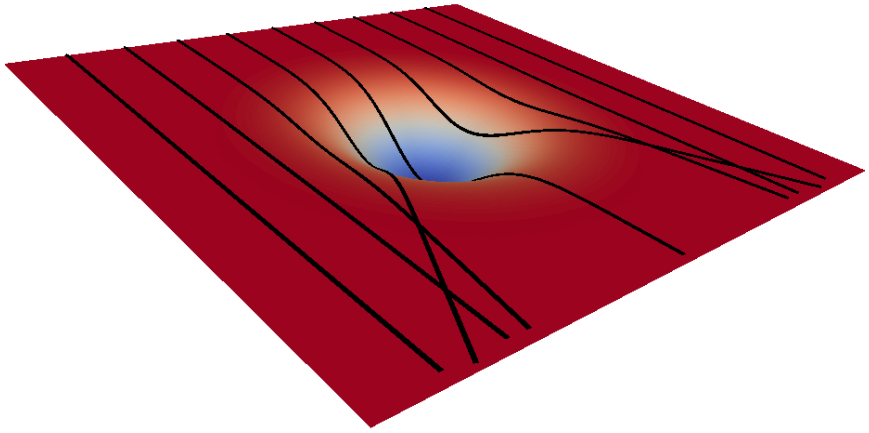

Figure 2.13 – Trajectories for photons of different impact parameters. The trajectories are the geodesics of the relevant "optical spacetime", where the curvature of space represents the optical distance that the photon has to traverse. The central region, where the refractive index is lower, acts as a diverging lens.

matrix, which in turn correspond to the resonances of the scatterer. The eigenvectors of the **Q**-matrix define a set of modes that exists for each real value of k. The eigenvectors which correspond to peaks in the time delay spectrum can be associated with the complex poles of $\mathbf{S}(k)$.

The formalism is coupled to a numerical method that computes the scattering matrix for inhomogeneous bidimensional cavities. The method is based on an onion-like discretization scheme where the solution of Helmholtz's equation can be reduced to an eigenvalue problem. This leads to the construction of local, or "shell scattering matrices". The boundary conditions allow to fuse the shells of the onion and compute the effect of the whole scatterer, viz. the scattering matrix.

The method is fast enough that it is possible to consider an optimization problem with one or several cost functions that quantify the performance of the scatterer for a given application. A few examples spring to mind, such as a dielectric optical switch, beam splitters, biosensors and others. If the material is active, one could optimize the form of the pump profile to minimize thresholds and maximizing, for instance, output directionality and power. This will be discussed in the following chapter.

One subject we have failed to mention in the main text is the fragility of the generalization of the SQA to complex energies k and potentials n; it also becomes computationally heavy. The details of the fragility are discussed in Appendix B.1. This, coupled to the instabilities related to the reconstruction of the field inside the scatterer has been a motivation to look for other numerical methods. In the next chapter, we will develop an *integral* method for the computation of the scattering matrix. This flexible method will be use of great use in discussing active material and 3D geometries.

Chapter 3

Active Media and Radiation

> Truth at last cannot be hidden. Dissimulation is of no avail. Dissimulation is to no purpose before so great a judge. Falsehood puts on a mask. Nothing is hidden under the sun.
>
> Leonardo da Vinci

The previous chapter set the stage for the study of the scattering of light on general, albeit passive, potentials. The relative simplicity of the geometry and of the physics allowed for a solution rich in physical information and lead to a rather simple numerical solution.

In the first section, we test the limits of the our analytical formalism and of our numerical advances. To more accurately model microlasers, we model the interaction of light with the underlying quantum gain medium, i.e. we solve the Maxwell-Bloch, or Schrödinger-Bloch, matter equations. We will specifically use the steady state *ab initio* laser theory, or SALT, a recently formulated steady state laser theory. In this theory, the effect of the active medium is reduced to an additional frequency and pump-dependent term in the refractive index. This extra term has a Lorentzian frequency dependence, as physically expected, and has non-zero real and imaginary parts. The fragility of our extension of SQA is then exposed and an integral method is developed to replace it.

The second section studies the experimental response of different realizations of a specific type of antenna known as leaky coax antennae (LCXs). The genesis of this study lies in the hopes of designing an antenna that can be seamlessly integrated into textile. The sheer complexity of the antenna, as we will show, bars the use of the methods developed in this essay in favour of an all-numerical method, the FEM. This particular choice will be motivated and the design parameters

of the antenna thoroughly explained.

3.1 Lasing and Scattering

A recently formulated laser theory, named the SALT and developed by A. D. Stone's group at Yale, has been shown to be an accurate model of the light-matter interaction involved in bidimensional microlasers. Its steady-state nature allows us to apply the formalism developed in the previous section to the theory. However, in light of the several shortcomings of the SQA's numerical implementation, we have dveloped another numerical method. To find a more robust solution, we completely forgo differential equations in favour of integral ones. Our brief incursion into the rich field of integral equations is a rather recent one, and might leave the reader hungry for more.

3.1.1 Primer on Steady State ab initio Laser Theory (SALT)

We briefly expose the parts of SALT that we will need. Our exposition of SALT is divided into two main sections: the first describes the details of the interaction of light with the quantum gain medium and provides a steady-state solution of the resulting Maxwell-Bloch equations. The second discusses the constant-flux states and their computation using the aforementioned numerical methods. This section is based in part on [56, 57, 95].

(a) Solving the Matter Equations Our starting point, as always, is

$$\nabla \times \boldsymbol{E} = ik\mu\boldsymbol{H}; \qquad \nabla \times \boldsymbol{H} = -ik\epsilon\boldsymbol{E} - ik\boldsymbol{P}^{NL} \tag{3.1}$$

where $\boldsymbol{P}^{NL}$ now represents the possibly non-linear response of the underlying quantum gain medium to the electric field $\boldsymbol{E}$. We separate the fields in transverse and longitudinal components, as we did for the passive cavities. Assuming that the propagation constant β vanishes, we can separate two polarization states and write decoupled differential equations for the longitudinal components of the fields

$$\left[\nabla^2 + k^2 n^2\right] E_z = \frac{1}{\mu}\nabla E_z \cdot \nabla\mu - k^2\mu P_z \tag{3.2.TM}$$

$$\left[\nabla^2 + k^2 n^2\right] H_z = \frac{1}{\epsilon}\nabla H_z \cdot \nabla\epsilon - \frac{ik}{\epsilon}\boldsymbol{P}^{NL} \times \nabla\epsilon - ik\nabla \times \boldsymbol{P}^{NL} \tag{3.2.TE}$$

where the last equation is the *proper* generalization for TE modes [1]. To derive these equations, we made the implicit assumptions that the non-linear electric susceptibility tensor,

$$\boldsymbol{P}^{NL} = \boldsymbol{\chi_e}^{NL}(\boldsymbol{r}; \omega)\boldsymbol{E}(\boldsymbol{r}), \tag{3.3}$$

is either a diagonal tensor or a scalar. In the TM polarization, $E_r = E_\theta = 0 \Rightarrow P_r = P_\theta = 0$, such that $\boldsymbol{P}^{NL}$ has a single non-zero component, P_z, while it is the the P_r and P_θ components that are

[1] In the SALT literature, it is always said that the generalization to TE is "trivial", or "follows immediately". This is far removed from the truth. The TE differential equation is completely different from the TM one.

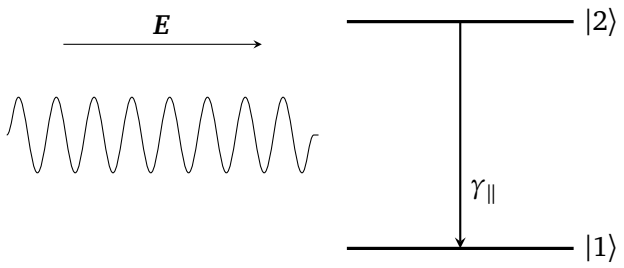

Figure 3.1 – Pictorial representation of the interaction between the quantum gain medium and the incoming field. The quantum system has two levels, the wavefunction being either $|1\rangle$ or $|2\rangle$. The relaxation rate from level 2 to level 1 is given by $1/\gamma_{\parallel}$.

non-zero in the TE polarization. The vectors resulting from the cross-product and curl in (3.2.TE) possess only a z-component, as needed.

To go any further, we must compute the value of the non-linear electric susceptibility tensor [96]. To show the main features of the theory, we assume a two-level quantum system as the gain medium, although the method is generalizable to multi-level systems [57, §2.3].

Solving Schrödinger's equation for a "bare", i.e. non-interacting two-level system yields

$$H_0 |j\rangle = \omega_j |j\rangle \qquad j = 1,2 \tag{3.4}$$

and corresponding eigenfunctions $|1\rangle$ and $|2\rangle$. The incoming light field acts as a perturbation and source of energy that stimulates a population transfer from level 1 to level 2 decaying at a rate $1/\gamma_{\parallel}$. The perturbation can be written as

$$H_1 = e\boldsymbol{\mu}\cdot\boldsymbol{E} \tag{3.5}$$

where e is the electric charge and $\boldsymbol{\mu}$ is the dipole moment tensor of the material. We expand the solution of the perturbed system in the states of the unperturbed system

$$|\psi_1(t)\rangle = C_1(t)|1\rangle + C_2(t)|2\rangle \tag{3.6}$$

and form the density matrix

$$\rho(t) = |\psi_1(t)\rangle \langle\psi_1(t)| . \tag{3.7}$$

It allows us to solve the problem for an ensemble of two-level systems [57]. Using the well-known evolution equations of the density matrix [97, §6.2] and defining $D = \rho_{22} - \rho_{11}$, the population difference between the two levels, we obtain the equations [98, §5.3]

$$\dot{\boldsymbol{P}}^{NL} = -(i\omega + \gamma_{\perp})\boldsymbol{P}^{NL} + \frac{g^2}{i\hbar}\boldsymbol{E}D \tag{3.8}$$

$$\dot{D} = \gamma_{\parallel}(D_0 - D) - \frac{2}{i\hbar}\boldsymbol{E}\cdot\boldsymbol{P}^{NL} \tag{3.9}$$

where g^2 is the dipole moment of the system, $\gamma_{\perp}$ is an *ad hoc* phenomenological damping term that comes from the interaction of the ensemble of two-level systems[2] and D_0 is the equilibrium

[2]The author surmises that it could be computed with a mean field approximation.

population. The approach uses a rotating wave approximation (RWA), but, contrary to most derivations, does not invoke the slowly varying envelope approximation (SVEA). One of the main approximations, one that is necessary to make ground, is the stationary inversion approximation (SIA), i.e. $\dot{D} = 0$. Writing the fields as Fourier series

$$\boldsymbol{P}^{NL} = \sum_{\mu} \boldsymbol{p}_{\mu} e^{-ik_{\mu}t} \qquad\qquad \boldsymbol{E} = \sum_{\mu} \boldsymbol{\Psi}_{\mu} e^{-ik_{\mu}t}$$

leads to the relationship[3]

$$\boldsymbol{p}_{\mu} = \frac{g^2}{\hbar} \frac{1}{k_{\mu} - k + i\gamma_{\perp}} \frac{D(\boldsymbol{r})}{1 + \sum \frac{4g^2}{\gamma_{\perp}\gamma_{\parallel}} \Gamma(k_{\mu}) \left|\Psi_{\mu}(\boldsymbol{r})\right|^2} \boldsymbol{\Psi}_{\mu}(\boldsymbol{r}). \tag{3.10}$$

In the TM polarization, this leads to the equation

$$\left[\nabla^2 + k^2 \left(\epsilon(\boldsymbol{r}) + \frac{g^2}{\hbar} \frac{1}{k_{\mu} - k + i\gamma_{\perp}} \frac{D(\boldsymbol{r})}{1 + \sum_{\mu} \frac{4g^2}{\gamma_{\perp}\gamma_{\parallel}} \Gamma(k_{\mu}) \left|\Psi_{\mu}(\boldsymbol{r})\right|^2}\right)\right] \Psi_{\mu}(\boldsymbol{r}) = 0 \tag{3.11}$$

where

$$\Gamma(k_{\mu}) = \frac{\gamma_{\perp}^2}{(k - k_{\mu})^2 - \gamma_{\perp}^2} \tag{3.12}$$

$\Psi_{\mu}(\boldsymbol{r})$ is the longitudinal component of the field.

(b) Constant-flux States and Threshold Lasing Modes The derivation above, novel to SALT and slightly more accurate than the standard derivations [56, 57, 99], shows that the effect of the quantum gain medium can be modeled as an extra term in the refractive index in the TM polarization, but leads to an altogether different differential equation in the TE polarization. To the author's knowledge, this is never specifically addressed in the SALT articles. In the following, we will also focus on the TM polarization.

The central feature of SALT is the introduction of the constant-flux (CF) states, which are defined by

$$\left[\nabla^2 + \epsilon(\boldsymbol{r}) K^2(k)\right] \psi(\boldsymbol{r}) = 0 \qquad \boldsymbol{r} \in \mathscr{C} \tag{3.13a}$$

$$\left[\nabla^2 + \epsilon(\boldsymbol{r}) k^2\right] \psi(\boldsymbol{r}) = 0 \qquad \boldsymbol{r} \notin \mathscr{C} \tag{3.13b}$$

where $\mathscr{C}$ is the cavity region. Inside $\mathscr{C}$, the frequency $K(k)$ is allowed to be complex, but outside the cavity we force k to be real. This allows us to bestow physical meaning unto the CF states, as they do not suffer from the exponential growth of the QB states. Despite the non-linearity of the equations, the CF states can be used as a basis for the laser modes, and can even take into account saturation, spatial hole burning and non-uniform pumps through the

$$\frac{D(\boldsymbol{r})}{1 + \sum_{\mu} \frac{4g^2}{\gamma_{\perp}\gamma_{\parallel}} \Gamma(k_{\mu}) \left|\Psi_{\mu}\right|^2}$$

[3] We have skipped some steps. See [57, §2.2] for details.

term. If we restrict our analysis to near-threshold modes, where the lasing field intensity is very low, we can neglect the interaction between the different modes. This allows us to entirely neglect the summation from the previous term and, writing the pump profile as a pump strength multiplied by a shape function $D(\boldsymbol{r}) = D_0 F(\boldsymbol{r})$, we obtain

$$\left[\nabla^2 + k^2\left(\epsilon(\boldsymbol{r}) + \frac{\gamma_\perp D_0 F(\boldsymbol{r})}{k_\mu - k + i\gamma_\perp}\right)\right]\psi(\boldsymbol{r}) = 0 \qquad \boldsymbol{r} \in \mathscr{C} \tag{3.14}$$

where now the fields and the pump strength are dimensionless parameters measured in units of $e_c = \hbar\sqrt{\gamma_\parallel \gamma_\perp}/(2g)$ and $D_{0c} = \hbar\gamma_\perp/(4\pi g^2)$, respectively. Notice that $\gamma_\parallel$ does not appear explicitly in our set of equations; it has become a mere scaling factor [57, p. 19–20]. The solutions of this equation describe the lasing action near lasing thresholds, the threshold lasing modes (TLMs). In the case of uniform pumping, i.e. $F(\boldsymbol{r}) = 1$, the CFs are in a one-to-one correspondence with the TLMs, as we can see by comparing (3.13a) and (3.14). To find the TLMs, one needs to compute the CF states, find the values of $K^2(k)$ and infer the values of D_0. When the exterior frequency k is such that D_0 is real, the resulting couple (k_a, D_0^a) reveals the frequency and threshold of the lasing mode. This was done in [3].

However, we will mostly be interested in the case of non-uniform pumping and/or inhomogeneous refractive index distribution. To find the couple (k_a, D_0^a), we must solve (3.14) self-consistently for a real value of D_0 such that a pole of scattering matrix hits the real k-line. In the following, we develop a method that allows us to compute the **S**-matrix for complex potentials.

3.1.2 Numerical Method II: Lippmann-Schwinger

Seeing the differential methods fail, the author of this essay took notice of the power of integral methods. Simply rewriting Helmholtz's equation as

$$\left[\nabla^2 + n_0^2(\omega)k^2\right]\psi = -k^2\Delta n^2(\boldsymbol{r};\omega)\psi \tag{3.15}$$

where

$$\Delta n^2(\boldsymbol{r};\omega) = n_c^2(\boldsymbol{r};\omega) - n_0^2(\omega) \tag{3.16}$$

where $n_c^2(\boldsymbol{r};\omega)$ is the permittivity profile of the scatterer and $n_0^2(\omega)$ the constant permittivity of the environment, or background. This allows to write a formal solution using the Green's function of Helmholtz's equation

$$\psi(\boldsymbol{r}) = \phi(\boldsymbol{r}) - k^2 \iint_{\mathscr{C}} G_+(\boldsymbol{r},\boldsymbol{r}')\Delta n^2(\boldsymbol{r}';\omega)\psi(\boldsymbol{r}')d^2\boldsymbol{r}' \tag{3.17}$$

where $\phi(\boldsymbol{r})$ is a solution of the homogeneous problem and

$$G_\omega(\boldsymbol{r},\boldsymbol{r}') = -\frac{i}{4}H_0^{(\omega)}(kn_0|\boldsymbol{r}-\boldsymbol{r}'|). \tag{3.18}$$

While (3.17) is very general (it can be applied to any $\Delta n^2(\boldsymbol{r};\omega)$, even to non-linear ones), the method of solution we will use restricts us to linear problems.

Instead of a partial differential equation (PDE), we now must solve an implicit integral equation for the field. It is a Fredholm equation of the second kind with a weakly singular, compact operator. This ensures the existence and uniticity of the solution [50, 100]. We solve the surface integral equation in real space by meshing the cavity $\mathscr{C}$. The details of the meshing is left to Appendix B.2. Let us denote the set of cells of our mesh by Δ. We can thus cast the integral equation as

$$\psi_j = \phi_j - k^2 \sum_{j' \in \Delta} G_{jj'} \Delta\epsilon_{j'} A_{j'} \psi_{j'} \tag{3.19}$$

where $\psi_j = \psi(\boldsymbol{r}_j)$ and similarly for the other quantities and where A_j is the area of cell j. We can rewrite this as the matrix problem[4]

$$(\mathbf{I} + \mathbf{K})\boldsymbol{\psi} = \boldsymbol{\phi}. \tag{3.20}$$

where

$$K_{jj'} = G_{jj'} \Delta\epsilon_{j'} A_{j'}. \tag{3.21}$$

The matrix equation is then solved using any good linear algebra solver. This yields values for the field inside the scatterer. The integral equation is then explicit for the field outside the scatterer. Our interest, however, still lies in the computation of the scattering matrix. It turns out that, if we use

$$\phi = J_M(kr)e^{iM\theta} \tag{3.22}$$

as the "incoming" field, one may find that the scattering matrix can be computed via

$$S_{Mm} = \delta_{Mm} - \frac{ik^2}{2} \iint_{\mathscr{C}} e^{-im\theta'} J_m(kr') \Delta\epsilon(\boldsymbol{r}') \psi^{(M)}(\boldsymbol{r}') d^2\boldsymbol{r}'. \tag{3.23}$$

In Appendix B.2, we lay out the method in more detail, discuss the numerical implementation and present a generalization for the complete vectorial electromagnetic fields.

3.1.3 Examples

To demonstrate the method, we compute a lasing mode of the homogeneous, circular cavity laser. We take $k_\mu = 9.25$ and $\gamma_\perp = 0.125$ and compute the threshold of a particular lasing mode. This is done by following the upwards movement of the poles of the scattering matrix as D_0 is increased. We show the determinant of the **S**-matrix of the system for $D_0 = 0.027$ in Figure 3.2. There is a lasing mode at $k = 9.37343358$. It has a low lasing threshold mainly because of the extremely high Q-factor of its related QB state [3].

While we see that one of the poles has moved directly onto the real k-axis and is therefore a physical lasing mode, perhaps the most striking feature of the pole structure is the movement

[4] This, of course, only holds if the kernel is linear.

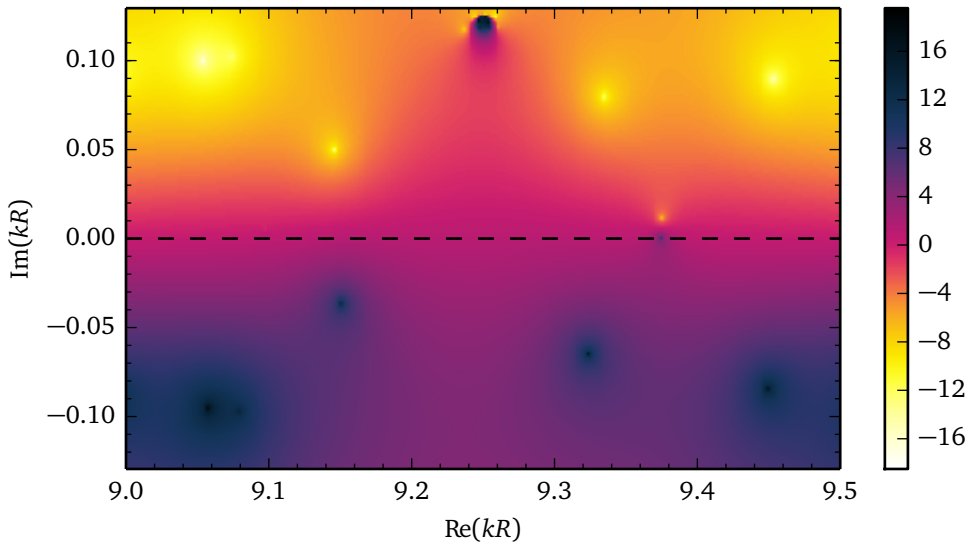

Figure 3.2 – Map of the determinant of the **S**-matrix of the homogeneous, circular cavity laser. We have used $n_c = 3.2$, $n_o = 1$ and $R_0 = 1$. The gain transition parameters are $\gamma_\perp = 0.125$ and $k_\mu = 9.25$. This yields a threshold of $D_0 = 0.027$ for the mode at $k = 9.37343358$.

of the other poles (contrast with Figure 2.4). As we had predicted in section on the properties of the **Q**-matrix (p. 20), the poles are still symmetric, but along a curve in the complex k-plane rather than along the real k-line. Although it is difficult to derive the exact form of the curve, we can see that it is of Lorentzian shape, as is the imaginary part of the refractive index. Notice also the clustering of zeros and poles at $k = 9.25$, the centre of the gain transition. This is where the refractive index change is the highest.

3.2 Smart Textile Antennae

The last part of this essay recounts the author's contributions in a project involving the design and theoretical characterization of fibre-antennas. This section departs a little from the more theoretical and numerical musings of the others and presents both the modeling of the antennae and their experimental characterization.

The goal of the original project was to develop an antenna that is compatible with WiFi standards (i.e. emits at $f = 2.45\,\text{GHz}$) and can be easily integrated to textile. These two requirements impose multiple restrictions on both the materials that can be used and the geometry of the antenna. For instance, we would like the antenna to be spun directly into the textile as to have, so to speak, a seamless integration of the antenna.

Most solutions today merely affix a patch antenna to a less encumbered part of the textile [101, 102], e.g. on the shoulder pads of a shirt or the front of a t-shirt. A metallic plate shields the user from the electronic components of the patch antenna. Because the properties of patch

antennas are well known [103], very little engineering is required and this solution is thus quite cheap[5]. However, integration with the textile is far from seamless, as it is very apparent to the user that he has become a giant walking antenna. Our project thus strives to find antenna designs that have emission properties as flexible as a patch antenna's while improving textile integration as to make it transparent to the user.

The concept of a fibre-antenna rapidly established itself as an ideal solution in our research group, as it provides a rich architecture upon which to build. A fibre-antenna has the potential of having good mechanical properties, of shielding the electronic components from both the user and the washing machine and can be loaded directly unto the spools that deliver textile to industrial looms, making it both easy to manufacture and transparent to the user.

Before showing the details of our contribution, we will first show the important quantities when working with antennas, and more importantly the design parameters.

3.2.1 Basic Antenna Theory

Even today, a full 140 years after the publication of Maxwell's seminal *Treatise on Electricity and Magnetism*, the electromagnetic modeling of radiating structures is an ongoing research problem. The notorious difficulty of solving Maxwell's equations seriously hampers analytical efforts and, due to the nature of electromagnetic radiation, numerical progress is not easier to achieve.

In what follows, we present the Stratton-Chu equations, a rigorous solution of Maxwell's equations which relates the electric and magnetic fields to the currents and charges that "produce" them. They can alternatively compute the fields in all space if they are known on any given surface(s).

3.2.1.1 Stratton-Chu Solution

In antenna problems, we want to compute the field values as a function of the sources that contribute to these fields. From electrostatics, we know that a current density $\boldsymbol{J}$ gives rise to a magnetic field and a charge density ρ gives rise to an electric field. In the time-varying picture, the electric and magnetic fields become coupled and we take the viewpoint that the $\boldsymbol{J}$ and ρ give rise to both electric and magnetic fields.

To compute the field from these sources, which are presupposed to exist, we must use the Stratton-Chu integrals. The derivation is standard, so we refer to [103]. Consider a volume V of free space containing sources and possibly excluded sub-volumes V_i bound by surfaces S_i that contain matter of some kind. By the use of Green's and Stokes' theorems and other vectorial

[5]The general availability of consumer-grade "smart" textile on the Web should suffice to prove this point.

identities, we find that the field outside the excluded sub-volumes can be expressed as

$$\boldsymbol{E} = \frac{1}{4\pi}\iiint_V (\rho\nabla G + i\omega G\boldsymbol{J})\,dV + \frac{1}{4\pi}\oiint_{S_1,\cdots,S_N} [\boldsymbol{n}\cdot\boldsymbol{E}\nabla G + (\boldsymbol{n}\times\boldsymbol{E})\times\nabla G + i\omega G(\boldsymbol{n}\times\boldsymbol{H})]\,dS \tag{3.24a}$$

$$\boldsymbol{H} = \frac{1}{4\pi}\iiint_V \boldsymbol{J}\times\nabla G dV + \frac{1}{4\pi}\oiint_{S_1,\cdots,S_N} [-i\omega G(\boldsymbol{n}\times\boldsymbol{E}) + (\boldsymbol{n}\times\boldsymbol{H})\times\nabla G + (\boldsymbol{n}\cdot\boldsymbol{H})\nabla G]\,dS \tag{3.24b}$$

where G is the Green's function of the problem

$$G(\boldsymbol{r},\boldsymbol{r}') = \frac{e^{ik|\boldsymbol{r}-\boldsymbol{r}'|}}{4\pi|\boldsymbol{r}-\boldsymbol{r}'|}. \tag{3.24c}$$

These two equations are rigorous solutions of Maxwell's equations. They can be used with any antenna and provide ways to compute the current distribution if it is unknown (constitutes an integral equation in the current[6]) and can be used to compute the far-field of antennae when either (i) the current distribution is known or (ii) the near-field around the antenna is known. These two properties discriminate antennae into two categories, denoted Type I and Type II.

Type I antennae have a well-approximated current distribution, which means that there are no sub-volumes to be excluded and therefore no surface integrals in expressions (3.24a) and (3.24b).

On the other hand, Type II antennae have well-approximated near-fields, leading us to exclude the volume containing the antenna. Expressions (3.24a) and (3.24b) contain only surface integrals, then.

We will give examples relating these two types of antennae to the Stratton-Chu equations when we have defined the antenna parameters.

3.2.1.2 Antenna Parameters

In the design of our antenna, we will want to optimize the value of some parameters. We will now describe some of these parameters.

(a) Directivity and Gain [103, §1.16] Given a radiation pattern measured (in the far-field) as the power density $\mathscr{P}(\theta,\varphi)$, we can define its *directivity* as

$$D(\theta,\varphi) = \frac{4\pi\mathscr{P}(\theta,\varphi)}{\int_0^\pi\int_0^{2\pi}\mathscr{P}(\theta',\varphi')\sin\theta' d\theta' d\varphi'}. \tag{3.25}$$

The value of the directivity is less than unity if the power density radiated at angle (θ,φ) is less than the average power radiated. For instance, an isotropic antenna will possess a unit directivity

[6] This is the basis of the popular computational method known as the *method of moments* [103, §7.5].

for all angles while a highly directional antenna will have a sharp peak in its directivity function at some angle (θ^*, φ^*).

Another interesting concept to introduce is *partial directivity*. The power density can be divided into two contributions: the θ- and φ-polarized contributions and we can write

$$\mathscr{P}(\theta,\varphi) = \mathscr{P}_\theta(\theta,\varphi) + \mathscr{P}_\varphi(\theta,\varphi) \tag{3.26}$$

where the subscripts indicate the polarization state. The partial directivities hence follow

$$D(\theta,\varphi) = D_\theta(\theta,\varphi) + D_\varphi(\theta,\varphi). \tag{3.27}$$

We can also introduce the gain, which characterizes the loss and the directivity of the antenna simultaneously. It is simply given as

$$G(\theta,\varphi) = \frac{4\pi r^2 \mathscr{P}(\theta,\varphi)}{P} \tag{3.28}$$

where P is the power fed into the antenna. Because of the losses,

$$P/r^2 \geq \int_0^{\pi}\int_0^{2\pi} \mathscr{P}(\theta',\varphi')\sin\theta' d\theta' d\varphi'$$

such that $G(\theta,\varphi) \leq D(\theta,\varphi)$.

We can also define partial gains in the exact same fashion we defined partial directivities.

Radiation efficiency η is defined as the ratio of the total radiated power to the power accepted by the antenna [104].

Example 3.1 (Dipole Antenna [103])**.** Perhaps the most basic antenna design, it has the form shown in Figure 3.3.

It is also called the slender dipole antenna, as we consider the limit where the diameter of the wire is much smaller than the wavelength, making the dipole antenna a 1-dimensional problem. The current flowing through the dipole can be approximated by

$$I(z) = I_m \sin[k(\ell - |z|)] \tag{3.29}$$

where I_m is the intensity of the current. It is thus categorized as a Type I antenna. We can use the volumetric part of the Stratton-Chu solution to compute the far-field of such antennae. Introducing a directional weight function $\mathscr{A}_{\{\theta,\varphi\}}$ such that

$$\mathscr{P}_{\{\theta,\varphi\}}(\theta,\varphi) = \left|\mathscr{A}_{\{\theta,\varphi\}}\right|^2 \tag{3.30}$$

and using the far-field approximation of the Green function in Stratton-Chu's equation, we obtain

$$\mathscr{A}_\theta(\theta) = -I_m \sin\theta \int_{-\ell}^{\ell} \sin[k(\ell - |z|)]\, e^{ikz\cos\theta} dz \tag{3.31}$$

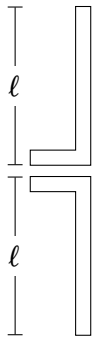

Figure 3.3 – Geometry of the dipole antenna. It consists of a pair of thin wires whose diameters are much smaller than their length ℓ. They are actually separated by an infinitesimal spacing. It has been made visible for the drawing. Current is fed to the antenna from one of the incoming wires. The z-coordinate has its origin directly between the two wires.

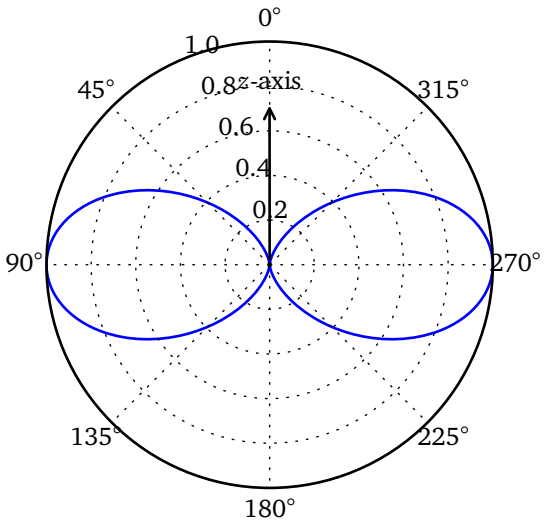

Figure 3.4 – Cross-section of the 3D far-field of the half-wave dipole antenna.

which can be integrated to yield

$$\mathscr{A}_\theta(\theta) = -\frac{2I_m}{k\sin\theta}\left[\cos(k\ell\cos\theta) - \cos(k\ell)\right]. \tag{3.32}$$

This is the functional form of the field on the azimuthal great circle as the radius of the sphere goes to infinity. Figure 3.4 shows a cross-section of the 3D far-field along any φ for the half-wave dipole antenna ($\ell = \lambda/4$).

Example 3.2 (Near- to Far-Field Transformation)**.** If, instead of knowing the currents and charges in a given volume V, we know the fields on the boundaries S_i of a given number of volumes V_i in which there (supposedly) exist unknown charges and currents producing those fields, we can use the boundary terms in the Stratton-Chu equation to compute the field outside the antenna. This often arises when using FEM and finite-difference time-domain (FDTD) software, as both

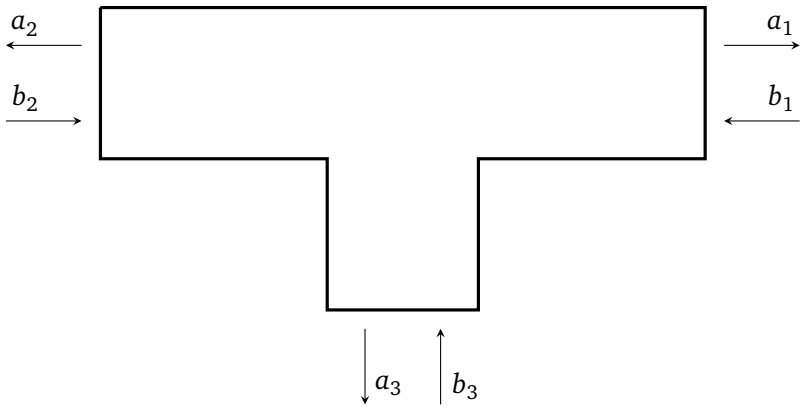

Figure 3.5 – Example of a 3-port network. The "ends" of the structure are generally used at its ports.

methods solve the fields in a given computational volume. The far-field is not directly available to them, as this would require a very large computational volume. Usually, then, one can specify a boundary which encloses all scattering objects (the last scattering surface). Since the fields are known, we can use the surface part of (3.24a) together with the far-field expansion of $G(\boldsymbol{r}, \boldsymbol{r}')$ to compute the far-field via a simple quadrature of the near-field. For instance, this is how the commercial software COMSOL computes the far-field.

In our previous example, we could define the last scattering surface as the cylinder enclosing the whole of the dipole antenna. The Stratton-Chu integrals can then be evaluated with the known field on the cylinder and yield the far-field.

(b) Scattering Parameters The scattering parameters (or S-parameters) are usually defined through a linear N-port network. Suppose we have an electronic device comprising N ports, or points of entry. Imagine shining light onto, or make a current flow into, one of the ports, say port j. A certain percentage of the power carried by this light/current will be reflected by this port and the rest will be transmitted to the other ports or absorbed in the medium. The *reflection* coefficients are given by S_{jj} while the transmission coefficients are given by S_{ji} $(i \neq j)$ where $\mathbf{S}$ is the scattering matrix of the network. In a reciprocal (in the sense of Lorentz) network, the scattering matrix will be equal to its transpose, i.e. $S_{ij} = S_{ji}$. In a lossless network, the scattering matrix will be unitary.

This is, of course, highly reminiscent of the scattering operator in quantum-mechanical scattering which relates the outgoing (scattered) components to the incoming (incident) components

$$|\Psi_{\text{out}}\rangle = \mathscr{S}\,|\Psi_{\text{in}}\rangle\,. \tag{3.33}$$

In this case, the "ports" are the different angular momenta components rather than physical input/output connections. The precise nature of ports is somewhat arbitrary in optical structures.

3.2.2 The Leaky Coaxial Cable

A standard antenna design, the leaky coaxial cable, or LCX, will be the primary object of our present study. Its relatively simple design: a coaxial cable from which some parts of the metal coating are removed as to form "windows", made it a safe choice to toy with both the experimental fabrication procedure and the numerical modeling. Usual LCXs are much longer than the wavelength at which they are meant to operate, with a unit cell (see Figure 3.6) of comparable size.

Our antennae, contrary to typical LCXs, have lengths similar to that of the operating wavelength. Figure 3.6(a) shows a cross-section of a typical LCX antenna and Figure 3.6(b) shows a top view of the fibres our group actually made. They all contain three windows of varying widths S_z and distance between windows d_z, making for fibres having all approximately $L \sim 24\,\text{cm}$. Table 3.1(a) shows the geometrical parameters of the fabricated antennae, while Table 3.1(b) shows the physical parameters of the materials involved.

(a) Modeling LCXs The modelization of LCX is not a new field [105–108]. They have been studied using a variety of analytical and numerical methods. Most of them depend on a set of *crucial* approximations that cannot be assumed to hold in our particular case:

Periodicity of the structure The z-periodicity of the geometry and and material parameters paves the way for a Floquet-Bloch expansion of the fields. This is used in [106].

Narrow slits A perturbation theory, where slits are supposed to be small as compared to the wavelength, $kS_z \ll 1$, is used in [107].

Transmission line behaviour One of the most important approximation, it stipulates that the LCX supports a single TEM propagating mode. This allows the unambiguous use of scalar voltages and currents as the physical observables [109]. It also allows the use of simpler numerical methods, such as using the overlap between the propagating mode and the radiation continuum to quantify the radiation properties [108, 110].

In our case, the worst offender is the last one, as our metal deposition method does not allow for a fine control of the thicknesses deposited, nor ensure its smoothness. The TEM approximation depends on the metal layers behaving almost as perfect conductors. Our metallic layers are typically smaller than the skin depth of the metal, which makes the approximation invalid (we will explore this later in this essay).

Moreover, we cannot consider the structure to be periodic, as the total length of the fibre-antenna is of the order of the wavelength ($\lambda \sim 12\text{cm}$) and the period of the slots is smaller than the wavelength. Given the size of the slots, the author is comfortable to say that we neither are in

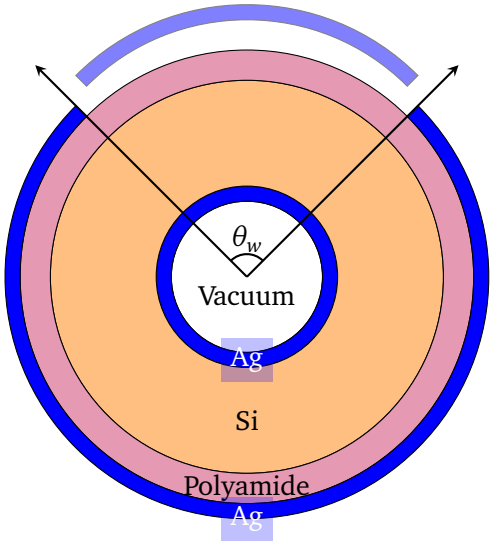

(a) View of the cross-section: in order of increasing radius, we have: vacuum, silver, silica, polyamide and silver. We have shown a cross-section where there is a "window". When there are no windows, the outer silver layer takes up the entire circumference of the fiber. θ_w is the angular size of the windows.

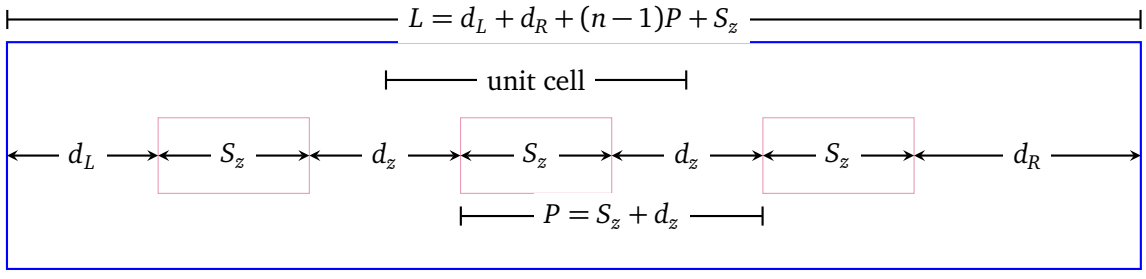

(b) Top view: the positions of the windows are usually asymmetric, i.e. $d_L \neq d_R$. The distance between the windows is given by d_z and the length of the windows are S_z. We notice that the length of the fibre is given by $L = d_L + d_R + (n-1)P + S_z$ where $P = S_z + d_z$ is the period between windows and n is the number of windows.

Figure 3.6 – Geometry of the fibre-antenna

the perturbation regime. Figure 3.6 shows the actual design and the important parameters. We will use the fact that the first radiation harmonics of a LCX is given by the relation [106]

$$f_1 = \frac{c}{P\left(\sqrt{\epsilon_r}+1\right)} \tag{3.34}$$

to guide the numerical modeling.

(b) Specifications of the Devices To be able to theoretically investigate the behaviour of these antennas, we must know their physical and geometrical properties. The parameters of the dielectric materials are provided by the manufacturer of the optical fibres we use as a building platform, Polymicro Technologies, and are reproduced in Table 3.1.

The thickness of the metallic layers is more delicate and depends on the minute details of the deposition method. As a first approximation, we can compute the thicknesses by measuring the D.C. resistance of the inner and outer layers of silver and using the relation [111, p. 204]

$$R = \frac{L}{\sigma A} \tag{3.35}$$

where L is the length of the fibre, σ the conductivity of the silver layer and A its area. For the inner and outer layers, we have

$$A_{\text{inner}} = \int_0^{2\pi}\int_{t_{\text{vac}}-t_{\text{Ag1}}}^{t_{\text{vac}}} r\,dr d\theta = \pi\left(2t_{\text{vac}}t_{\text{Ag1}} - t_{\text{Ag1}}^2\right) \tag{3.36}$$

$$A_{\text{outer}} = \int_0^{2\pi}\int_{T}^{T+t_{\text{Ag2}}} r\,dr d\theta = \pi\left(2T t_{\text{Ag2}} + t_{\text{Ag2}}^2\right) \tag{3.37}$$

where $T = t_{\text{vac}} + t_{\text{Ag1}} + t_{\text{Si}} + t_{\text{pyamide}}$. Substituting these results into (3.35) yields

$$-t_{\text{Ag1}}^2 + 2t_{\text{vac}}t_{\text{Ag1}} - \frac{L}{\sigma_{\text{Ag0}}\pi R_{\text{inner}}} = 0 \tag{3.38a}$$

$$t_{\text{Ag2}}^2 + 2T t_{\text{Ag2}} - \frac{L}{\sigma_{\text{Ag0}}\pi R_{\text{outer}}} = 0 \tag{3.38b}$$

where the Rs are the measured D.C. resistances for each shell. This can readily be solved using the quadratic equation. Using the bulk conductivity of silver (see Table 3.1(b)) yields the thicknesses found in Table 3.1(a).

Notice that this assumes smooth metallic layers (no surface inhomogeneities) and constant conductivity within the whole volume. We will return to this assumption shortly.

(c) Choice of simulation software The LCXs to be modeled have a decidedly complex geometry that do not possess any symmetry and metallic layers of high, though not infinite, conductivity. To properly take the effects of both situations into account, one would need, at the very least, to use multi-scale discretization techniques. Unfortunately, the extremely wide range in the characteristic sizes of the structures (from the nanometer to the millimeter) makes meshing the LCX

Table 3.1 – Geometric and physical parameters of the LCX antennae. Units are repeated from column above if not indicated.

(a) Geometric parameters of the fibre designs. The thicknesses of the layers are listed in order, starting from the inner layer to the outer layer of the fibre-antenna.

Quantity	Unit	RF21	RF27[1]	RF29	RF33
t_{vac}	μm	99.874	99.900	99.646	99.924
t_{Ag1}		0.126	0.100	0.354	0.0766
t_{Si}		273	273	273	273
t_{pyamide}		24	24	24	24
t_{Ag2}		0.101	0.100	0.306	0.030
d_L	mm	27	30	31	30.91
d_R		55	55	55	54.72
S_{z1}[2]		32	34	33	34.36
S_{z2}		32	34	34	34.06
S_{z3}		32	34	33.5	33.87
d_{z1}		28	28	29	27.44
d_{z2}		28	28	28.5	28.36
L	cm	30.0	24.3	24.4	24.372
θ_w	deg	180	180	180	180
R_{inner}	Ω	60.0	—	60	80.5
R_{outer}		20.0	—	20	59.8

[1] Measurements are approximate; values for the inner and outer resistances were lost. We assume they are identical to the RF29. [2] Each window has a different S_z and d_z.

(b) Physical parameters of the materials used in the fibre-antennae.

Quantity	Unit	Value
ϵ_{Si}	–	3.77
$\epsilon_{\text{pyamide}}$	–	3.50
σ_{Ag0}	MS/m	63.0
σ_{AgO0}		6.79
λ_{Ag}	nm	40

geometry a Herculean, if not even Sisyphean, task. The issue of meshing thin silvers layers has already been solved in the literature and involves replacing the silver shells by appropriate boundary conditions [112].

The two requirements discussed above essentially destroy all hope of using any of the methods we have devised in the last sections of this essay. The eigenbasis expansions suffer from poor mesh control[7], direct integration Helmholtz's or Maxwell's equations is usually unstable[8] and it is notoriously difficult to incorporate boundary conditions naturally in the framework of the Fredholm integral methods [113, 114]. This leaves us with two choices: the FDTD method and the FEM. The former can deal with arbitrary boundary conditions rather easily, but generates a fixed scale mesh [115]. The latter, by the use of the weak form of Maxwell's equations, can easily incorporate any type of boundary conditions and work with multi-scale and even adaptive meshes. We thus use the commercial FEM software Ansys HFSS to model the frequency response of the

[7] There exists, for instance, algorithms that compute the Discrete Fourier Transform for non-uniform samples, and such endeavors are worthwhile, but their sizable numerical cost and their only slightly better mesh control is not worth their effort in our particular case.

[8] Not always however, as the FDTD method does just that. It requires, however, some numerical legwork.

the LCX antennae.

The software comes with bundled CAD capabilities. To model the LCXs, we draw a coax cable inside a cylinder of larger radius that acts as the "environment". Its borders are terminated by perfectly matched layers, or PMLs [116], that absorb the field emanating from the antenna. They serve to emulate the Sommerfeld radiation condition[9] and to ensure that the waves radiated by the antenna are not reflected back to it from the edges of the computational domain. In a driven problem like ours, some numerical back-reflections from the PMLs can and do occur, but cause little to no problem. The metallic layers are implemented as "Layered Impedance Boundary Conditions", which are essentially a generalization to an arbitrary number of layers of the formalism laid out in [112]. The ports of the structure are its left and right coupling points, or simply "ends." Technically, we could define the windows as open ports, but their frequency response is difficult to measure experimentally and consider the light radiating through them as loss in the system. In other words, $|\det \mathbf{S}| < 1$. Solving the system boils down to the definition of the input field on the ports and letting the solver solve Maxwell's equations in the computational domain. The S-parameters correspond to the fraction of the power that either (i) returned back into the source port or (ii) traveled all the way to the other port. This is done for both ports in turn. The far-field associated with each run is computed via the near- to far-field transformation that is discussed in Example 3.2, using the environment's boundary as the last scattering surface.

The traces of the S-parameters, i.e. the value of S_{ij} as a function of the frequency of the input fields, will be of primary interest. The frequency response can give information about the quality factor of the resonances, as well as hinting at specific radiation mechanisms. The analysis below will be divided in two parts: the analysis of the traces on their own, and comparison with the theoretical/simulation traces. Notice that our device is reciprocal, such that $S_{12} = S_{21}$. We only have three independent scattering parameters to study.

3.2.2.1 Analysis of Experimental Traces[10]

Before showing the correspondence (or lack thereof) between the simulated and measured traces, we will analyze the traces by themselves and try to extract any information we can. The main tool we will use to do so is the autocorrelation of the traces. It is defined as

$$c_{XX}(\Delta t) = \frac{\langle [X(t+\Delta t) - \langle X(t)\rangle][X(t) - \langle X(t)\rangle]\rangle}{\langle X(t)^2\rangle - \langle X(t)\rangle} \tag{3.39}$$

[9] This type of absorbing boundary conditions has been used for decades and has lead to a number of problems, which in turn led to a rich literature. It was shown that naïvely using PMLs led to spurious solutions [117–119]. They are usually removed by adding the null term $(\nabla \cdot \boldsymbol{H}^*)(\nabla \cdot \boldsymbol{H})$ in the functional that is minimized. In the microcavities field, specifically in the finding of resonances, it was found out that the PMLs caused large errors in the determination of the imaginary part of the resonant k [120–122] The problem was recently solved for microcavities having azimuthal symmetry [123, 124].

[10] All experimental measurements were obtained by our local experimental group at Centre d'Optique Photonique et Laser at Université Laval, by either Stephan Gorgutsa or Victor Bélanger-Garnier.

for a time series $X(t)$. Since the autocorrelation of a signal has the same periodicity as the input signal, it is a practical way to reduce the noise of experimental data and detect periodicity.

Another interesting property that can be used to theoretically characterize the type of scattering occurring in our structures is the decay of the autocorrelation function. In the 1980s, it was shown that if the underlying classical mechanics of the structure showed chaoticity, the corresponding open quantum scattering problem retained the signature of chaos through the Lorentzian decay of the autocorrelation of the scattering matrix elements [125, 126]. We will thus use a Lorentzian fit of the form

$$L(x;\boldsymbol{p}) = p_0 \frac{p_1/2}{x^2 - p_1^2/4} \tag{3.40}$$

where $\boldsymbol{p}$ is a vector of parameters to be fitted. The quality of the fit will serve as a qualitative way to determine the quality of the fibre-antenna. A good Lorentzian fit indicates irregularity of the spectral response and consequently of the bad quality of this particular fibre-antenna realization. The reasoning is that the resonances (or dips in the traces, rather) are the result of the commensuration between the geometry and the wavelength of the light and are thus expected to repeat periodically.

(a) RF10 This is the first realization of the fibre-antenna and, consequently, its S-parameters are far from the desired ones (see Figure 3.7), as they show a single dip at $f \sim 800\,\text{MHz}$. The rapid decrease of the autocorrelation reflects on the poor fabrication process. In other words, the lengths of the window are so different that the wave essentially undergoes random motion.

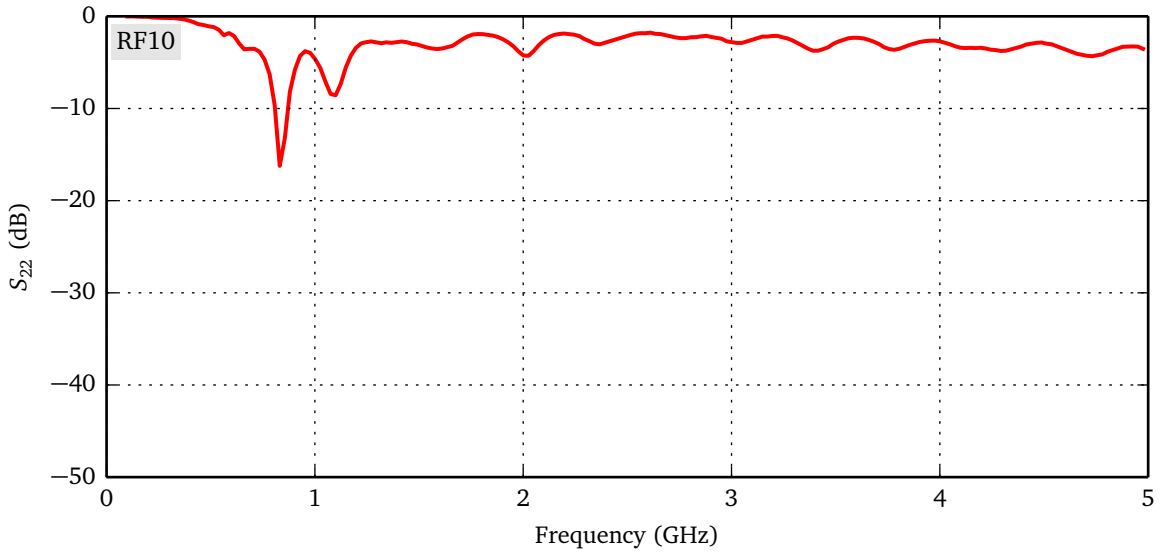

Figure 3.7 – Experimental S_{22} trace for the RF10 fibre-antenna. The relatively small background value of $\sim -4\,\text{dB}$ indicates that much of the power is reflected back from port 2 (the right-hand side of the antenna, according to our specifications). Also, its single dip at $f \sim 800\,\text{MHz}$ is mostly useless for our purposes.

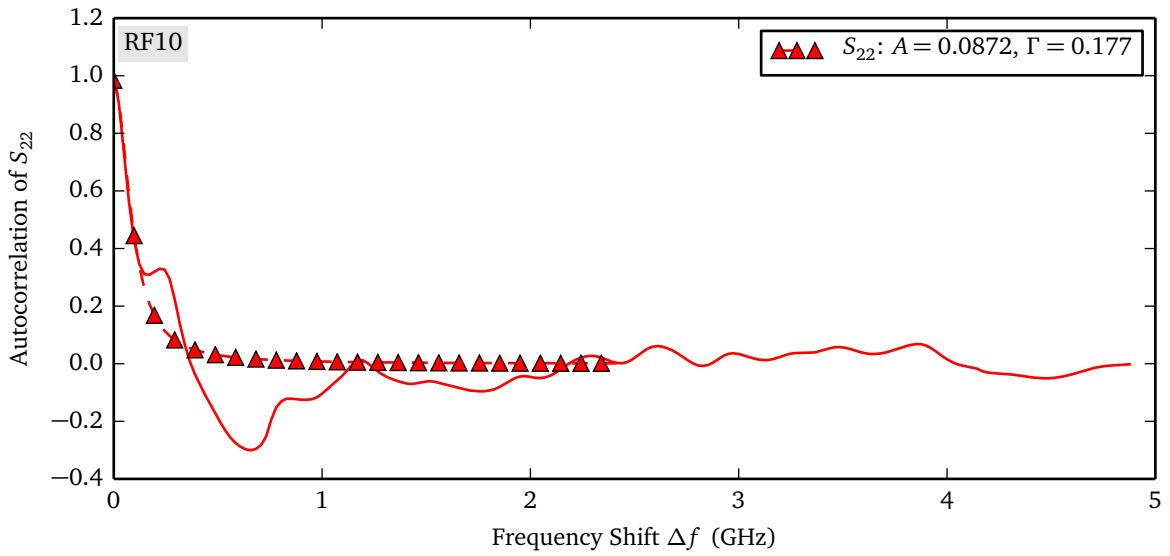

Figure 3.8 – Autocorrelation of the experimental trace of S_{22} for the RF10 fibre-antenna. The dotted line represents the Lorentzian fit. Despite relatively strong negative correlation around 800 MHz, it is almost zero over the whole interval, but does not fit the Lorentzian.

(b) RF21 The traces of this particular realization shows definite dips, particularly in the transmission coefficient S_{12}, with associated although weaker dips in both reflection coefficients. The two dips, occurring at $f \sim 1.8\,\text{GHz}$ and $f \sim 3.0\,\text{GHz}$, correspond to optical wavelengths $\lambda_{\text{opt}} = c/(nf)$ of approximately 8.5 cm and 5.3 cm, respectively. They correspond to the lengths of the first and last scattering cells, approximately; the existence of these two dips thus seems predicated on the asymmetry of the cells ($d_L \neq d_R$). The fact that all traces show dips at these frequencies implies that energy is lost in the system. Neglecting the losses to the metallic layers (they are thinner than the skin depth, minimizing the losses), we can assume that the lost energy is radiated away through the windows. This design thus has two operating frequencies, both outside the desired range, however.

(c) RF27 and RF29 As we can see from Table 3.1(a), these two antennae are rather similar. It is thus not surprising that their S-parameters show similar behaviour (compare Figures 3.11 and 3.13). Their small differences can be explained away by the experimental variability of both the metal deposition and window sizing protocols, as they have identical specifications.

Notice the quick decay of the autocorrelation function of the reflection coefficients, S_{11} and S_{22}. If it were not for the hint of regularity present in the autocorrelation function of S_{12}, it could be swiftly concluded that both antennae show chaotic scattering. In any case, the lack of periodicity in the signals seems to indicate that the dip is not due to the geometry of the fibre-antenna.

(d) RF33 The RF33 fibre-antenna, the final antenna produced, is the most mature one in terms of experimental protocol and is therefore most worthy of study. Notice that the baseline for this

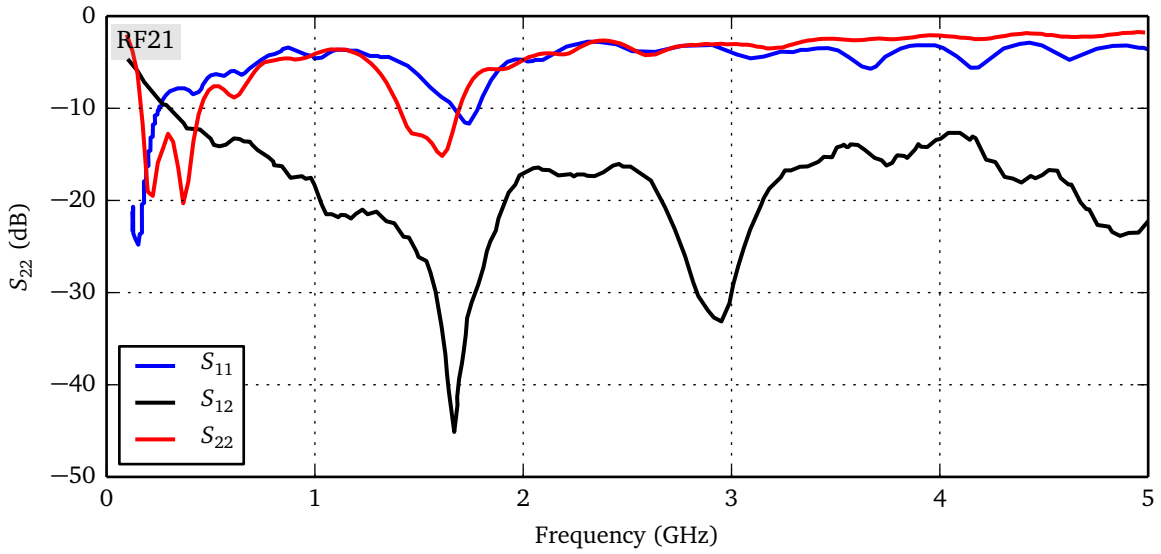

Figure 3.9 – Experimental S_{22} trace for the RF21 fibre.

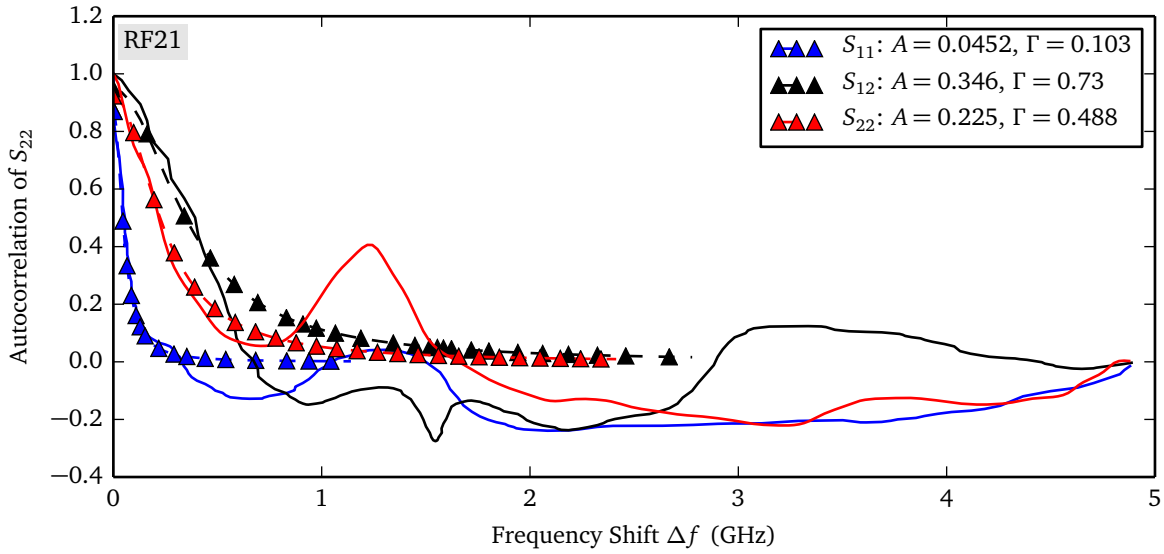

Figure 3.10 – Autocorrelation of the experimental S_{22} trace for the RF21 fibre-antenna.

fibre is higher than that of the other fibres. The dips also show lower quality, although it is possible to make the LCX operate as an antenna at some of the frequency dips. Specifically, there is a dip at $f \sim 2.6\,\text{GHz}$, which is close to our requirements. There is however, an increase in the reflection coefficients at this frequency, hinting that the antenna might not be efficient at that frequency. There seems to be a repetition of the trace at every 2 GHz.

The autocorrelation of the trace of S_{22} shows a strong periodic component, which we have isolated by taking the FFT of the signal. Figure 3.17 shows the intensity of the FFT transform. To see if the periodic components corresponded to particular lengths in the system, we converted the

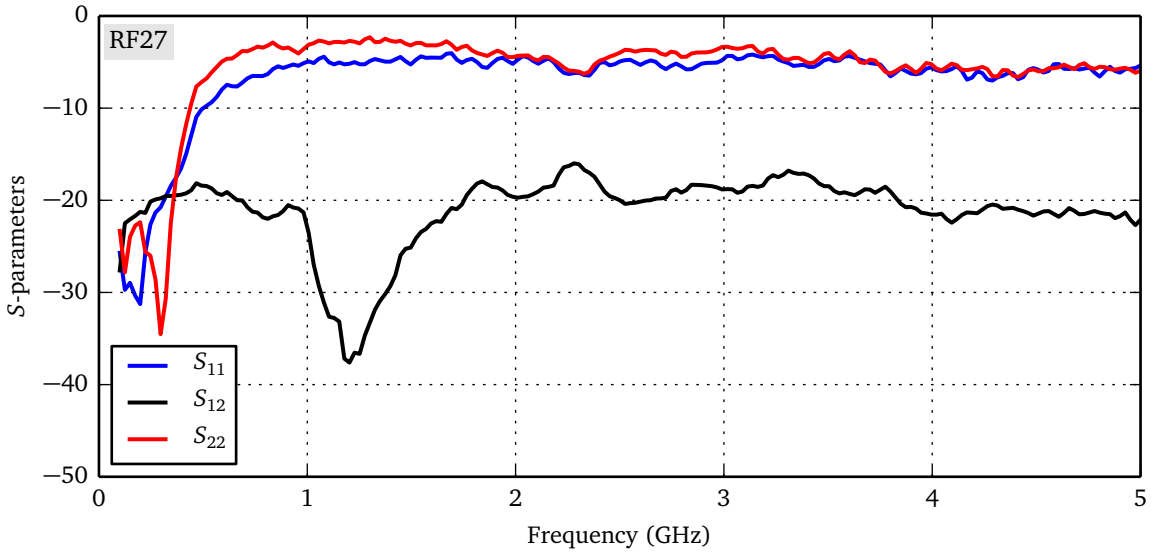

Figure 3.11 – Experimental S-parameter traces for the RF27 fibre-antenna.

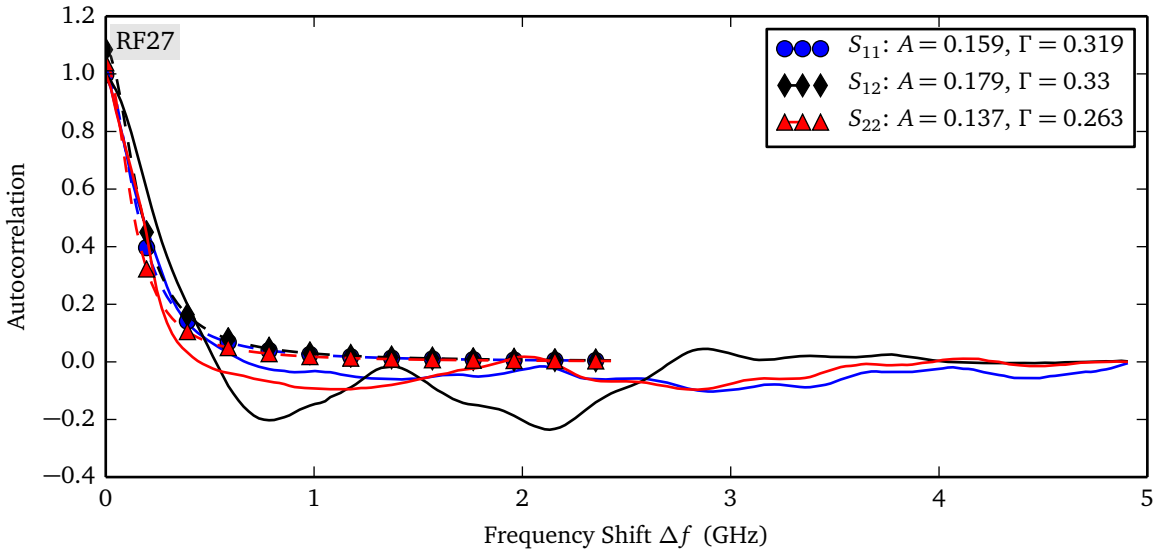

Figure 3.12 – Autocorrelation of the experimental S-parameter traces for the RF27 fibre-antenna.

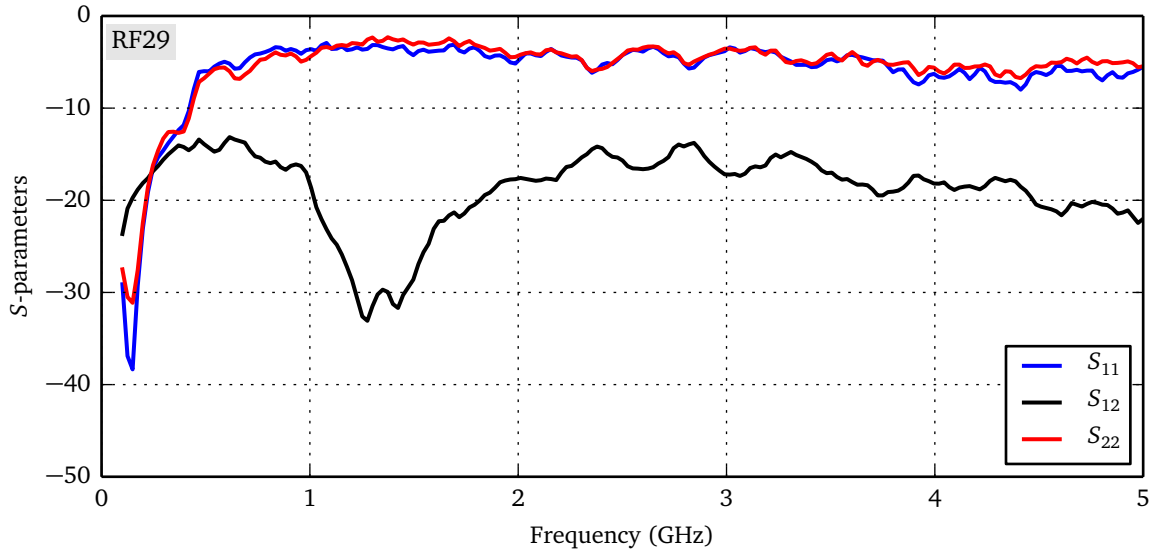

Figure 3.13 – Experimental S-parameter traces for the RF29 fibre-antenna.

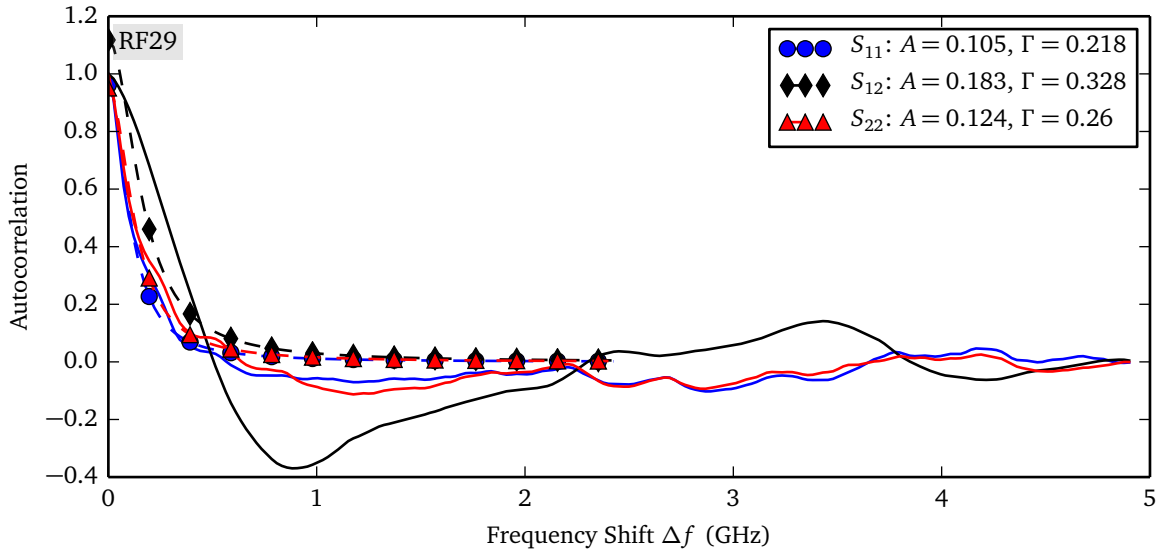

Figure 3.14 – Autocorrelation of the experimental S-parameter traces for the RF29 fibre-antenna.

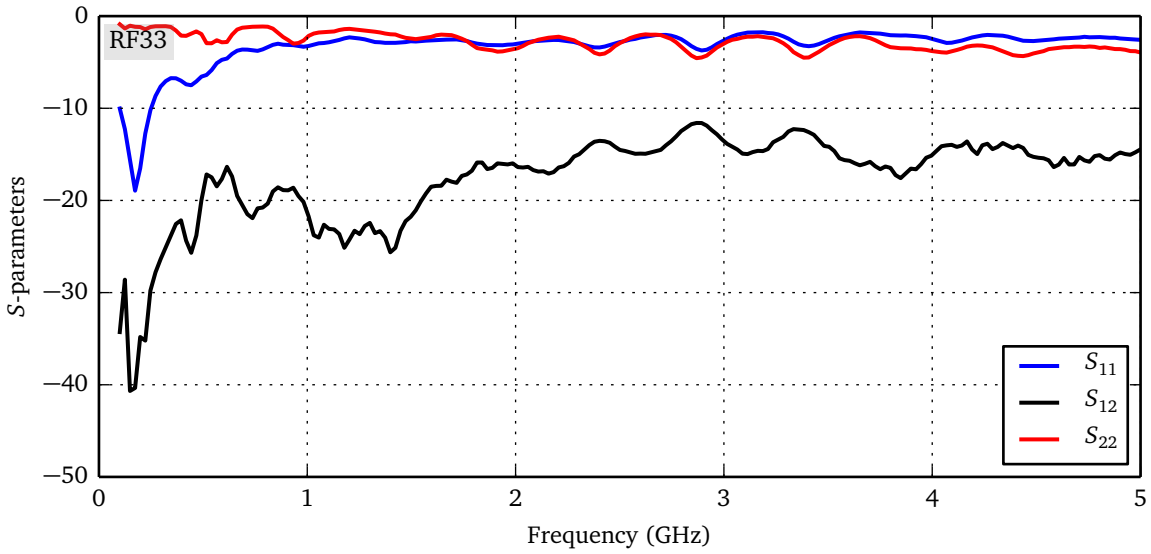

Figure 3.15 – Experimental S-parameter traces for the RF33 fibre-antenna.

associated wavelengths to frequencies. The fundamental mode of infinite LCX [106] is

$$f_1 = \frac{c}{(S_z + d_z)\left(\sqrt{\epsilon_{\text{Si}}} + 1\right)} \sim 1.6\,\text{GHz}. \tag{3.41}$$

The frequency associated with the optical and the actual lengths of the window are

$$l_{\text{opt}} = \frac{c}{S_z\sqrt{\epsilon_{\text{Si}}}} \sim 4.5\,\text{GHz}$$
$$l_{\text{phy}} = \frac{c}{S_z} \sim 8\,\text{GHz}.$$

Nothing thus far seems to explain the periodic properties of the experimental S_{22} trace, although it might just be that f_1 depends on the sizes d_L and d_R and what we see is the fundamental mode of our quasi-LCX.

3.2.2.2 Comparison with Simulation Results

The specifications of each RFXX was based on the numerical simulation of the antennae. However, once they were built, it became clear the numerical modeling did not correlate well with the experimental realizations. As we will see, the experimental traces rarely possess the same features as the numerical ones and the far-field patterns do not match.

The main cause for such poor agreement between theory and experiment was hypothesized to be related to the metallic layers. As discussed above, the experimental method the group used did not allow for any control over the thickness of metal deposited, and did not guarantee its mechanical properties nor its chemical ones. In other words, the layers could be grainy and contain impurities. The former was taken into account directly in the HFSS software, as the

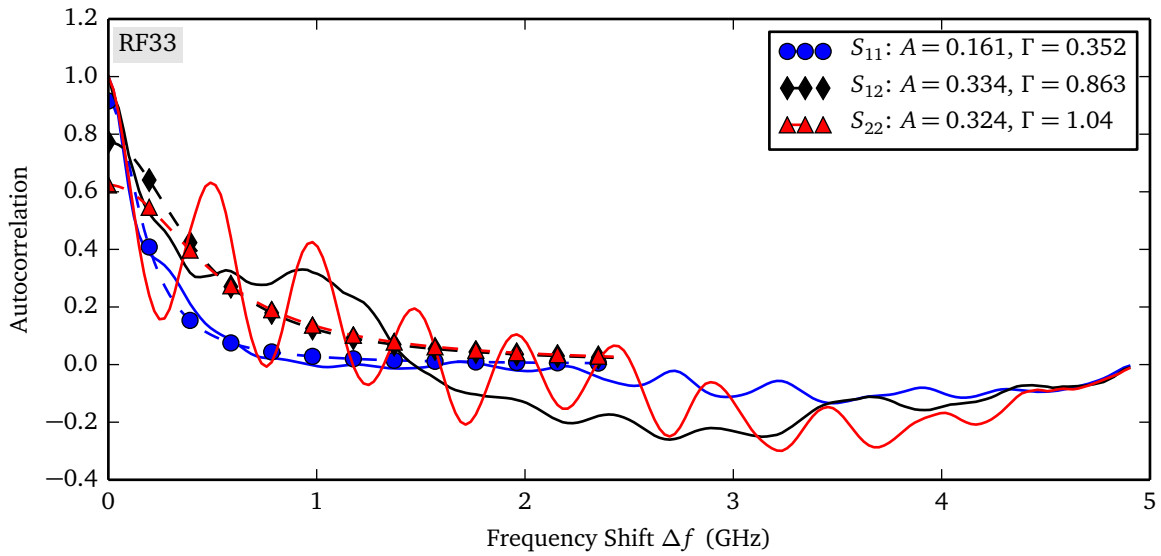

Figure 3.16 – Autocorrelation of the experimental S-parameter traces for the RF33 fibre-antenna.

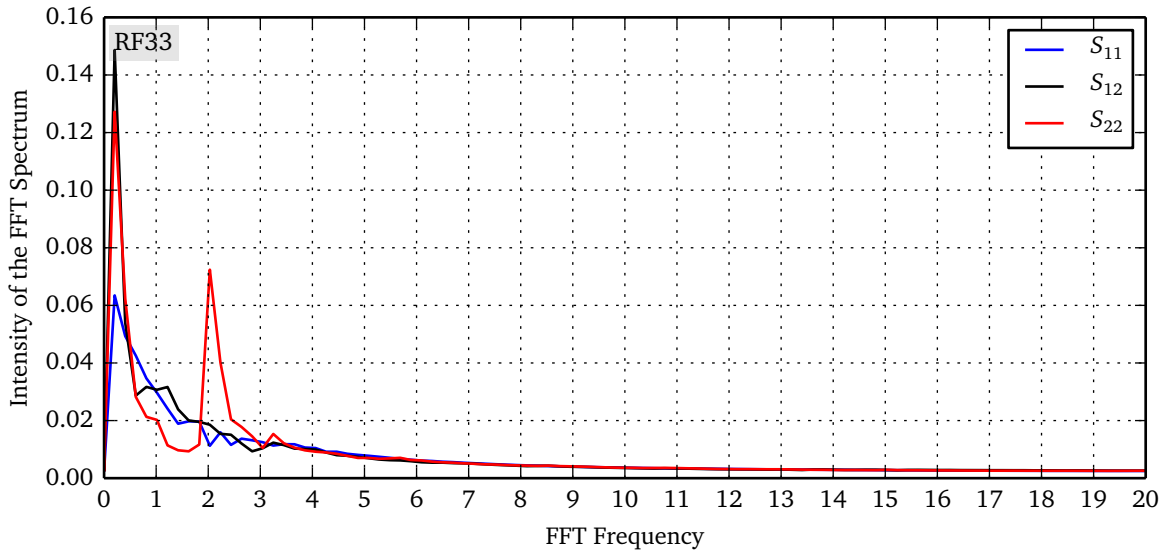

Figure 3.17 – FFT spectrum of the autocorrelation functions of the S-parameters of the RF33 fibre-antenna.

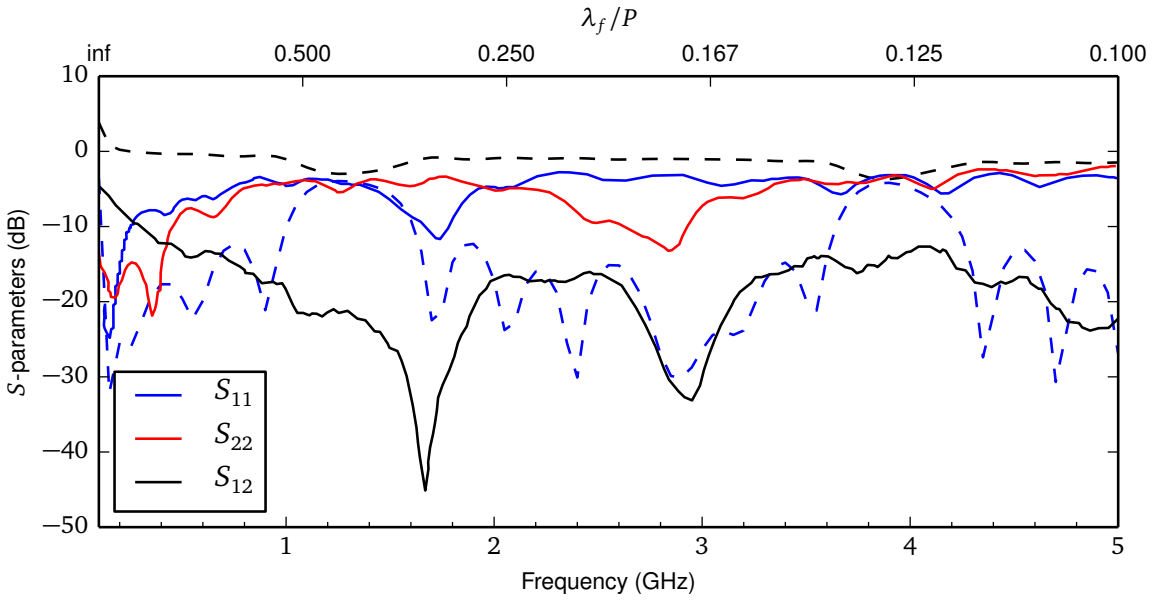

Figure 3.18 – S-parameters of the RF21 fibre design. The full lines represent the experimental data while the dotted lines represent the simulation data. The top x axis shows the S-parameters as a function of the ratio of the vacuum wavelength λ_f over the period of the windows P.

"Layered Impedance Boundary Conditions" module allows for inhomogeneities in the surfaces. The author of this essay thus tried to model the effects of impurities on the conductivity and the effect of the resulting small thicknesses of the layers. The next section details the modeling efforts.

(a) Preliminary Results Because of its easily interpretable traces and of its (at the time) quality, the RF21 fibre is the one we analyze. Figure 3.18 shows both the experimental traces and the numerically predicted ones. Note that this simulation did not contain any effective boundary conditions, but assumed that the silver layers had a constant $2\,\mu$m thickness. We can see transmission-line behaviour in the S_{12} parameter, as the wave is transmitted without much loss regardless of frequency. Clearly, this model does not represent reality well. Removing the silver layers and replacing them by effective boundary conditions does not solve the problem, as is shown in Figure 3.21.

(b) Modeling the Effect ot Thin Metallic Layers AFM pictures (see Figure 3.19) have suggested that the deposited metal is in fact a mixture of silver and silver oxide. To evaluate the effective conductivity of the mixture, we have used Bruggeman's model [127]. The model starts from a homogeneous medium, call it medium 1, of conductivity σ_1 and replaces spherical portions of this material by another one of conductivity σ_2. When this process is done, we are left with a inhomogeneous material with partial concentrations δ_i of each material. The effective conductivity

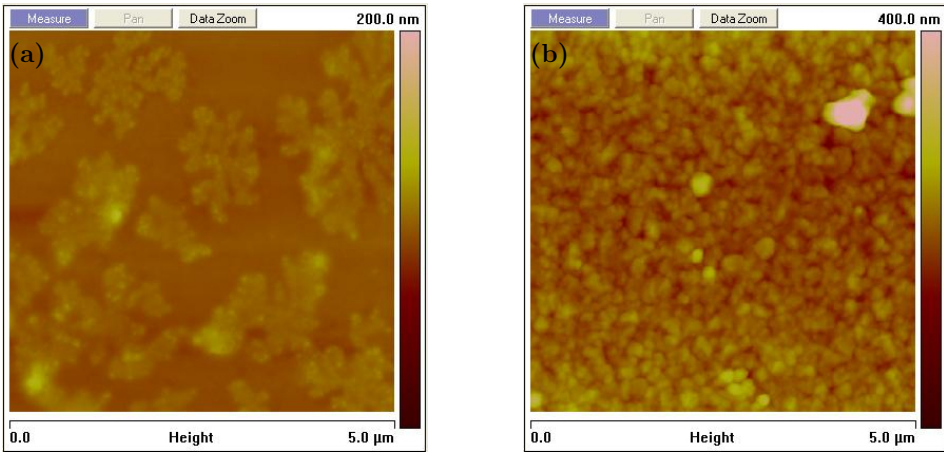

Figure 3.19 – AFM pictures of silver deposited onto glass plates. **(a)** Flakes of silver oxide seem to be forming onto the deposited silver layer. **(b)** Sample image showing the inhomogeneity of the silver layer.

σ_e of the medium can be computed using the relation (for an arbitrary number of materials)

$$\sum_i^n \delta_i \frac{\sigma_i - \sigma_e}{\sigma_i + (d-1)\sigma_e} = 0 \tag{3.42}$$

where $\sum_i \delta_i = 1$ and d is the dimensionality of the system. Solving for σ_e in the case $n = 2$ yields

$$(d-1)\sigma_e^2 + [(d\delta_1 - 1)\sigma_1 + (d\delta_2 - 1)\sigma_2] + \sigma_1\sigma_2 = 0. \tag{3.43}$$

The positive solution is, defining $q = (d\delta_1 - 1)\sigma_1 + (d\delta_2 - 1)\sigma_2$

$$\sigma_e = \frac{1}{2d-2}\left[q + \sqrt{q^2 + 4(d-1)\sigma_1\sigma_2}\right]. \tag{3.44}$$

Using this effective conductivity in (3.38) yields the associated thicknesses. We use $d = 3$ throughout.

It also came to light that the conductivity of thin metal films can be a function of their thicknesses. The state-of-the-art model to describe this dependence is the *Fuchs-Sondheimer* model, which essentially computes the electron distribution in the metal as a function of its thickness. From Ohm's law, it is then trivial to obtain the value of the conductivity [128–130]. The general relationship is

$$\frac{\sigma_F}{\sigma_0} = 1 - \frac{3(1-p)}{8\kappa} + \frac{3}{4\kappa}(1-p)^2 \sum_{\nu=1}^{\infty} p^{\nu-1} \left\{ \int_{\kappa\nu}^{\infty} \frac{e^{-\xi}}{\xi} d\xi \left(\kappa^2\nu^2 - \frac{\kappa^4\nu^4}{12} \right) + e^{-\kappa\nu} \left(\frac{1}{2} - \frac{5\kappa\nu}{6} - \frac{\kappa^2\nu^2}{12} + \frac{\kappa^3\nu^3}{12} \right) \right\} \tag{3.45}$$

where $\kappa = t/\lambda_0$ where λ_0 is the mean free path of the electrons in the metal and t the thickness of the sample. The parameter p is the proportion of electrons that are reflected elastically at the

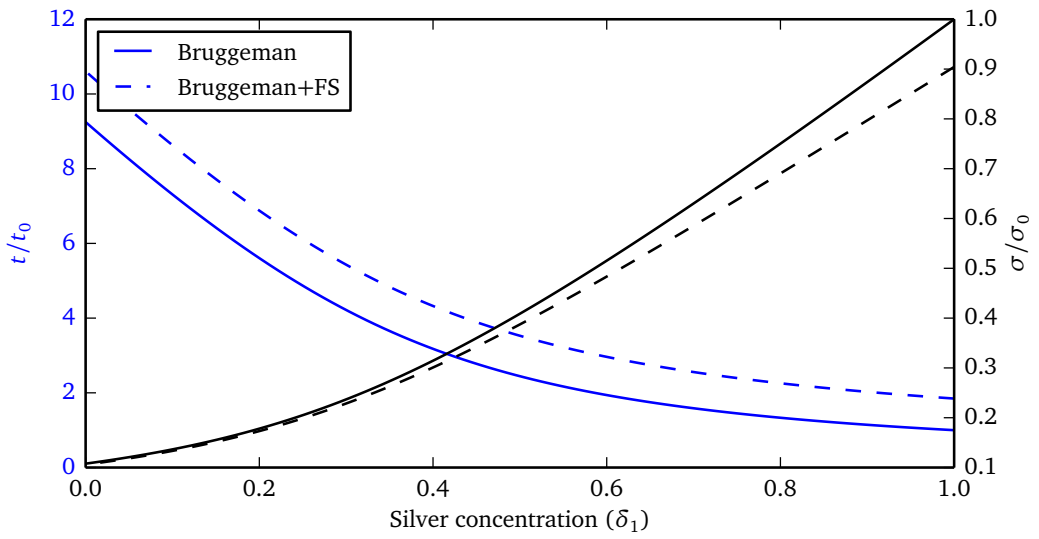

Figure 3.20 – Conductivities and thicknesses predicted by the Bruggeman and Fuchs-Sondheimer models as a function of the silver concentration, δ_1. Conductivity increases as δ_1 increases and the thickness correspondingly decreases.

boundary. For rough edges, we expect the electrons to be scattered off randomly and thus $p \sim 0$. Notice that the above expression is extremely unwieldy and yields to a highly non-linear root search when substituted in (3.38). We will use the much more convenient form (valid for $\kappa \ll 1$) [128]

$$\sigma_F = \frac{\sigma_0}{1 + \frac{3\lambda}{8t}(1-p)} \tag{3.46}$$

which leads to a simpler cubic equation for the thickness. This model states that conductivity diminishes as the thickness of the metallic layer gets smaller, as one would expect.

In Figure 3.20, we show the changes in the predicted conductivities and thicknesses of the silvers layers if we take the Bruggeman and Fuchs-Sondheimer models into account. Given that the AFM pictures show surface inhomogeneity, we assume diffuse scattering in the FS model ($p = 0$). Both the changes in effective conductivities and thicknesses cover an order of magnitude, which should lead to changes in the S-parameters.

We have simulated the RF21 fibre using Bruggeman's model for the effective conductivity and with values of $\delta_1 \in \{0, 1\}$ and $d = 3$ in (3.44). After obtaining the simulated S_{11} parameter of the fibre, we compared it to the experimentally obtained one using the Pearson correlation coefficient. For two samples $\{X_i\}$ and $\{Y_i\}$, it is defined as

$$r = \frac{\sum_i^n (X_i - \langle X \rangle)(Y_i - \langle Y \rangle)}{\sqrt{\sum_i^n (X_i - \langle X \rangle)^2}\sqrt{\sum_i^n (Y_i - \langle Y \rangle)^2}}. \tag{3.47}$$

From the definition, we see that the simultaneous linear transformations $X_i \to b + aX_i$ and $Y_i \to d + cY_1$ do not change the value of the Pearson coefficient. This means that even if the two samples

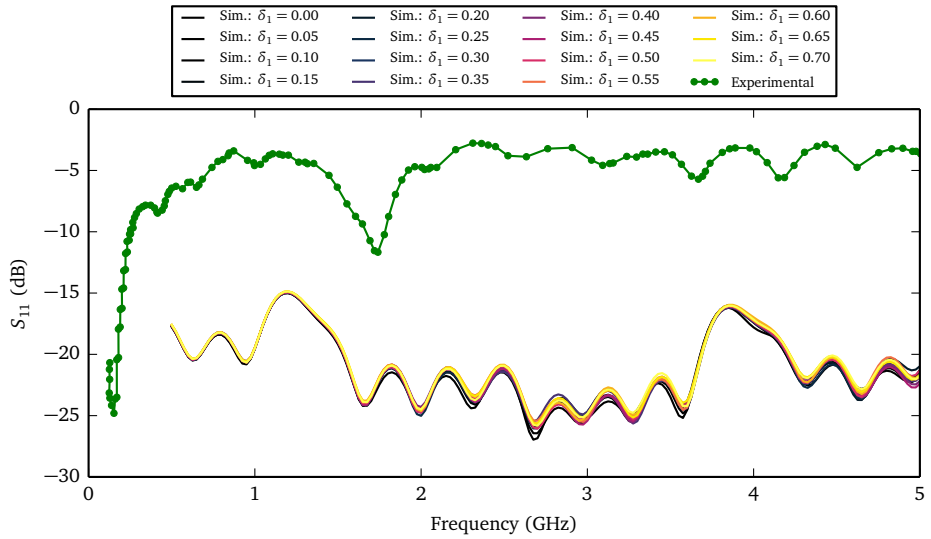

Figure 3.21 – Experimental and simulated S_{11} parameter for the RF21 fibre.

do not have the same normalization or are shifted by a constant amount, the correlation will stay the same. As such, the Pearson correlation measures the degree at which both samples are linearly related.

Figure 3.18 shows the experimental and simulated S_{11} parameter. At first look, it might seem like the general form of the curves are similar, but our quantitative analysis shows that that would be wrong. To make sure that our simulation data was not simply shifted in frequency due to a small error in the geometry, we have also calculated the correlation for a shifted dataset [11]. This changes the Pearson correlation because we must elide some of the experimental and simulation data to do so. Figure 3.22 shows our results. We see that there are little to no correlation between the simulation data and the experimental data with $r \in \{-0.04, 0.05\}$, and this is true for all silver concentrations. Although it is not shown, were also performed with the Fuchs-Sondheimer model: the S-parameters did not vary appreciably from those shown here.

We unfortunately conclude this section by noting that the above phenomena are not sufficient to explain the lack of correlation between the experimental and simulation datasets. The models do predict dramatically different properties for the metallic layers, but it seems that this does not affect the S-parameters all that much. One explanation is that the effect of the surface inhomogeneities are *not* taken into account when computing the thicknesses; they are only accounted for *a posteriori* in the FEM software. By using an *ab initio* model to compute the effects of randomly distributed inhomogeneities on the base conductivity σ_0 of the metallic layers [131], one could obtain a better estimate of the thicknesses and possibly a better fit between the experimental and simulated datasets.

[11] To do so, we simply right-shifted the arrays containing the simulation data and removed the data that fell outside the frequency range of the experimental data.

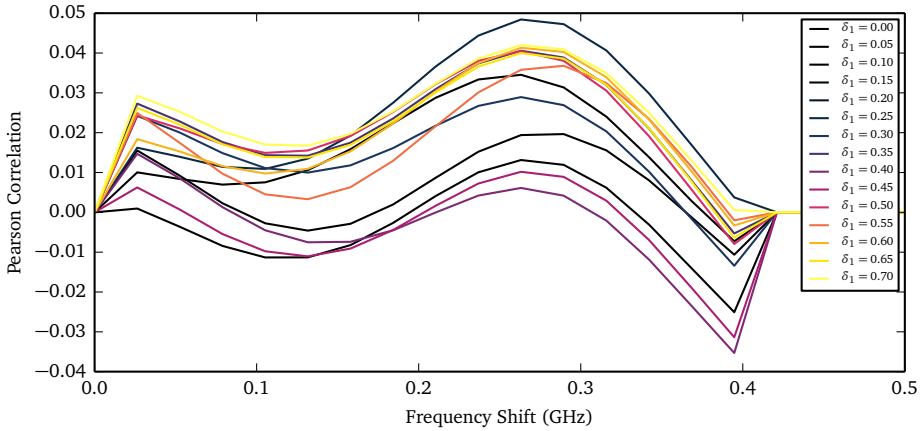

Figure 3.22 – Pearson correlation coefficient as a function of the frequency shift of the data.

We can see, however, that while of the details of the S-parameters are not well reproduced, some dips appear both in experimental and simulated traces. The irregular scattering, due to the experimental variations of the geometry, could account for the suppression of some dips and the possible shifts. However, it is difficult to predict *a priori* which ones will be suppressed and which ones will be shifted, as we do not have “robustness” information.

Chapter 4

Conclusion

Qui va ça et là finit par arriver.

Wisdom of a Fortune Cookie

4.1 Summary

We have presented some results about the modelization of bidimensional resonators, both passive and active, and have designed a leaky coax antenna for smart textile applications.

Throughout this essay, we have made use of the **S**-matrix formalism to compute the resonances of the devices under study. For passive (and lossless) cavities, the formalism was augmented by the introduction of the time-delay matrix, or **Q**-matrix, which is related to the overlap of the normal modes of the resonator. The eigenvalues of this matrix turned out to be related to the poles of the **S**-matrix and be composed of a sum of Lorentzian curves. The eigenvalues were in fact the time-delays associated with the interaction of the incoming light field with the scatterer. The eigenvectors of the **Q**-matrix describe a set of modes that exist for every continuous value of k. The set of modes has the property of interacting in a *self-replicating* manner with the cavity. While the interaction does not disturb the angular momentum distribution, it incurs a phase shift on the incoming field, and the energy derivative of this shift is the time-delay suffered by the mode. It can be directly related to the Q-factor of the mode. The introduction of the **Q**-matrix transforms the search for the poles of the **S**-matrix in the complex plane in a search for the maxima of the time-delay spectrum on the real k-line.

The properties of the **Q**-matrix, and its simple interpretation, mostly depend on the unitarity of the **S**-matrix. When the potential is complex, this is no longer true. It is however still possible to define a Hermitian **Q**-matrix with the sought-after properties, but it requires the evaluation of the **Q**-matrix along a curve in the complex k-plane. This makes the interpretation of the spectrum of

Q as a time-delay more difficult, and most importantly makes their relationship with the poles of the **S**-matrix clouded. It also nullifies the computational advantages of working with $k \in \mathbb{R}$. The author thus concluded that for active (or lossy) cavities, it is best to stick with the **S**-matrix alone.

This seemed a perfect segue into the study of active cavities, where the SALT is used to model the effect of a quantum gain medium as an additional term in the refractive index[1]. The latter is dispersive and complex, possibly non-linear. This motivated the development of a more stable numerical method. We used a Lippmann-Schwinger approach. The method is calibrated using the homogeneous circular cavity laser and we discuss the pole structure of the scattering matrix.

We then turned our attention to the design of a LCX antenna. The complex geometry of the antenna and the perplexing features of the metallic layers made for a complicated modeling task. Some attempts were made at explaining the major discrepancies between the experimental and simulation datasets. We quantified the effects of mixing different materials and of thin films using the Bruggeman and Fuchs-Sondheimer models, respectively. Using FEM software to incorporate these models, as well as taking into account possible surface inhomogeneities via a dedicated module in the software, the author concluded that an *ab initio* model of the effect of the surface inhomogeneities was needed in order to properly assess the thicknesses of the silver layers.

This last paragraph should convince the reader that data alone is not sufficient to explain everything. The first section showed that theory can give both qualitative and quantitative insight into the systems under study. Data is of course necessary to confirm or infirm theory, but, for intellectual and practical reasons, cannot stand alone. The intellectual exercise of probing the working of the universe, in itself, better the state of our knowledge. The resulting theories provide guidelines for future research and new experiments[2] and ease the interpretation of the data. On the more practical side, the guidelines can dramatically reduce the cost of the design phase of any kind of device.

4.2 Perspectives

While most of this essay limited its scope to bidimensional cavities, many of the tools can be directly generalized to three dimensions. Much work was done by the author to find methods that would work reasonably well in 3D, but it was never seen to completion. The last appendix of this essay presents some of the basic tools for 3D scattering. They are published here in the hope that they may be useful in the future.

One of the main approximations generally used in the study of microcavities in the assumption that the fields exist in infinitely long cylinders. This works reasonably well, but is not enough for accurate comparison with experiments. One interesting project would be to use a full 3D numerical method and investigate the 2D limit of electromagnetism in microcavities, if it is well-

[1] This is valid for the TM mode only.
[2] Guidelines that must sometimes be broken, of course [132].

defined. This could in turn be used to properly model polarization effects, which could perhaps be put to use as an extra degree of freedom in biodetection devices.

4.3 Technical Acknowledgements

This work would not have been possible without [133], a C++ linear algebra library. We also wish to thank [134] for the color-blind compliant color maps.

Appendix A

Bessel Functions

This appendix contains some results concerning the Bessel functions. Given our redution of Maxwell's equations from 3D to 2D using cylindrical coordinates, the Bessel functions will form the basis of our analysis, as they are the eigenfunctions of Helmholtz's equation in those coordinates.

We thus wish to collect some of their most important properties here for easy reference. Most of them come from the celebrated volume by Abromowitz & Stegun [135], while a few come from [136]. Proper reference will be given when needed.

In what follows, $\nu, z \in \mathbb{C}$ and $n \in \mathbb{N}$ unless explicitly stated otherwise.

A.1 Definition and Elementary Properties

A.1.1 Differential Equation

The Bessel functions solve the differential equation

$$z^2 \frac{d^2 w}{dz^2} + z \frac{dw}{dz} + (z^2 - \nu^2) w = 0 \tag{A.1}$$

which is a special case of the confluent hypergeometric differential equation, which is in turn a special case of the hypergeometric differential equation. When solved via Fröbenius' method, it yields the solution

$$J_\nu(z) = \sum_{k=0}^{\infty} \frac{(-1)^k \left(\frac{1}{2} z\right)^{\nu+2k}}{k! \Gamma(\nu + k + 1)}. \tag{A.2}$$

This is the Bessel function of the first kind. A second, linearly independent is defined by

$$Y_\nu(z) = \frac{J_\nu(z) \cos \pi\nu - J_{-\nu}(z)}{\sin \pi\nu} \tag{A.3}$$

where a valid limiting process must be used when $\nu \to n$.

We will be mostly interested in a second set of linearly independant solutions: the Hankel functions. They are defined by

$$H_\nu^{(+)}(z) = J_\nu(z) + iY_\nu(z) \tag{A.4a}$$
$$H_\nu^{(-)}(z) = J_\nu(z) - iY_\nu(z). \tag{A.4b}$$

We will alternatively use the notation

$$H_\nu^{(\omega)} = J_\nu(z) + i\omega Y_\nu(z) \qquad (\omega = \pm) \tag{A.5}$$

to denote both functions at the same time.

A.1.2 Recurrence Relations

From the differential equation itself, we can derive multiple recurrence relations that the whole family of Bessel functions obey. If $\mathscr{C}$ denotes J, Y, $H^{(\pm)}$ or any linear combination of the four functions, we have

$$\mathscr{C}_{\nu-1}(z) + \mathscr{C}_{\nu+1}(z) = \frac{2\nu}{z}\mathscr{C}_\nu(z) \tag{A.6a}$$
$$\mathscr{C}_{\nu-1}(z) - \mathscr{C}_{\nu+1}(z) = 2\mathscr{C}'_\nu(z) \tag{A.6b}$$
$$\mathscr{C}_{\nu-1}(z) - \frac{\nu}{z}\mathscr{C}_\nu(z) = \mathscr{C}'_\nu(z) \tag{A.6c}$$
$$-\mathscr{C}_{\nu+1}(z) + \frac{\nu}{z}\mathscr{C}_\nu(z) = \mathscr{C}'_\nu(z). \tag{A.6d}$$

However, the minimal solution to these recurrence relations is $J_\nu(z)$, so any attempt at numerically evaluating Y_ν or $H_\nu^{(\pm)}$ using these is foiled (see §C.1 for details).

A.1.3 Relations between Solutions

The following are analytical relationships between the set of Bessel functions. They can be of use in both standard and numerical analysis.

Reflection Formulas [137, p. 286]

$$J_{-\nu}(z) = \cos\nu\pi J_\nu(z) - \sin\nu\pi Y_\nu(z) \tag{A.7a}$$
$$Y_{-\nu}(z) = \sin\nu\pi J_\nu(z) + \cos\nu\pi Y_\nu(z) \tag{A.7b}$$
$$J_{-n}(z) = (-1)^n J_n(z) \tag{A.7c}$$
$$Y_{-n}(z) = (-1)^n Y_n(z) \tag{A.7d}$$
$$H_{-\nu}^{(\omega)} = e^{i\omega\nu\pi} H_\nu^{(\omega)} \tag{A.7e}$$

Complex Conjugate ($\nu \in \mathbb{R}$)

$$\overline{J_\nu(z)} = J_\nu(\overline{z}) \tag{A.8a}$$
$$\overline{Y_\nu(z)} = Y_\nu(\overline{z}) \tag{A.8b}$$
$$\overline{H_\nu^{\omega}(z)} = H_\nu^{(-\omega)}(\overline{z}) \tag{A.8c}$$

The last of these equations is of particular importance in establishing symmetries of the scaattering matrix.

A.2 Asymptotic and Limiting Forms

A.2.1 Expansions for Small Arguments and Fixed ν

From the first few terms of the power series (A.1),

$$J_\nu(z) = \frac{1}{\Gamma(\nu+1)}\left(\frac{z}{2}\right)^\nu \left[1 - \frac{1}{\nu+1}\left(\frac{z}{2}\right)^2\right] + \mathcal{O}(z^{\nu+4}). \tag{A.9}$$

Using the first terms of the ascending series for integer orders n [135, §9.1.11]

$$Y_n(z) = -\frac{1}{\pi}\left(\frac{z}{2}\right)^{-n}\sum_{k=0}^{n-1}\frac{(n-k-1)!}{k!}\left(\frac{z}{2}\right)^{2k} + \frac{2}{\pi}\ln\frac{z}{2}J_n(z) \\ -\frac{1}{\pi}\left(\frac{z}{2}\right)^n\sum_{k=0}^{\infty}\{\psi(k+1)+\psi(n+k+1)\}\left(\frac{z}{2}\right)^{2k}\frac{1}{k!(n+k)!}, \tag{A.10}$$

where

$$\psi(n+1) = -\gamma + \sum_{k=1}^{n} k^{-1} \qquad (\gamma = 0.5772156649\ldots) \tag{A.11}$$

is the digamma function. The cases $n = 0$ and $n \neq 0$ differ

$$Y_0(z) = \frac{2}{\pi}\left(\ln\frac{z}{2} + \gamma\right) + \mathcal{O}(z^2) \tag{A.12}$$
$$Y_n(z) = -\frac{(n-1)!}{\pi}\left(\frac{z}{2}\right)^{-n} + \mathcal{O}(z^{-n+2}). \tag{A.13}$$

The expansions of the Hankel functions are found by using their definition (A.4):

$$H_0^{(\omega)}(z) = 1 + \frac{2i\omega}{\pi}\left(\ln\frac{z}{2} + \gamma\right) + \mathcal{O}(z^2) \tag{A.14}$$
$$H_n^{(\omega)}(z) = -\frac{i\omega(m-1)!}{\pi}\left(\frac{z}{2}\right)^{-n} + \mathcal{O}(z^{-n+2}). \tag{A.15}$$

A.2.2 Expansions for Large Arguments and Fixed ν

The Bessel functions, jealous of the simpler trigonometric functions, try to mimic them when their arguments get large. We have

$$J_\nu(z) \approx \sqrt{\frac{2}{\pi z}} \cos\left(z - \frac{\nu\pi}{2} - \frac{\pi}{4}\right) \tag{A.16a}$$

$$Y_\nu(z) \approx \sqrt{\frac{2}{\pi z}} \sin\left(z - \frac{\nu\pi}{2} - \frac{\pi}{4}\right) \tag{A.16b}$$

$$H_\nu^{(\omega)}(z) \approx \sqrt{\frac{2}{\pi z}} e^{i\omega\left(z - \frac{\nu\pi}{2} - \frac{\pi}{4}\right)} \tag{A.16c}$$

The last of these makes the respect of Sommerfeld's radiation condition a breeze in cylindrical coordinates.

Appendix B

Numerical Methods

In this appendix, we review the details of some of the numerical methods and tools described in the essay. Most of the sections concern the numerical computation of the scattering matrix, as it is our main object of interest.

We wish to solve Helmholtz's equation

$$\left[\nabla^2 + k^2 n_0^2\right]|\psi\rangle = 0 \qquad \boldsymbol{r} \notin \mathscr{C} \tag{B.1a}$$

$$\left[\nabla^2 + k^2 n_c^2\right]|\psi\rangle = V(\boldsymbol{r})\,|\psi\rangle \qquad \boldsymbol{r} \in \mathscr{C} \tag{B.1b}$$

where we write the exterior solution ($\boldsymbol{r} \notin \mathscr{C}$) as $|\psi\rangle = |\psi^{\text{inc}}\rangle + |\psi^{\text{sca}}\rangle$ and the interior solution as $|\psi\rangle = |\psi^{i}\rangle$. The potential operator has the form

$$V(\boldsymbol{r})\{\} = \frac{2}{n}\nabla n \cdot \nabla\{\}$$

in TE polarization, but vanishes in the TM one. Together with the transmission conditions

$$|\psi^{i}\rangle = |\psi^{\text{inc}}\rangle + |\psi^{\text{sca}}\rangle \qquad \boldsymbol{r} \in \partial\mathscr{C} \tag{B.1c}$$

$$\eta_c^2 \frac{d\,|\psi^{i}\rangle}{dn} = \eta_o^2 \frac{d}{dn}\left(|\psi^{\text{inc}}\rangle + |\psi^{\text{sca}}\rangle\right) \qquad \boldsymbol{r} \in \partial\mathscr{C}, \tag{B.1d}$$

where $\eta_i = 1\,(1/n_i)$ in the TM (or TE) polarization, these equations form the general scattering problem for 2D microcavities.

The scattering matrix depends on the various parameters defined above. The environment is considered to be infinite and featureless, i.e. $\mathscr{C}^c = \mathbb{R}^2$ and n_0 is a constant. The cavity region, $\mathscr{C}$, can be any bounded, connected set (or a collection of such sets) and endowed with a refractive index $n_c = n_c(r, \theta)$, which is allowed to be a function of position and frequency. The support of the function $n_o^2 - n_c^2$ coincides with the cavity region $\mathscr{C}$. The scattering operator is defined by the relationship

$$|\psi^{\text{sca}}\rangle = \mathscr{S}\left|\psi^{\text{inc}}\right\rangle \tag{B.2}$$

and relates incoming parts of the field to the outgoing ones *outside* of the last scattering surface, outside of the support of $n_o^2 - n_c^2$.

B.1 Numerical Computation of the Scattering Matrix in SQA

Since it is our primary tool, we will describe the numerical implementation of the SQA in detail. The necessary notation and parameters are defined in Figure 2.5. The discretization contains three distinct regions; an inner circle of radius r_0 (let us call it the first scattering surface, or FSS), the outer circle of radius R_0 (the last scattering surface) and the region in between, which is discretized in onion-like shells. We suppose that refractive index in the FSS is constant and equal to $n_{\text{in}} = n_c(0,0)$. The differential equation inside the FSS reduces to the Bessel equation (A.1). The solution is thus given by (2.41). In the outer region, the solution is given by (2.17).

In the intermediary region, the differential equations to solve depend on the polarizations[1]. For the TM polarization, we must solve the pair of equations found in the main text,

$$\left[\rho_j^2 \frac{d^2}{d\rho_j^2} + \rho_j \frac{d}{d\rho_j} - \xi^j\right] \mathscr{R}^j = 0 \tag{B.3a}$$

$$\left[\frac{d}{d\theta^2} + \left(k^2 n^2(r_j,\theta) r_j^2 + \xi^j\right)\right] \Phi^j = 0 \tag{B.3b}$$

where it is supposed that, inside each shell j, the refractive index does not depend on r, only on θ and where $\rho_j = r/r_j$ is the scaled radius of the shell. For the TE polarization, the pair is

$$\left[\rho_j^2 \frac{d^2}{d\rho_j^2} + \rho_j \frac{d}{d\rho_j} - \xi^j\right] \mathscr{R}^j = 0 \tag{B.3c}$$

$$\left[\frac{d}{d\theta^2} - 2\frac{\partial n}{\partial \theta}\frac{\partial}{\partial \theta} + \left(k^2 n^2(r_j,\theta) r_j^2 + \xi^j\right)\right] \Phi^j = 0. \tag{B.3d}$$

The substitution of the expansion

$$\left\langle \theta \middle| \Phi_\mu^j \right\rangle = \frac{1}{\sqrt{2\pi}} \sum_{m=-\infty}^{\infty} c_{\mu m}^j e^{im\theta} \tag{B.4}$$

in both angular equations yields an eigenvalue problem for the separation constants ξ^j and the expansion coefficients $c_{\mu m}^j$ of the form

$$\mathbf{L}_{\{\text{TE,TM}\}}^j \mathbf{c}_\mu^j = \xi_\mu^j \mathbf{c}_\mu^j \tag{B.5}$$

where

$$\left[\mathbf{L}_{\text{TM}}^j\right]_{mm'} = m^2 \delta_{mm'} - \frac{k^2 r_j^2}{2\pi} \int_0^{2\pi} n^2(r_j,\theta) e^{i(m-m')\theta} d\theta \tag{B.6a}$$

$$\left[\mathbf{L}_{\text{TE}}^j\right]_{mm'} = m^2 \delta_{mm'} + \frac{1}{2\pi} \int_0^{2\pi} \left[\frac{2im}{n(r_j,\theta)} \frac{dn(r_j,\theta)}{d\theta} - k^2 r_j^2 n^2(r_j,\theta)\right] e^{i(m-m')\theta} d\theta. \tag{B.6b}$$

[1] While we used the form (2.14a') to derive the form of the **Q**-matrix, it is actually simpler to solve for $\boldsymbol{H}$ rather $\boldsymbol{h}$, as the boundary conditions are simpler. We will thus use the form (2.14a) for the remainder of this section.

At first glance, $\mathbf{L}^j_{\mathrm{TE}}$ prescribes the evaluation of the angular derivative of the refractive index. However, using

$$\frac{1}{n}\frac{dn}{d\theta} = \frac{d\ln n}{d\theta} \tag{B.7}$$

allows the use of integration by parts. The surface term vanishes as per the periodicity of the refractive index, and we are left with

$$\left[\mathbf{L}^j_{\mathrm{TE}}\right]_{mm'} = \left[\mathbf{L}^j_{\mathrm{TM}}\right]_{mm'} + \frac{m(m-m')}{\pi}\int_0^{2\pi} \ln n(r_j,\theta) e^{i(m-m')\theta} d\theta. \tag{B.8}$$

(a) Normality of $\mathbf{L}^j$ One important property of matrices that physicists often take for granted is *normality*.

Definition B.1 (Normal matrix [77, 138])**.** A matrix $\mathbf{A} \in \mathbb{C}^{n\times n}$ is said to be *normal* if it commutes with its hermitian conjugate

$$[\mathbf{A}, \mathbf{A}^\dagger] = \mathbf{A}\mathbf{A}^\dagger - \mathbf{A}^\dagger\mathbf{A} = 0. \tag{B.9}$$

For these matrices, the following holds:

(i) the eigenvectors form a complete orthonormal set;

(ii) the left and right eigenvectors are related via complex conjugation.

Symmetric and Hermitian matrices are necessarily normal, with the additional property that their spectrum is real.

As can be seem from inspection, $\mathbf{L}^j_{\{\mathrm{TM,TE}\}}$ are normal if, and only if, $n, k \in \mathbb{R}$. The normality depends on the "reflection" symmetry of Fourier series of real data, i.e. that $n_{-j} = n_j^*$. When k possess a non-vanishing imaginary part, some terms in the commutator become anti-Hermitian and of alternating signs and are thus not canceled in the subtraction. The $\mathbf{L}^j_{\mathrm{TM}}$ matrix has the additional property that the value of the elements depend only on their distance from the diagonal:

$$\mathbf{L}^j_{\mathrm{TM}} = \mathbf{M}^2 + k^2 r_j^2 \begin{pmatrix} n_0 & n_{-1} & \cdots & \cdots & n_{-2M} \\ n_1 & n_0 & \cdots & \cdots & n_{-2M-1} \\ n_2 & n_1 & n_0 & \cdots & n_{-2M-2} \\ \vdots & n_2 & n_1 & \ddots & \vdots \\ n_{2M} & \cdots & \cdots & \cdots & n_0 \end{pmatrix} \tag{B.10}$$

which is manifestly Toeplitz.

Because we are interested in computing the scattering matrix for complex n and k and that we need to use orthogonality relations in what follows, we must compute both the left and right eigenvectors. We will note the left (covariant) basis by $\left|\tilde{\Phi}^j_\mu\right\rangle$. This is not sufficient, however, because we are not guaranteed that both sets of eigenvectors will form a *complete* basis.

If the set of eigenvectors does not form a complete basis, the angular ODEs are said to be *defective* and the $\mathbf{L}^j$ matrix is not diagonalizable. The alternative that is usually suggested is the use of Jordan forms, which define an "almost diagonal" matrix J such that

$$\mathbf{A} = \mathbf{P}\mathbf{J}\mathbf{P}^{-1} \tag{B.11}$$

where P is invertible. The $\mathbf{J}$ matrix has the following block structure

$$\mathbf{J} = \begin{pmatrix} J_1 & & \\ & \ddots & \\ & & J_p \end{pmatrix}. \tag{B.12}$$

where p is the number of distinct eigenvalues of $\mathbf{A}$. The eigenvalue problem

$$\mathbf{A}\mathbf{P} = \mathbf{P}\mathbf{J} \tag{B.13}$$

can be used to define a set of generalized eigenvectors. It can be shown that there always exist an eigenbasis consisting only of eigenvectors and of generalized eigenvectors [77]. This can be used to solve the defective angular ODEs.

We do not use Jordan forms numerically, as they are incredibly sensitive on the floating-point representation of the elements of the matrix. We can, however, use SVD to detect whether the basis is incomplete (by looking for vanishing singular values) and computing the generalized eigenvectors that way [137].

We now return to the computation of the scattering matrix. Assuming that we have a complete eigenbasis, we can write the radial solution as

$$\mathscr{R}^j_\mu(r) = a^j_\mu \rho_j^{+\sqrt{\xi^j\mu}} + b^j_\mu \rho_j^{-\sqrt{\xi^j_\mu}}. \tag{B.14}$$

Enforcing the boundary conditions at the interfaces between each shell yields the two sets of equations shown in (2.52). It will be useful to write this in the form

$$\sum_\mu \Big[a^j_\mu F(\rho_{j+}) + b^j_\mu G(\rho_{j+})\Big]\Big|\Phi^j_\mu\Big\rangle = \sum_\mu \Big[b^{j+1}_\mu H(\rho_{j+1-}) + a^{j+1}_\mu K(\rho_{j+1-})\Big]\Big|\Phi^{j+1}_\mu\Big\rangle \tag{B.15a}$$

and

$$\sum_\mu \Big[a^j_\mu F'(\rho_{j+}) + b^j_\mu G'(\rho_{j+})\Big]\Big|\Phi^j_\mu\Big\rangle = \sum_\mu \Big[b^{j+1}_\mu H'(\rho_{j+1-}) + a^{j+1}_\mu K'(\rho_{j+1-})\Big]\Big|\Phi^{j+1}_\mu\Big\rangle \tag{B.15b}$$

where $\rho_{j+} = r_j + \epsilon = r_{j+1} - \epsilon = \rho_{j+1-}$ so that both expressions are evaluated at the interface between the two shells. Now, using the biorthogonality relation between the contravariant $\left|\Phi^j_\mu\right\rangle$ and the covariant bases $\left|\tilde{\Phi}^j_\mu\right\rangle$, i.e.

$$\left\langle \tilde{\Phi}^j_\mu \middle| \Phi^j_{\mu'} \right\rangle = \delta_{\mu\mu'} \tag{B.16}$$

regrouping the a and b coefficients together, we have

$$\sum_{\mu}\Big[a_{\mu}^{j}F(\rho_{j+})\delta_{\mu}^{\mu'}-a_{\mu}^{j+1}K(\rho_{j+1-})U_{\mu\mu'}^{j,j+1}\Big]=\sum_{\mu}\Big[b_{\mu}^{j+1}H(\rho_{j+1-})U_{\mu\mu'}^{j,j+1}-b_{\mu}^{j}G(\rho_{j+})\delta_{\mu}^{\mu'}\Big] \tag{B.17a}$$

and

$$\sum_{\mu}\Big[a_{\mu}^{j}F'(\rho_{j+})\delta_{\mu}^{\mu'}-a_{\mu}^{j+1}K'(\rho_{j+1-})U_{\mu\mu'}^{j,j+1}\Big]=\sum_{\mu}\Big[b_{\mu}^{j+1}H'(\rho_{j+1-})U_{\mu\mu'}^{j,j+1}-b_{\mu}^{j}G'(\rho_{j+})\delta_{\mu}^{\mu'}\Big] \tag{B.17b}$$

where

$$\mathbf{U}^{j,j+1}=\left\langle\tilde{\Phi}_{\mu'}^{j}\middle|\Phi_{\mu}^{j+1}\right\rangle \tag{B.18a}$$

$$\mathbf{V}^{j,j+1}=\left\langle\tilde{\Phi}_{\mu'}^{j}\middle|\frac{n_c^2(r_j,\theta)}{n_c^2(r_{j+1},\theta)}\middle|\Phi_{\mu}^{j+1}\right\rangle \tag{B.18b}$$

Defining diagonal matrices for all radial functions and their derivatives, we can write these equations in matrix form

$$\begin{bmatrix}\mathbf{F} & -\mathbf{U}^{j,j+1}\mathbf{K}\\ \mathbf{F}' & -\mathbf{V}^{j,j+1}\mathbf{K}'\end{bmatrix}\begin{bmatrix}\boldsymbol{a}^{j}\\ \boldsymbol{a}^{j+1}\end{bmatrix}=\begin{bmatrix}-\mathbf{G} & \mathbf{U}^{j,j+1}\mathbf{H}\\ -\mathbf{G}' & \mathbf{V}^{j,j+1}\mathbf{H}'\end{bmatrix}\begin{bmatrix}\boldsymbol{b}^{j}\\ \boldsymbol{b}^{j+1}\end{bmatrix} \tag{B.19}$$

We will now use some results of the excellent book by Meyer [77]. By using Schur's complements, we can invert a block matrix in the following ways

$$\begin{bmatrix}\mathbf{M} & \mathbf{N}\\ \mathbf{O} & \mathbf{P}\end{bmatrix}^{-1}=\begin{bmatrix}\mathbf{M}^{-1}+\mathbf{M}^{-1}\mathbf{N}\mathbf{C}^{-1}\mathbf{O}\mathbf{M}^{-1} & -\mathbf{M}^{-1}\mathbf{N}\mathbf{C}^{-1}\\ -\mathbf{C}^{-1}\mathbf{O}\mathbf{M}^{-1} & \mathbf{C}^{-1}\end{bmatrix} \tag{B.20}$$

$$=\begin{bmatrix}\mathbf{D}^{-1} & -\mathbf{D}^{-1}\mathbf{N}\mathbf{P}^{-1}\\ -\mathbf{P}^{-1}\mathbf{O}\mathbf{D}^{-1} & \mathbf{P}^{-1}+\mathbf{P}^{-1}\mathbf{O}\mathbf{D}^{-1}\mathbf{N}\mathbf{P}^{-1}\end{bmatrix} \tag{B.21}$$

where $\mathbf{M}$, $\mathbf{N}$, $\mathbf{O}$ and $\mathbf{P}$ are matrices and

$$\mathbf{C}=\mathbf{P}-\mathbf{O}\mathbf{M}^{-1}\mathbf{N} \tag{B.22}$$

$$\mathbf{D}=\mathbf{M}-\mathbf{N}\mathbf{P}^{-1}\mathbf{O} \tag{B.23}$$

Inverting (B.19) using the first complement, we obtain

$$\mathbf{S}^{j}=\begin{bmatrix}-\mathbf{G} & \mathbf{U}^{j,j+1}\mathbf{H}\\ -\mathbf{G}' & \mathbf{V}^{j,j+1}\mathbf{H}'\end{bmatrix}^{-1}\begin{bmatrix}\mathbf{F} & -\mathbf{U}^{j,j+1}\mathbf{K}\\ \mathbf{F}' & -\mathbf{V}^{j,j+1}\mathbf{K}'\end{bmatrix} \tag{B.24}$$

$$=\begin{bmatrix}-\mathbf{G}^{-1}-\mathbf{G}^{-1}\mathbf{U}^{j,j+1}\mathbf{H}\mathbf{C}^{-1}\mathbf{G}'\mathbf{G}^{-1} & \mathbf{G}^{-1}\mathbf{U}^{j,j+1}\mathbf{H}\mathbf{C}^{-1}\\ -\mathbf{C}^{-1}\mathbf{G}'\mathbf{G}^{-1} & \mathbf{C}^{-1}\end{bmatrix}\begin{bmatrix}\mathbf{F} & -\mathbf{U}^{j,j+1}\mathbf{K}\\ \mathbf{F}' & -\mathbf{V}^{j,j+1}\mathbf{K}'\end{bmatrix} \tag{B.25}$$

Going through the multiplication gives us the the following block matrices

$$\mathbf{S}_{11}^{j}=-\mathbf{G}^{-1}\mathbf{F}-\mathbf{G}^{-1}\mathbf{U}^{j,j+1}\mathbf{H}\mathbf{C}^{-1}\mathbf{G}'\mathbf{G}^{-1}\mathbf{F}+\mathbf{G}^{-1}\mathbf{U}^{j,j+1}\mathbf{H}\mathbf{C}^{-1}\mathbf{F}' \tag{B.26a}$$

$$\mathbf{S}_{12}^{j}=\mathbf{G}^{-1}\mathbf{U}^{j,j+1}\mathbf{K}+\mathbf{G}^{-1}\mathbf{U}^{j,j+1}\mathbf{H}\mathbf{C}^{-1}\mathbf{G}'\mathbf{G}^{-1}\mathbf{U}^{j,j+1}\mathbf{K}-\mathbf{G}^{-1}\mathbf{U}^{j,j+1}\mathbf{H}\mathbf{C}^{-1}\mathbf{V}^{j,j+1}\mathbf{K}' \tag{B.26b}$$

$$\mathbf{S}_{21}^{j}=-\mathbf{C}^{-1}\mathbf{G}'\mathbf{G}^{-1}\mathbf{F}+\mathbf{C}^{-1}\mathbf{F}' \tag{B.26c}$$

$$\mathbf{S}_{22}^{j}=\mathbf{C}^{-1}\mathbf{G}'\mathbf{G}^{-1}\mathbf{U}^{j,j+1}\mathbf{K}-\mathbf{C}^{-1}\mathbf{V}^{j,j+1}\mathbf{K}' \tag{B.26d}$$

This is all fine and well, but it is instructive to write this in another manner. Notice that the product $\mathbf{U}^{j,j+1}\mathbf{H}\mathbf{C}^{-1}$ appears almost everywhere. Let's write it as

$$\mathbf{U}^{j,j+1}\mathbf{H}\left(\mathbf{V}^{j,j+1}\mathbf{H}' - \mathbf{G}'\mathbf{G}^{-1}\mathbf{U}^{j,j+1}\mathbf{H}\right)^{-1} = \left(\mathbf{V}^{j,j+1}\mathbf{H}'\mathbf{H}^{-1}(\mathbf{U}^{j,j+1})^{-1} - \mathbf{G}'\mathbf{G}^{-1}\right)^{-1} = \mathbf{R}^{-1}. \tag{B.27}$$

We will also define

$$\mathbf{T} = \mathbf{V}^{j,j+1}\mathbf{K}'\mathbf{K}^{-1}(\mathbf{U}^{j,j+1})^{-1} - \mathbf{G}'\mathbf{G}^{-1}. \tag{B.28}$$

Rewriting the block scattering matrices with this, we get

$$\mathbf{S}^j_{11} = \mathbf{G}^{-1}\left[-\mathbf{F} + \mathbf{R}^{-1}\left(-\mathbf{G}'\mathbf{G}^{-1}\mathbf{F} + \mathbf{F}'\right)\right] \tag{B.29a}$$
$$\mathbf{S}^j_{12} = \mathbf{G}^{-1}\left[\mathbf{I} - \mathbf{R}^{-1}\mathbf{T}\right]\mathbf{U}^{j,j+1}\mathbf{K} \tag{B.29b}$$
$$\mathbf{S}^j_{21} = \mathbf{H}^{-1}(\mathbf{U}^{j,j+1})^{-1}\mathbf{R}^{-1}\left[-\mathbf{G}'\mathbf{G}^{-1}\mathbf{F} + \mathbf{F}'\right] \tag{B.29c}$$
$$\mathbf{S}^j_{22} = -\mathbf{H}^{-1}(\mathbf{U}^{j,j+1})^{-1}\mathbf{R}^{-1}\mathbf{T}\mathbf{U}^{j,j+1}\mathbf{K} \tag{B.29d}$$

B.1.1 Specialization to Interfaces

Because the scattering matrices relate the coefficients of neighboring shells, including the inner circle's, we will call the inner circle our "zeroth" shell. With this nomenclature, the exterior of the dielectric can be labelled our $(N+1)$th shell. Hence, the matrix $\mathbf{S}^0$ relates the coefficients of the zeroth shell to that of the first shell.

(a) Zeroth Shell ($j = 0$) The coupling from the inner circle to the first shell has $\boldsymbol{a}^0 = \boldsymbol{b}^0$, hence the factor of 2 in the inner circle solution. This gives the matrices

$$\begin{aligned}
\mathbf{F} &= \mathbf{G} = \mathbf{J} \\
\mathbf{F}' &= \mathbf{G}' = n_{\text{in}} k r \mathbf{J}' \\
\mathbf{H} &= \left(\frac{r}{r_1}\right)^{\mathbf{\Lambda^1}} \\
\mathbf{H}' &= \mathbf{\Lambda^1}\mathbf{H} \\
\mathbf{K} &= \left(\frac{r}{r_1}\right)^{-\mathbf{\Lambda}^1} \\
\mathbf{K}' &= -\mathbf{\Lambda}^1\mathbf{K}
\end{aligned}$$

where $\{\mathbf{J}\}_{mm'} = J_m(n_{\text{in}} k r_0)\delta_{mm'}$ and where the apostrophe means the derivative with respect to the entire argument. Similarly with the other radial functions. The block scattering matrices can

be written as

$$\mathbf{S}_{11}^{0} = -\mathbf{I} \tag{B.30a}$$

$$\mathbf{S}_{12}^{0} = \mathbf{J}^{-1}\left[\mathbf{I} - \mathbf{R}^{-1}\mathbf{T}\right]\mathbf{U}^{0,1}\left(\frac{r_0}{r_1}\right)^{-\mathbf{\Lambda}^1} \tag{B.30b}$$

$$\mathbf{S}_{21}^{0} = \mathbf{0} \tag{B.30c}$$

$$\mathbf{S}_{22}^{0} = -\left(\frac{r_0}{r_1}\right)^{-\mathbf{\Lambda}^1}(\mathbf{U}^{0,1})^{-1}\mathbf{R}^{-1}\mathbf{T}\mathbf{U}^{0,1}\left(\frac{r_0}{r_1}\right)^{-\mathbf{\Lambda}^1} \tag{B.30d}$$

with

$$\mathbf{R} = -\mathbf{V}^{0,1}\mathbf{\Lambda}^1(\mathbf{U}^{0,1})^{-1} - n_{\text{in}}kr_0\mathbf{J}'\mathbf{J}^{-1} \tag{B.31a}$$

$$\mathbf{T} = +\mathbf{V}^{0,1}\mathbf{\Lambda}^1(\mathbf{U}^{0,1})^{-1} - n_{\text{in}}kr_0\mathbf{J}'\mathbf{J}^{-1}. \tag{B.31b}$$

(b) Intermediate Shells $(1 \le j < N)$ We then have

$$\mathbf{R} = \mathbf{V}^{j,j+1}\mathbf{\Lambda}^{j+1}(\mathbf{U}^{j,j+1})^{-1} + \mathbf{\Lambda}^{j} \tag{B.32a}$$

$$\mathbf{T} = -\mathbf{V}^{j,j+1}\mathbf{\Lambda}^{j+1}(\mathbf{U}^{j,j+1})^{-1} + \mathbf{\Lambda}^{j} \tag{B.32b}$$

which gives the block scattering matrices as

$$\mathbf{S}_{11}^{j} = \left(\frac{r_j+\epsilon}{r_j}\right)^{\mathbf{\Lambda}^j}\left[-\mathbf{I} + 2\mathbf{R}^{-1}\mathbf{\Lambda}^j\right]\left(\frac{r_j+\epsilon}{r_j}\right)^{\mathbf{\Lambda}^j} \tag{B.33a}$$

$$\mathbf{S}_{12}^{j} = \left(\frac{r_j+\epsilon}{r_j}\right)^{\mathbf{\Lambda}^j}\left[\mathbf{I} - \mathbf{R}^{-1}\mathbf{T}\right]\mathbf{U}^{j,j+1}\left(\frac{r_{j+1}-\epsilon}{r_{j+1}}\right)^{-\mathbf{\Lambda}^{i+1}} \tag{B.33b}$$

$$\mathbf{S}_{21}^{j} = 2\left(\frac{r_{j+1}-\epsilon}{r_{j+1}}\right)^{-\mathbf{\Lambda}^{j+1}}(\mathbf{U}^{j,j+1})^{-1}\mathbf{R}^{-1}\mathbf{\Lambda}^{j}\left(\frac{r_j+\epsilon}{r_j}\right)^{\mathbf{\Lambda}^j} \tag{B.33c}$$

$$\mathbf{S}_{22}^{j} = -\left(\frac{r_{j+1}-\epsilon}{r_{j+1}}\right)^{-\mathbf{\Lambda}^{j+1}}(\mathbf{U}^{j,j+1})^{-1}\mathbf{R}^{-1}\mathbf{T}\mathbf{U}^{j,j+1} \left(\frac{r_{j+1}-\epsilon}{r_{j+1}}\right)^{-\mathbf{\Lambda}^{j+1}}. \tag{B.33d}$$

For the odd shells where the $\{a_\mu^j\}$ and $\{b_\mu^j\}$ coefficients are interchanged, the scattering matrices are the same, but the resulting equation is

$$\begin{bmatrix} \boldsymbol{a}^j \\ \boldsymbol{a}^{j+1} \end{bmatrix} = \mathbf{S}^j \begin{bmatrix} \boldsymbol{b}^j \\ \boldsymbol{b}^{j+1} \end{bmatrix}. \tag{B.34}$$

(c) Last Shell $(j = N)$ We now consider the coupling between the the last shell and outside the dielectric. The intermediate matrices are

$$\mathbf{R} = \mathbf{V}^{N,N+1}n_0kR_0\mathbf{H}^{(+)'}(\mathbf{H}^{(+)})^{-1}(\mathbf{U}^{N,N+1})^{-1} + \mathbf{\Lambda}^{N} \tag{B.35a}$$

$$\mathbf{T} = \mathbf{V}^{N,N+1}n_0kR_0\mathbf{H}^{(-)'}(\mathbf{H}^{(-)})^{-1}(\mathbf{U}^{N,N+1})^{-1} + \mathbf{\Lambda}^{N} \tag{B.35b}$$

which gives the block scattering matrices as

$$\mathbf{S}_{11}^{N} = \left(\frac{R_0}{r_N}\right)^{\mathbf{\Lambda}^N} \left[-\mathbf{I} + 2\mathbf{R}^{-1}\mathbf{\Lambda}^N\right] \left(\frac{R_0}{r_N}\right)^{\mathbf{\Lambda}^N} \tag{B.36a}$$

$$\mathbf{S}_{12}^{N} = \left(\frac{R_0}{r_N}\right)^{\mathbf{\Lambda}^N} \left[\mathbf{I} - \mathbf{R}^{-1}\mathbf{T}\right] \mathbf{U}^{N,N+1} n_0 k R_0 \mathbf{H}^{(-)'} \tag{B.36b}$$

$$\mathbf{S}_{21}^{N} = 2\mathbf{H}^{(+)^{-1}} \left(U^{N,N+1}\right)^{-1} \mathbf{R}^{-1}\mathbf{\Lambda}^N \left(\frac{R_0}{r_N}\right)^{\mathbf{\Lambda}^N} \tag{B.36c}$$

$$\mathbf{S}_{22}^{N} = -\mathbf{H}^{(+)^{-1}} \left(U^{N,N+1}\right)^{-1} \mathbf{R}^{-1}\mathbf{T}\mathbf{U}^{N,N+1}\mathbf{H}^{(-)}. \tag{B.36d}$$

We now have the expression for every scattering matrix we need. All that is left is to propagate the solution from the inner shell to the outer shell.

B.1.2 Connecting the Matrices

The following, which we will call the propagation of the solution, allows to write a matrix that expresses the solution outside to the solution inside, i.e.

$$\begin{bmatrix} \boldsymbol{a}^0 \\ \boldsymbol{B} \end{bmatrix} = \mathbf{S}^{0,N} \begin{bmatrix} \boldsymbol{a}^0 \\ \boldsymbol{A} \end{bmatrix}. \tag{B.37}$$

As we shall show, our particular choice of interior solution will allow us to find the scattering matrix $\mathbf{S}$ as $\mathbf{S}_{22}^{0,N}$.

Now, say we're in shell j. We wish to connect the coefficients of this shell with the coefficients of shell $j+2$. First, let us write the linear systems in question:

$$\begin{bmatrix} \boldsymbol{b}^j \\ \boldsymbol{b}^{j+1} \end{bmatrix} = \mathbf{S}^j \begin{bmatrix} \boldsymbol{a}^j \\ \boldsymbol{a}^{j+1} \end{bmatrix}$$
$$\begin{bmatrix} \boldsymbol{a}^{j+1} \\ \boldsymbol{a}^{j+2} \end{bmatrix} = \mathbf{S}^{j+1} \begin{bmatrix} \boldsymbol{b}^{j+1} \\ \boldsymbol{b}^{j+2} \end{bmatrix}$$

where we have interchanged th coefficients for ingoing and outgoing waves. We wish to compute

$$\begin{bmatrix} \boldsymbol{b}^j \\ \boldsymbol{a}^{j+2} \end{bmatrix} = \mathbf{S}^{j,j+1} \begin{bmatrix} \boldsymbol{a}^j \\ \boldsymbol{b}^{j+2} \end{bmatrix} \tag{B.38}$$

Straightforward algebra gives us

$$\mathbf{S}_{11}^{j,j+1} = \mathbf{S}_{11}^{j} + \mathbf{S}_{12}^{j} \left(\mathbf{I} - \mathbf{S}_{11}^{j+1}\mathbf{S}_{22}^{j}\right)^{-1} \mathbf{S}_{11}^{j+1}\mathbf{S}_{21}^{j} \tag{B.39a}$$

$$\mathbf{S}_{12}^{j,j+1} = \mathbf{S}_{12}^{j} \left(\mathbf{I} - \mathbf{S}_{11}^{j+1}\mathbf{S}_{22}^{j}\right)^{-1} \mathbf{S}_{12}^{j+1} \tag{B.39b}$$

$$\mathbf{S}_{21}^{j,j+1} = \mathbf{S}_{21}^{j+1} \left(\mathbf{I} - \mathbf{S}_{22}^{j}\mathbf{S}_{11}^{j+1}\right)^{-1} \mathbf{S}_{21}^{j} \tag{B.39c}$$

$$\mathbf{S}_{22}^{j,j+1} = \mathbf{S}_{22}^{j+1} + \mathbf{S}_{21}^{j+1} \left(\mathbf{I} - \mathbf{S}_{22}^{j}\mathbf{S}_{11}^{j+1}\right)^{-1} \mathbf{S}_{22}^{j}\mathbf{S}_{12}^{j+1}. \tag{B.39d}$$

It is easy to see that this prescribes an iterative procedure. Adding a shell and defining the matrix $\mathbf{S}^{j,j+2}$ makes the same system of equations appear.

We also notice that the matrix $\mathbf{S}^{0,j}$ has an interesting property. Inserting the block scattering matrices for the zeroth and first shell yield

$$\mathbf{S}_{11}^{0,1} = -\mathbf{I} \tag{B.40a}$$
$$\mathbf{S}_{12}^{0,1} = \mathbf{S}_{12}^{0}\left(\mathbf{I}-\mathbf{S}_{11}^{1}\mathbf{S}_{22}^{0}\right)^{-1}\mathbf{S}_{12}^{1} \tag{B.40b}$$
$$\mathbf{S}_{21}^{0,1} = \mathbf{0} \tag{B.40c}$$
$$\mathbf{S}_{22}^{0,1} = \mathbf{S}_{22}^{1} + \mathbf{S}_{21}^{1}\left(\mathbf{I}-\mathbf{S}_{22}^{0}\mathbf{S}_{11}^{1}\right)^{-1}\mathbf{S}_{22}^{0}\mathbf{S}_{12}^{1} \tag{B.40d}$$

Notice that the iterative procedure yields the same values for $\mathbf{S}_{11}^{0,j}$ and $\mathbf{S}_{21}^{0,j}$, $\forall j$. They are essentially fixed points of this iterative process. It is this exact property that allows us to say that the scattering matrix is $\mathbf{S}_{22}^{0,N}$.

B.2 Lippmann-Schwinger Computation of the Scattering Matrix: Scalar Case

The final method discussed in this Appendix is, according to the author, the most promising. Its implementation, however, is not totally complete. We will here share its most salient details and some preliminary results. We will also show the formalism only the TM case, as the TE case requires a little more analysis [114].

B.2.1 Analysis and Derivation of Integral Formulation

The first step is to notice that we can write (B.1) as

$$\left[\nabla^2 + k^2 n_o^2\right]\psi = -k^2\left(n_c^2 - n_0^2\right)\psi \qquad \boldsymbol{r} \in \mathbb{R}^2 \tag{B.41}$$

where the r.h.s can be seen as a forcing function. This inhomogeneous differential equation can be solved by using the Green's function of the homogeneous problem. We have

$$\left[\nabla^2 + k^2 n_0^2\right]G(\boldsymbol{r}-\boldsymbol{r}') = \delta(\boldsymbol{r}-\boldsymbol{r}') \tag{B.42}$$

where $G(\boldsymbol{r}-\boldsymbol{r}')$ is the Green function and $\delta(\boldsymbol{r}-\boldsymbol{r}')$ a Dirac delta function, used to model a point source. To solve the equation, we must enforce Sommerfeld's radiation condition. The well-known solution is [5] is

$$G_\omega(\boldsymbol{r}-\boldsymbol{r}') = -\frac{i}{4}H_0^{(\omega)}(kn_0|\boldsymbol{r}-\boldsymbol{r}'|). \tag{B.43}$$

Because we deal with outgoing waves at infinity, we take $G = G_+$. Multiplying (B.42) by ψ, integrating over all space and using the compact support of $n_c^2 - n_0^2$, we have

$$\psi(\boldsymbol{r}) = \phi(\boldsymbol{r}) - k^2 \iint_{\mathscr{C}} G(\boldsymbol{r},\boldsymbol{r}')\Delta n^2(\boldsymbol{r}')\psi(\boldsymbol{r}')d^2\boldsymbol{r}' \tag{B.44}$$

where $\phi(\boldsymbol{r})$ is a solution of the homogeneous equation and $\Delta n^2 = n_c^2 - n_0^2$. We have arrived at an implicit volume integral equation[2] for the field inside the scatterer. It is a Fredholm problem of the second kind with a weakly singular kernel $G(\boldsymbol{r}-\boldsymbol{r}')\Delta n^2(\boldsymbol{r}')$ [140] and has thus a well-behaved solution. It is also called a Lippmann-Schwinger equation.

Before detailing the numerical algorithm we will use to solve the problem, we will discuss the computation of the scattering matrix. If we solve the problem with $\phi(\boldsymbol{r}) = J_M(kn_0 r)e^{iM\theta}$, the eigenfunction of the problem, we obtain

$$\psi(\boldsymbol{r}) = J_M(kn_0 r)e^{iM\theta} - k^2 \iint_{\mathscr{C}} G(\boldsymbol{r},\boldsymbol{r}')\Delta n^2(\boldsymbol{r}')\psi(\boldsymbol{r}')d^2\boldsymbol{r}'. \tag{B.45}$$

and solve the field within $\mathscr{C}$. In what follows, we will need to use the partial wave expansion of Green's function, given by [141]

$$G(\boldsymbol{r},\boldsymbol{r}') = -\frac{i}{4}H_0^{(+)}(kn_0|\boldsymbol{r}-\boldsymbol{r}'|) = -\frac{i}{4}\sum_m J_m(kn_0 r_<)H_m^{(+)}(kn_0 r_>)e^{im(\theta-\theta')} \tag{B.46}$$

where $r_< = \min(|\boldsymbol{r}|,|\boldsymbol{r}'|)$ and $r_> = \max(|\boldsymbol{r}|,|\boldsymbol{r}'|)$. We can now write an equation for the field outside the last scattering surface (where the **S**-matrix is defined)

$$\psi(\boldsymbol{r}) = J_M(kn_0 r)e^{iM\theta} - \frac{ik^2}{4}\sum_m H_m^{(+)}(kn_0 r)e^{im\theta}\iint_{\mathscr{C}} J_m(kn_0 r')e^{-im\theta'}\Delta n^2(\boldsymbol{r}')\psi(\boldsymbol{r}')d^2\boldsymbol{r}' \tag{B.47}$$

where we could pull out the Hankel function out of the integral since $r_> = r$ outside the last scattering surface. We can rewrite this as

$$\begin{aligned} 2\psi(\boldsymbol{r}) = {} & H_M^{(-)}(kn_0 r)e^{iM\theta} + H_M^{(+)}(kn_0 r)e^{iM\theta} \\ & - \frac{ik^2}{4}\sum_m H_m^{(+)}(kn_0 r)e^{im\theta}\iint_{\mathscr{C}} J_m(kn_0 r')e^{-im\theta'}\Delta n^2(\boldsymbol{r}')\psi(\boldsymbol{r}')d^2\boldsymbol{r}' \end{aligned} \tag{B.48}$$

We can now invoke the definition of the **S**-matrix

$$2\psi(\boldsymbol{r}) = H_M^{(-)}(kn_0 r)e^{iM\theta} + \sum_m S_{Mm}(k)H_m^{(+)}(kn_0 r)e^{im\theta}. \tag{B.49}$$

We can now "read off" the elements of the **S**-matrix from the previous equation as

$$S_{Mm} = \delta_{Mm} - \frac{ik^2}{2}\iint_{\mathscr{C}} J_m(kn_0 r')e^{-im\theta'}\Delta n^2(\boldsymbol{r}')\psi(\boldsymbol{r}')d^2\boldsymbol{r}'. \tag{B.50}$$

[2] For homogeneous cavities, i.e. where n_c^2 is a constant function, it is better to use boundary integral methods [122, 139], as they greatly reduce the discretization needed, among other things.

B.2.2 Numerical Solution

The integral formulation can accommodate dispersive, inhomogeneous and even non-linear refractive indices. However, since we are mostly interested in linear scatterers, we will turn the integral problem into a system of linear equations[3].

To do so, we must mesh the cavity region $\mathscr{C}$. We use a simple Delaunay triangulation, with points distributed uniformly in the area of $\mathscr{C}$. We then suppose that the field is constant inside each triangle and use the centre of the triangle[4] as the reference point for each triangle. We will note the value of the field at the centre point $\psi(\boldsymbol{r}_j) = \psi_j$[5], where j in an index that runs over every triangle. Let us call the set of triangles generated by the Delaunay triangulation Δ. We can rewrite the integral equation as

$$\psi_j = \phi_j - k^2 \sum_{j'=0}^{|\Delta|} G_{jj'} \Delta n_{j'}^2 A_{j'} \psi_{j'} \tag{B.51}$$

where A_j is the area of triangle j and serves as our measure. Forming a vector $\boldsymbol{\psi}$ containing every ψ_j, we can rewrite this equation as

$$(\mathbf{I} + \mathbf{K})\boldsymbol{\psi} = \boldsymbol{\phi} \tag{B.52}$$

where $K_{jj'} = G_{jj'} \Delta n_{j'}^2 A_{j'}$ is the discretized kernel. Notice that the diagonal elements of the kernel diverge logarithmically, as

$$H_0^{(+)}(kn_0|\boldsymbol{r} - \boldsymbol{r}'|) \sim \ln(kn_0|\boldsymbol{r} - \boldsymbol{r}'|). \tag{B.53}$$

Even though the singularity is integrable and that analytical results exist in the literature [113, 143], we simply ignore the diagonal contribution. This is fine for low accuracy work, but will need to be dealt with more appropriately in the future.

B.2.2.1 Circular, Homogeneous Cavity

As a test for the method, we will compute the scattering matrix of the circular, homogeneous cavity. A typical mesh produced by the Delaunay triangulation is shown in Figure B.1. We then solve the scattering problem with $\phi_m(\boldsymbol{r}) = J_m(kn_0 r)e^{im\theta}$ and compute the elements of the scattering matrix.

Figures B.2 shows the field intensity inside the cavity when $\phi(\boldsymbol{r}) = J_0(kn_0 r)$, i.e. the only eigenfunction with vanishing angular momentum. We see that the field maintains its main features when a finer mesh is used, indicative of the convergence of the method.

[3] We could also use the eigenbasis expansion of the Green's function (B.46) and of the field and solve for the eigenmodes. This proves to be unstable, however, and difficult to generalize in the 3D cylindrical coordinates [142].

[4] Specifically, we use the centroid of each triangle. It is computed by introducing a trilinear coordinate system in each triangle, subsequently transforming the centroid position in our global Cartesian system.

[5] And similarly for the other quantities.

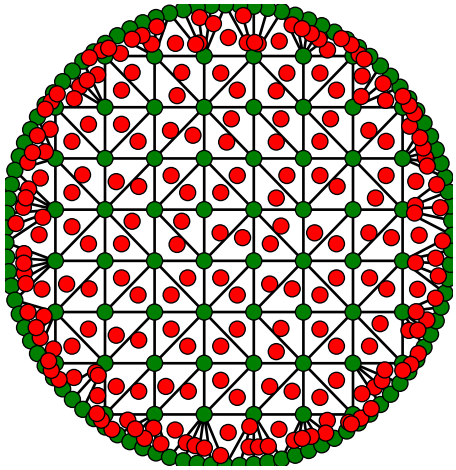

Figure B.1 – A typical mesh produced by the Delaunay triangulation. Here, 100 points were distrubuted along the boundary, with another 100 inside the perimeter of the cavity. The green dots represent the nodes of the mesh. The red dots are the centroids of each triangle.

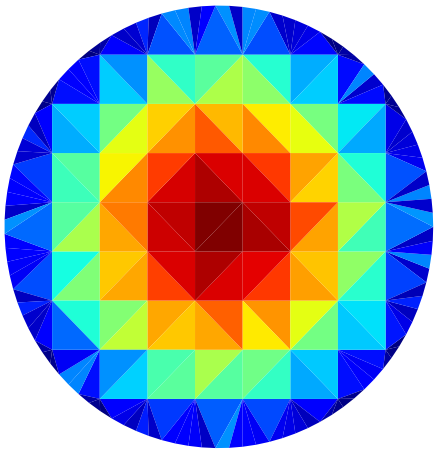

(a) Intensity of the field inside the cavity when $J_0(n_0 kr)$ is the incoming field. This mesh contains 100 points on the boundary and 100 more inside the perimeter.

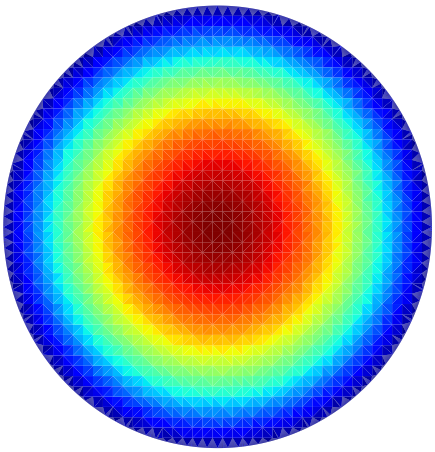

(b) Intensity of the field inside the cavity when $J_0(kn_0 r)$ is the incoming field. This mesh contains 2000 points on the boundary and 2000 more inside the perimeter.

Figure B.2 – Intensity of the field inside the cavity for two different meshes. We use $\phi(\boldsymbol{r}) = J_0(kn_0 r)$ as the incoming field.

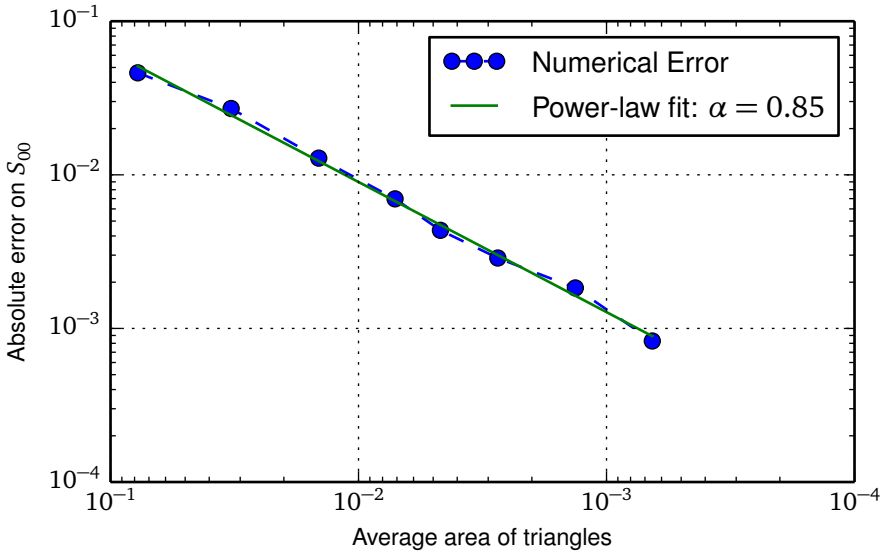

Figure B.3 – Convergence analysis of the integral method. We compute the difference between the analytical and numerical values of $S_{00}(k)$ for the homogeneous, circular cavity. The parameters are $k = 1$, $R_0 = 1$, $n_c = 1.5$ and $n_0 = 1$.

The convergence is confirmed to be linear in the average area in the triangles in Figure B.3. The fact that it is slightly slower than linear can probably be attributed to the fact that we have neglected the diagonal parts of the kernel.

B.3 Lippmann-Schwinger Computation of the Scattering Matrix: Vector Case

We repeat the procedure of the previous section, but for the complete 3D vector field. Similar methods are presented in [144, 145]. As always, our starting point is the couple

$$\nabla \times \boldsymbol{E} = ik\mu \boldsymbol{H} \qquad \nabla \times \boldsymbol{H} = -ik\epsilon \boldsymbol{E}. \tag{B.54}$$

Taking the curl of the first equation and going through the motions, we can obtain the equation

$$\nabla^2 \boldsymbol{E} + k^2 \epsilon_{\mathrm{B}} \mu_{\mathrm{B}} \boldsymbol{E} = -k^2 \mu_{\mathrm{B}} \Delta\epsilon \boldsymbol{E} + \nabla \left\{ \frac{1}{\epsilon_c} \boldsymbol{E} \cdot \nabla \epsilon_c \right\} + \mu_{\mathrm{B}} \nabla \times \left(\Delta\mu^{-1} \nabla \times \boldsymbol{E} \right) \tag{B.55}$$

where μ_{B} and ϵ_{B} are the permeability and permittivity of the environment and where the supports of the functions

$$\Delta\epsilon = \epsilon_c - \epsilon_{\mathrm{B}} \qquad \Delta\mu^{-1} = \mu_c^{-1} - \mu_{\mathrm{B}}^{-1} \tag{B.56}$$

are supposed to coincide with the cavity region $\mathscr{C}$, with, now, $\mathscr{C} \subset \mathbb{R}^3$. ϵ_c and μ_c are the physical parameters of the cavity region and allowed to be non-linear, position- and frequency-dependent. Once again, we have to solve an inhomogeneous partial differential equation. We will use the

tensorial Green's function[6], given by [47]

$$\mathbf{G}(\boldsymbol{r}',\boldsymbol{r}') = -\mathbf{I}\frac{e^{ikn_{\mathrm{B}}|\boldsymbol{r}-\boldsymbol{r}'|}}{4\pi|\boldsymbol{r}-\boldsymbol{r}'|}. \tag{B.57}$$

where $n_B = \sqrt{\epsilon_B \mu_B}$. We can thus write a formal solution to the scattering problem as

$$\boldsymbol{E}(\boldsymbol{r}) = \boldsymbol{E}^i(\boldsymbol{r}) + \iiint_{\mathscr{C}} \mathbf{G}(\boldsymbol{r},\boldsymbol{r}')\big[V(\boldsymbol{r}')\boldsymbol{E}(\boldsymbol{r}')\big]d^3\boldsymbol{r}' \tag{B.58}$$

where we have written the r.h.s. of (B.55) as the operator

$$V(\boldsymbol{r})\{\} = -k^2\mu_B\Delta\epsilon\,\{\} + \nabla\left\{\frac{1}{\epsilon_c}\{\}\cdot\nabla\epsilon_c\right\} + \mu_B\nabla\times\left(\Delta\mu^{-1}\nabla\times\{\}\right). \tag{B.59}$$

Once again, this Lippmann-Schwinger equation can be used to compute the scattering tensor of the problem. If we use the eigenfunction as the incoming field, we have

$$\boldsymbol{E}(\boldsymbol{r}) = j_L(n_B kr)\boldsymbol{Y}^L_{JM}(\theta,\varphi) + \iiint_{\mathscr{C}} \mathbf{G}(\boldsymbol{r},\boldsymbol{r}')\big[V(\boldsymbol{r}')\boldsymbol{E}(\boldsymbol{r}')\big]d^3\boldsymbol{r}' \tag{B.60}$$

where the vector spherical harmonics are given by a combination of the scalar spherical harmonics

$$\boldsymbol{Y}^\ell_{jm} = \sum_{m'}\sum_{\sigma} C^{jm}_{lm',1\sigma}Y^{m'}_\ell(\theta,\varphi)\hat{\boldsymbol{e}}_\sigma \tag{B.61}$$

where $C^{j_3m_3}_{j_1m_1,j_2m_2}$ are the Clebsch-Gordan coefficients and where the $\hat{\boldsymbol{e}}_\sigma$ are the unit vectors of the covariant spherical coordinate system [146]. We will use the expansion

$$\mathbf{G}(\boldsymbol{r},\boldsymbol{r}') = -ik\sum_{j,\ell,m} j_\ell(n_B kr_<)h^{(+)}_\ell(n_B kr_>)\boldsymbol{Y}^\ell_{jm}(\theta,\varphi)\otimes\boldsymbol{Y}^{\ell *}_{jm}(\theta',\varphi'). \tag{B.62}$$

Using the same technique as before, i.e. substituting the expansion in the integral equation for the field outside the last scattering surface and invoking the definition of the scattering matrix, we obtain

$$S_{j\ell m,JLM} = \delta_{j\ell m,JLM} - 2ik\iiint_{\mathscr{C}} j_\ell(kn_B r')\boldsymbol{Y}^{j*}_{\ell m}V(\boldsymbol{r}')\boldsymbol{E}(\boldsymbol{r}')d^3\boldsymbol{r}'. \tag{B.63}$$

To compute the scattering tensor, however, we must necessarily solve an integro-differential equation. We will not delve into the subject, as it is beyond the scope of this essay. However, it could be solved via a Galerkin method.

The curl-curl equation yields a simple integral method when the material is non-magnetic, but it seems impossible to recover our simple expression for the scattering tensor.

[6] In the literature, it is called a dyadic Green's function. This nomenclature is archaic and should not be used in modern texts.

Appendix C

Numerical Tools

The numerical tools developed here are printed in this essay for future reference. They all have some part to play in the generalization to three dimensions of the numerical methods discussed in this essay.

C.1 Computation of the Logarithmic Derivative $[H_\nu^{(\pm)}(z)]'/H_\nu^{(\pm)}(z)$

The computation of the logarithmic derivative of Bessel functions is of the utmost importance in the numerical solution of scattering problems. Given that we already use Amos' library [147] to evaluate the Bessel functions, we might have been tempted to use it to directly evaluate the derivative. It turns out that using expansions that pertain to logarithmic derivatives is somewhat faster and is more accurate than using Amos' library.

In this section, we introduce some concepts relating to continued fraction expansions (CFEs) and discuss their numerical evaluation. We then derive the CFEs and other expansions that will be of use in the computation of the logarithmic derivatives.

C.1.1 Notation and Necessary Theorems

A continued fraction expansion is a representation of a mathemetical function. It can be linked to Laurent series, Padé approximants and much more [136]. It has the standard form

$$f = b_0 + \cfrac{a_1}{b_1 + \cfrac{a_2}{b_2 + \cfrac{a_3}{b_3 + \cfrac{a_4}{b_4 + \cdots}}}} \tag{C.1}$$

or, more succinctly,

$$f = b_0 + \operatorname*{\mathbf{K}}_{m=1}^{\infty}\left(\frac{a_m}{b_m}\right) \tag{C.2}$$

where 'K' is for the German word *Kettenbruch*, meaning continued fraction. We define the nth approximant as

$$f_n = b_0 + \operatorname*{\mathbf{K}}_{m=1}^{n}\left(\frac{a_m}{b_m}\right). \tag{C.3}$$

We will be concerned with their numerical evaluation and convergence properties.

Notice that naïvely evaluating the CFE from right-to-left, as a person would do, does not yield a satisfying numerical algorithm, as the amount of iterations must be fixed in advance and consequently does not allow the control the accuracy of the evaluation. The chosen method is taken from the Holy Bible of Numerics, *Numerical Recipes* [137] and is called the modified Lentz's method. It constructs a rational approximation of the nth approximant

$$f_n = \frac{A_n}{B_n} \tag{C.4}$$

where

$$\begin{aligned} A_{-1} &= 1 & B_{-1} &= 0 \\ A_0 &= b_0 & B_0 &= 1 \\ A_j &= b_j A_{j-1} + a_j A_{j-2} & B_j &= b_j B_{j-1} + a_j B_{j-2}. \end{aligned} \tag{C.5}$$

This method can lead to over/underflow of the floating-point representation: the method hence uses

$$\begin{aligned} C_j &= A_j/A_{j-1} & D_j &= B_{j-1}/B_j \\ &= b_j + \frac{a_j}{C_{j-1}} & &= \frac{1}{b_j + a_j D_{j-1}} \\ f_j &= f_{j-1} C_j D_j. \end{aligned} \tag{C.6}$$

The method is aptly described by Algorithm 1. It allows for a left-to-right evaluation of the CFE and control of the relative accuracy of the computation.

As for the convergence properties, we will only bother with CFEs originating from three-term recurrence relations. Indeed, it turns out that any three-term recurrence relation can be linked to a CFE. Consider

$$y_{n+1} + a_n y_n + b_n y_{n-1} = 0. \tag{C.7}$$

It can be rewritten as

$$\frac{y_n}{y_{n-1}} = -\frac{b_n}{a_n + y_{n+1}/y_n}. \tag{C.8}$$

Iterating yields the CFE

$$\frac{y_n}{y_{n-1}} = \operatorname*{\mathbf{K}}_{m=n}^{\infty}\left(\frac{-b_m}{a_m}\right). \tag{C.9}$$

Algorithm 1: Evaluation of Continued Fractions

Data: `tiny` = square root of smallest representable number
Data: `eps` = accuracy of the CFE
if $b_0 = 0$ **then**
  $f_0 \leftarrow$`tiny`
else
  $f_0 \leftarrow 0$
$C_0 \leftarrow f_0$;
$D_0 \leftarrow 0$;
repeat from $j = 1$
  $D_j \leftarrow b_j + a_j D_{j-1}$;
  if $D_j = 0$ **then**
    $D_j \leftarrow$`tiny`
  $C_j \leftarrow b_j + \frac{a_j}{C_{j-1}}$;
  if $C_j = 0$ **then**
    $C_j \leftarrow$`tiny`
  $D_j \leftarrow 1/D_j$;
  $\Delta_j \leftarrow C_j D_j$;
  $f_j \leftarrow f_{j-1}\Delta_j$
until $|\Delta_j - 1| <$`eps`;
return f_j

Given our goal of computing $[H_\nu^{(\pm)}(z)]'/H_\nu^{(\pm)}(z)$ and in light of (A.6), it seems that we have won. The next theorem, however, will prove us wrong.

Theorem C.1 (Pincherle's Theorem [136])**.** *If there exists a minimal solution u_n of the three-term recurrence relation (C.7), the associated CFE (C.9) converges to u_n/u_{n-1}. A solution is said minimal if there exists another solution v_n such that*

$$\lim_{n\to\infty} \frac{u_n}{v_n} = 0. \tag{C.10}$$

v_n is said to be the dominant solution. The minimal solution is unique.

Because the minimal solution of (A.6a) if $J_\nu(z)$, we cannot use the associated CFE to compute the logarithmic derivatives of Hankel functions. Instead, we must look into the links between Hankel functions and confluent hypergeometric functions.

C.1.2 CFE and Other Expansions

In this brief foray into the vast subject of hypergeometric functions, we will introduce Kummer's confluent hypergeometric function of the second kind and its link to the evaluation of the logarithmic derivative.

Kummer's function solves the differential equation [135, §13.1.1]

$$z\frac{d^2y}{dz^2}+(b-z)\frac{dy}{dz}-ay=0 \tag{C.11}$$

and is noted $U(a,b,z)$[1]. It can be shown that that $u_k=(a)_k U(a+k,b,z)$ is the minimal solution of the recurrence [148]

$$u_{n+1}=\frac{2a-b+2n+z}{a-b+n+1}u_n-\frac{a+n-1}{a-b+n+1}u_{n-1} \tag{C.12}$$

where $(a)_k$ is the Pochhammer symbol. We can hence derive

$$\frac{U(a,b,z)}{U(a+1,b,z)}=2a-b+2+z-\mathop{\mathrm{K}}_{m=1}^{\infty}\left(\frac{(a+m)(b-a-m-1)}{b-2a-2m-2-z}\right). \tag{C.13}$$

Combined with [135, §13.4.23]

$$U(a+1,b,z)=\frac{1}{1+a-b}U(a,b,z)+\frac{z}{a(1+a-b)}U'(a,b,z), \tag{C.14}$$

we obtain [136]

$$\frac{dU(a,b,z)/dz}{U(a,b,z)}=-\frac{a}{z}+\frac{a(1+a-b)/z}{2a-b+2+z-}\mathop{\mathrm{K}}_{m=1}^{\infty}\left(\frac{(a+m)(b-a-m-1)}{b-2a-2m-2-z}\right). \tag{C.15}$$

Given the relation between Kummer's functions and Hankel functions $H_\nu^\omega(z)$ [135, §13.6.22/23]

$$H_\nu^\omega(z)=\frac{2}{\sqrt{\pi}}e^{-\omega[\pi(\nu+1/2)-z]}(2z)^\nu U(\nu+1/2,2\nu+1,-2i\omega z)\qquad(\omega=\pm) \tag{C.16}$$

we can finally find the CFE

$$\frac{dH_\nu^\omega(z)/dz}{H_\nu^\omega(z)}=-\frac{1}{2z}+i\omega+\frac{\omega}{z}\mathop{\mathrm{K}}_{m=1}^{\infty}\left(\frac{\nu^2-(2m-1)^2/4}{2(iz-\omega m)}\right). \tag{C.17}$$

In our numerical implementation (see next section), we have found that when $|z|<10^{-2}$, convergence is slow. This mirrors the results of [149]. We thus use the small argument expansions for the Bessel functions (*q.v.* §A.2.1) to obtain

$$\lim_{z\to0}\frac{dH_\nu^\omega(z)/dz}{H_\nu^\omega(z)}=-\frac{\nu}{z}\qquad(\nu\neq0) \tag{C.18a}$$

$$=\frac{1}{z}\left[\frac{\pi}{2i\omega}+\gamma+\ln\left(\frac{z}{2}\right)\right]^{-1}\qquad(\nu=0). \tag{C.18b}$$

[1] In fact, there are two functions known as "Kummer's function". The first is the confluent hypergeometric function of the first kind, defined by

$$M(a,b,z)={}_1F_1(a;b;z)=\sum_{k=0}^{\infty}\frac{(a)_k}{(b)_k}\frac{z^k}{k!}.$$

We use the confluent hypergeometric function of the second kind, or

$$U(a,b,z)=\frac{\Gamma(1-b)}{\Gamma(a-b+1)}{}_1F_1(a;b;z)+z^{1-b}\frac{\Gamma(b-1)}{\Gamma(a)}{}_1F_1(a-b+1;2-b;z).$$

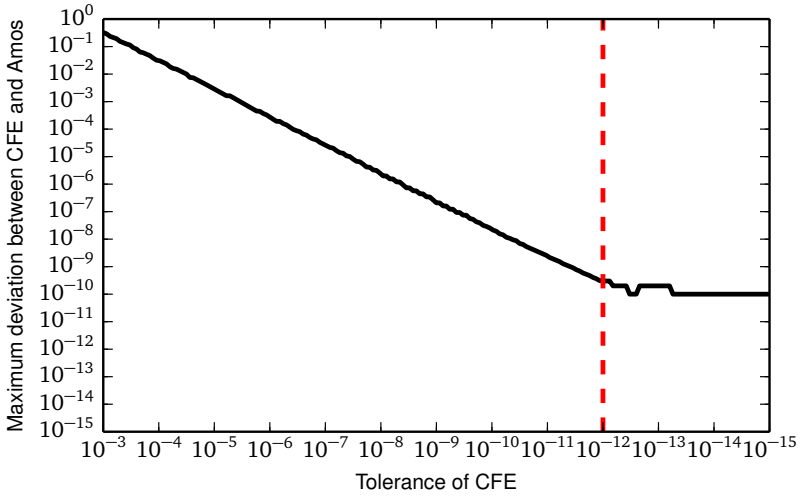

Figure C.1 – Maximum deviation between the CFE and Amos' implementation of the Bessel functions as a function of the tolerance of the CFE. This study was performed in the parameter space $z \in \{0.1, 10\}$, $\nu \in \{-100, 100\}$. We interpret the plateau in maximum deviation as the error committed by Amos' implementation, i.e. Amos' implementation has a precision of $\sim 10^{-10}$ on the evaluation of the logarithmic derivative.

C.1.3 Numerical Tests

We have performed a number of tests to ascertain the performance of our algorithm. To test the precision of the algorithm, we have evaluated the CFE for $z \in \{0, 10\}$ and $\nu \in \{-100, 100\} \in \mathbb{N}$ and compared it to the values obtained via Amos' library for a range of tolerances. It can be seen that the maximum deviation decreases until our set tolerance hits 10^{-12} and then plateaus. Because convergence of C.17 is mathematically ensured, we conclude that Amos's library evaluate the logarithmic derivative up to a precision of 10^{-12}. This is probably due to the propagation of errors in the floating point operations, as we use relation (A.6b) to evaluate the derivative.

However, it can be seen that Amos' library is somewhat faster, given its precision, that our CFE evaluation even though it requires three Hankel function evaluations.

C.2 Clebsch-Gordan Coefficients and Wigner Symbols

Before discussing the Wigner symbols, we introduce the Clebsch-Gordan coefficients as they appear quite naturally in the quantum theory of angular momentum. Specifically, they are needed to study the coupling of two systems having definite angular momenta. The material in this section is inspired by [146, 150].

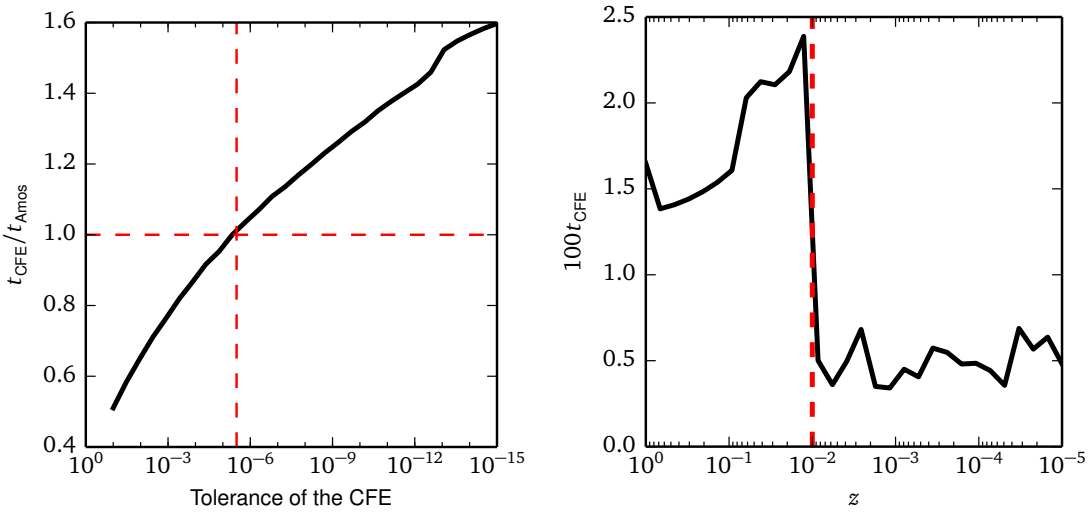

(a) Performance of the CFE implementation as a function of its tolerance. We measured the ratio of the time it takes to compute the logarithmic derivative at $z = 0$ for all orders $\nu \in \{-100, 100\}$ with the CFE and Amos' implementation. When the tolerance of the CFE hits $\sim 10^{-5.5}$, the CFE is slower than Amos' implementation.

(b) Performance of the CFE as a function of z. When approaching $z = 0$ (from all sides), it takes a higher number of terms for the CFE to converge, resulting in a slower algorithm. However, at $z = 10^{-2}$, we use the small argument form, preserving both precision and performance.

Figure C.2 – Performance of the CFE compared to that of Amos' library. The CFE is somewhat slower, but can achieve better precision.

C.2.1 Formal definitions

C.2.1.1 Clebsch-Gordan coefficients and Wigner 3j-symbols

Given two states that can be described by two quantum numbers pertaining to their angular momenta, say $|j_1 m_1\rangle$ and $|j_2 m_2\rangle$ where j_1 and j_2 are the total angular momenta and m_1 and m_2 are their z-projections. The states span two different vectors spaces, ξ_1 and ξ_2. To measure the angular momentum and associated z-projection of the composite system, call them j_3 and m_3, we look at the states spanning the product space $\xi_1 \otimes \xi_2$. The product states can be written

$$|j_3 m_3\rangle = \sum_{m_1} \sum_{m_2} |j_1 m_1 j_2 m_2\rangle \langle j_1 m_1 j_2 m_2 | j_3 m_3\rangle \tag{C.19}$$

where

$$|j_1 m_1 j_2 m_2\rangle = |j_1 m_1\rangle \otimes |j_2 m_2\rangle$$

and where the allowed values of j_3 and m_3 follow from the quantum vector addition rules.

A similar relation holds for the bra. This equation simply describes the expansion of the a vector in the product space $\xi_1 \otimes \xi_2$ in the product of the bases of ξ_1 and ξ_2 [151]. The expansion

coefficients are known as the Clebsch-Gordan coefficients. Their square represent the probability that a measurement of the angular momentum yields a value of $\sqrt{j_3(j_3+1)}\hbar$.

We will note the Clebsch-Gordan coefficients as

$$C^{j_3 m_3}_{j_1 m_1, j_2 m_2} = \langle j_1 m_1 j_2 m_2 | j_3 m_3 \rangle \,. \tag{C.20}$$

We can now introduce the Wigner $3j$-symbols. They are be related to the Clebsch-Gordan coefficients through

$$\begin{pmatrix} j_1 & j_2 & j_3 \\ m_1 & m_2 & m_3 \end{pmatrix} = \frac{(-1)^{j_1 - j_2 - m_3}}{\sqrt{2j_3+1}} \langle j_1 m_1 j_2 m_2 | j_3 - m_3 \rangle \,. \tag{C.21}$$

More telling, though, is their interpretation as the probability that three angular momenta couple to give zero angular momentum, or

$$\begin{pmatrix} j_1 & j_2 & j_3 \\ m_1 & m_2 & m_3 \end{pmatrix} = (-1)^{j_1 - j_2 + j_3} \sum_{j'm'} C^{j'm'}_{j_1 m_1, j_2 m_2} C^{00}_{j'm', j_3 m_3}. \tag{C.22}$$

The $3j$-symbols also appear in the angular integration of three spherical harmonics

$$\iint_\Omega Y_{j_1,m_1}(\theta,\varphi) Y_{j_2,m_2}(\theta,\varphi) Y_{j_3,m_3}(\theta,\varphi) d\Omega = \sqrt{\frac{(2j_1+1)(2j_2+1)(2j_3+1)}{4\pi}} \begin{pmatrix} j_1 & j_2 & j_3 \\ 0 & 0 & 0 \end{pmatrix} \begin{pmatrix} j_1 & j_2 & j_3 \\ m_1 & m_2 & m_3 \end{pmatrix} \tag{C.23}$$

C.2.1.2 Wigner $6j$-symbols

The $6j$-symbols are related to the coupling of three angular momenta. In this case, the resultant angular momentum $\boldsymbol{j}$ can be obtained via three different coupling schemes:

I. $\boldsymbol{j}_1 + \boldsymbol{j}_2 = \boldsymbol{j}_{12}, \qquad \boldsymbol{j}_{12} + \boldsymbol{j}_3 = \boldsymbol{j};$

II. $\boldsymbol{j}_2 + \boldsymbol{j}_3 = \boldsymbol{j}_{23}, \qquad \boldsymbol{j}_1 + \boldsymbol{j}_{23} = \boldsymbol{j};$

III. $\boldsymbol{j}_1 + \boldsymbol{j}_3 = \boldsymbol{j}_{13}, \qquad \boldsymbol{j}_{13} + \boldsymbol{j}_2 = \boldsymbol{j}.$

Each coupling scheme has a set of associated *generalized Clebsch-Gordan* coefficients which gives the coefficients of the expansion of a state vector in the basis of $|j_1 m_1, j_2 m_2, j_3 m_3\rangle$. For instance, a state corresponding to coupling scheme I has expansion

$$|j_1 j_2 (j_{12}), j_3 j m\rangle = \sum_{m_1, m_2, m_3} C^{jm}_{j_{12} m_{12} j_3 m_3} C^{j_{12} m_{12}}_{j_1 m_1 j_2 m_2} |j_1 m_1, j_2 m_2, j_3 m_3\rangle \tag{C.24}$$

with similar expressions holding for the other coupling schemes.

We thus define the $6j$-symbols as the coefficients of the unitary transformation that takes us from one scheme to another [146]. We can then write

$$\begin{Bmatrix} j_1 & j_2 & j_3 \\ j_4 & j_5 & j_6 \end{Bmatrix} = \frac{(-1)^{j_1+j_2+j_4+j_5}}{\sqrt{(2j_3+1)(2j_6+1)}} \sum_{m_1,m_2,m_3,m_4,m_6} C^{j_5 m_5}_{j_3 m_3, j_4 m_4} C^{j_3 m_3}_{j_1 m_1, j_2 m_2} C^{j_5 m_5}_{j_1 m_1, j_6 m_6} C^{j_6 m_6}_{j_2 m_2, j_4 m_4} \quad \text{(C.25)}$$

We can also define higher-order Wigner symbols, but things rapidly become complicated [152].

C.2.2 Numerical Computation of Wigner Symbols

The previous section dealt with the definitions of the Clebsch-Gordan coefficients and the Wigner symbols. While more (much, much more) could have been said on the subject, we will now discuss the actual evaluation of these numbers.

We note that the Condon-Shortley phase convention ensures that all Clebsch-Gordan coefficients and Wigner symbols are real, which is a real numerical advantage.

Moreover, there exists closed-forms formulas in the form of algebraic sums for the Wigner symbols, but they are riddled with numerical issues, such as the cancellation of large terms and the evaluation of the ratio of large factorial arguments.

The best way to evaluate the coefficient was devised in 1975 by chemical physicist K. Schulten [153]. He and R. G. Gordon rederived three-term recursion relation for the Wigner symbols and used them to evaluate sets of Wigner symbols at a time. Fortran code exists[2], but our tests showed only `single` numerical precision. We have thus reprogrammed the algorithm, first described in [153] and detailed in [154], in C++.

Before detailing our results, we will briefly overview the algorithm used (*see* Fgure C.4. We compute

$$\begin{pmatrix} j_1 & j_2 & j_3 \\ m_1 & m_2 & m_3 \end{pmatrix} \quad \forall j_1$$
$$\begin{Bmatrix} j_1 & j_2 & j_3 \\ j_4 & j_5 & j_6 \end{Bmatrix} \quad \forall j_1$$

We can write the recursion relations valid for both symbols as (we adopt the notation of [155])

$$\alpha_\psi(j_1)\psi(j_1+1) + \beta_\psi(j_1)\psi(j_1) + \gamma_\psi(j_1)\psi(j_1-1) = 0 \quad \text{(C.26)}$$

where $\psi(j_1)$ represents either the $3j$- or $6j$-symbol at j_1 and the Greek letters are the coefficient at that j_1. They are shown in Table C.1.

[2] http://cpc.cs.qub.ac.uk/summaries/ACWQ_v1_0.html

To start the recursion, we would usually need two initial conditions. It turns out, however, that the recursion relations reduce to only two terms at the boundaries $j_{1\min}$ and $j_{1\max}$. Like all other numerical schemes, recursion relations are only stable in the direction of increasing coupling coefficients. Semi-classical analysis [153] informs us that there generally exists three regions of interest for the function $\psi(j_1)$. Near the boundaries, we are in the nonclassical regions. At the lower values of j_1, $\psi(j_1)$ is increasing until it hits the central classical region, where it starts oscillating. On the other hand, near the $j_{1\max}$ boundaries, the coefficients are increasing with decreasing j_1. Given the linearity of the recursion relations, we can start the recursion relations from both boundaries using a sufficiently small but otherwise *arbitrary* number. While the ratios between successive values of the coupling coefficients will be correct, their absolute values will not. The forward and backward recurrences will be multiplied by a scalar, call them c_1 for the forward recursion and d_1 for the backward recursion. To find the relationship between the scalars, we watch the values of the forward and backward recursions at some intermediary point. For more numerical stability, we use three contiguous values around the intermediary point and find the parameter $\lambda = {}^{d_1}/_{c_1}$ from a least-squares fit. To choose the intermediary point, we note that the recursion relations appear in the form

$$\psi(j_1+1) = X(j_1)\psi(j_1) + Y(j_1)\psi(j_1-1). \tag{C.27}$$

Schulten found that, using semiclassical analysis, that $|X(j_1)|$ attains its minimum value in the classical domain. Monitoring the variation of $|X(j_1)|$ thus provides a way to find the intermediary point.

The overall scaling factor c_1 is found and the set of coupling coefficients is rescaled to its proper value by using the normalization condition on the computed set.

We note that if the total size of the set is 1 ($j_{1\min} = j_{1\max}$), we can deduce, from the triangular condition, that $l_2 \vee l_3 = 0$. We thus have to evaluate the $3j$-symbols

$$\begin{aligned}
\begin{pmatrix} l_3 & 0 & l_3 \\ -m_3 & 0 & m_3 \end{pmatrix} &= \begin{pmatrix} l_3 & l_3 & 0 \\ m_3 & -m_3 & 0 \end{pmatrix} = \frac{(-1)^{l_3-m_3}}{\sqrt{2l_3+1}} \\
\begin{pmatrix} l_2 & l_2 & 0 \\ -m_2 & m_2 & 0 \end{pmatrix} &= (-1)^{-2l_2} \begin{pmatrix} l_2 & l_2 & 0 \\ m_2 & -m_2 & 0 \end{pmatrix} \\
&= \frac{(-1)^{-l_2-m_3}}{\sqrt{2l_2+1}}
\end{aligned}$$

When the size is 2, we simply use the two-term recursion formula with an arbitrary initial condition and normalize the two coefficients obtained.

$$\sum_{m1,m2} (2l_3+1) \begin{pmatrix} l_1 & l_2 & l_3 \\ m_1 & m_2 & m_3 \end{pmatrix}^2 = 1 \tag{C.28}$$

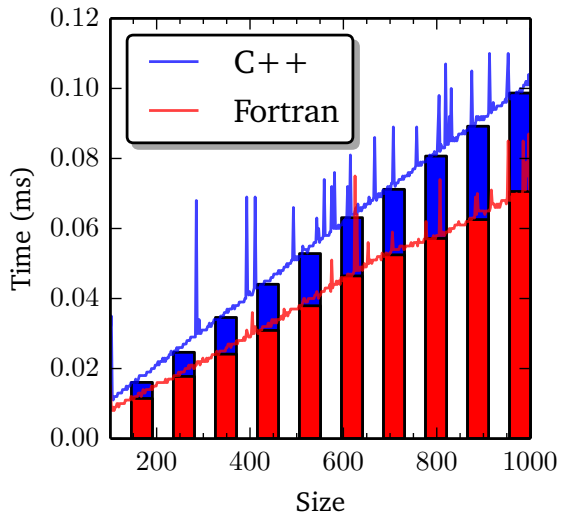

(a) Time (in ms) to compute sets of a given size of coupling coefficients, specifically the $3j$-symbol, in this case.

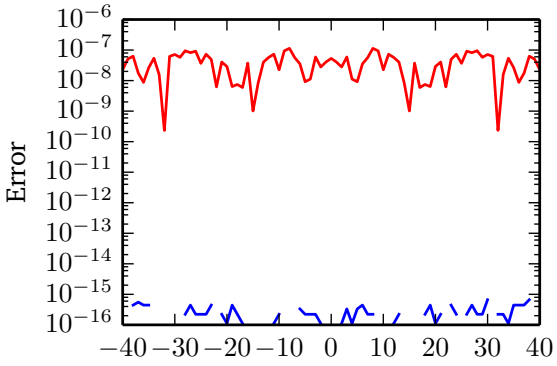

(b) Precision of the Fortran and C++ implementations of the algorithm obtainedby computing the orthogonality relationship (C.28).

Figure C.3 – Performance and precision of our numerical algorithms.

C.3 Spherical Harmonics Transform

In the variable phase method, we must find the spherical harmonics transform, i.e. the spherical moments, of the potential. To find these moments, we will have to become intimate with the spherical harmonics.

C.3.1 Definition of the scalar and vector spherical harmonics

While there is a number of ways to introduce the spherical harmonics, we will take the top to bottom approach: from the general to the specific. In all generality, spherical harmonics are solutions of the equation

$$\left[\nabla^2_\Omega + \ell(\ell+1)\right] Y^{\ell S}_{jm}(\theta,\varphi) = 0 \tag{C.29}$$

where $Y^{\ell S}_{jm}$ is actually a *tensor* spherical harmonic. It describes the angular distribution and polarization of spin-S particles with angular momentum j, projection m and orbital angular momentum ℓ [146]. While the study of particles with arbitrary spin S is interesting in its own right, we will concentrate on the case of particles of spin-1 and their scalar approximation (spin-0). Since the values of ℓ range from $|J-S|$ to $J+S$, the spin-0 case reduces to the usual scalar spherical harmonics while the spin-1 case are the *vector* spherical harmonics. As said in the main text, they can be formed by a superposition of scalar spherical harmonics of the form

$$\boldsymbol{Y}^{\ell}_{jm}(\theta,\varphi) = \sum_{m',\sigma} C^{jm}_{lm',1\sigma} Y^{m'}_{\ell}(\theta,\varphi)\hat{\boldsymbol{e}}_\sigma \tag{C.30}$$

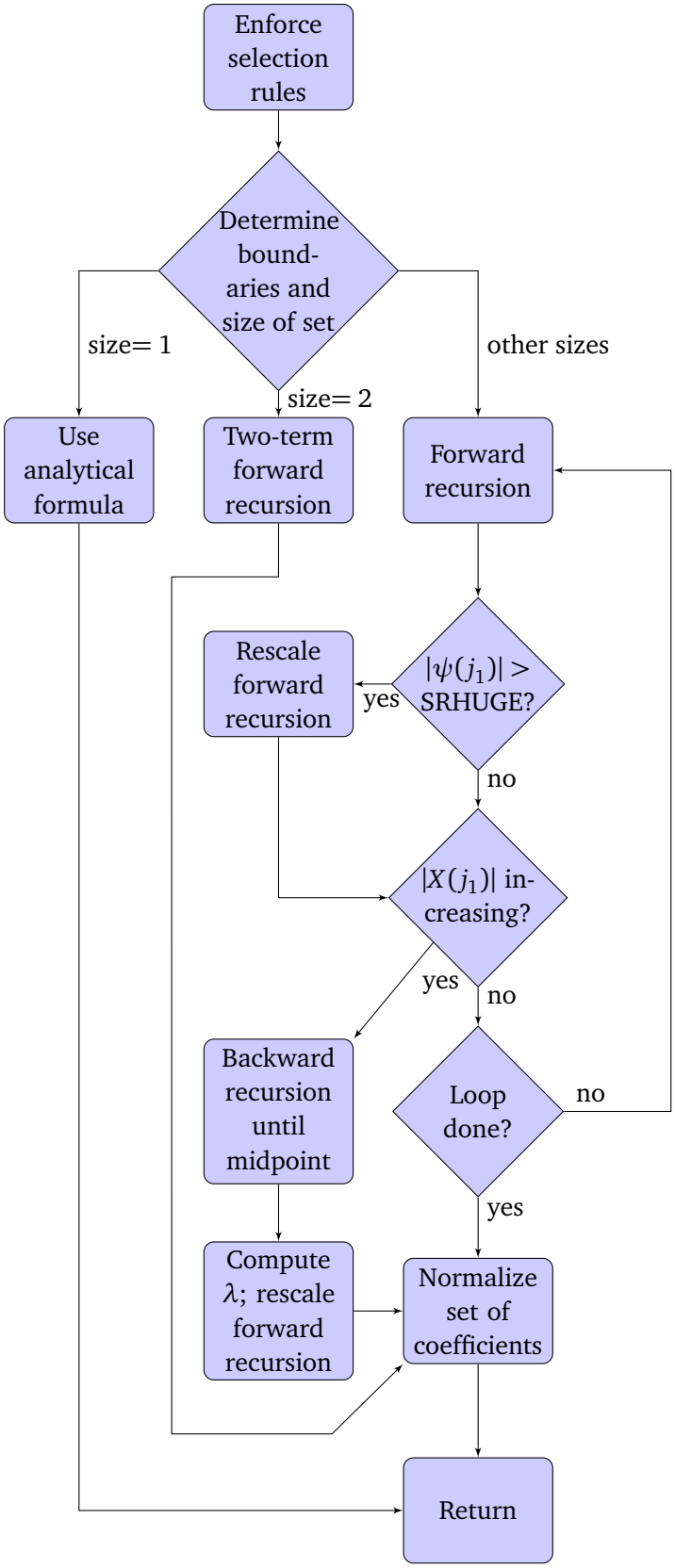

Figure C.4 – Flowchart of the algorithm used to compute the coupling coefficients. SRHUGE is the square root of the biggest representable number in our floating point representation.

Table C.1 – Parameters and coefficients of the three-term recursion relations satisfied by the $3j$- and $6j$-symbols. The expression $[++-]$ represents the coefficient $[j_1(j_1+1)+j_2(j_2+1)-j_3(j_3+1)]$ and similarly for other signs in the bracket.

$3j$- or $6j$-symbols	$f(j_1)=\begin{pmatrix} j_1 & j_2 & j_3 \\ m_1 & m_2 & m_3 \end{pmatrix}$	$h(j_1)=\begin{Bmatrix} j_1 & j_2 & j_3 \\ j_4 & j_5 & j_6 \end{Bmatrix}$
α_ψ	$j_1 A(j_1+1)$	$jE(j_1+1)$
β_ψ	$B(j_1)$	$F(j)$
γ_ψ	$(j_1+1)A(j_1)$	$(j_1+1)E(j)$
Functions	$A(j_1)=\left[j_1^2-(j_2-j_3)^2\right]^{1/2}$ $\times\left[(j_2+j_3+1)^2-j_1^2\right]^{1/2}$ $\times\left[j_1^2-m_1^2\right]^{1/2}$	$E(j_1)=\{\left[j_1^2-(j_2-j_3)^2\right]$ $\times\left[(j_2+j_3+1)^2-j_1^2\right]$ $\times\left[j_1^2-(j_5-j_6)^2\right]$ $\times\left[(j_5+j_6+1)^2-j_1^2\right]\}^{1/2}$
	$B(j_1)=-(2j_1+1)$ $\times[j_2(j_2+1)m_1$ $-j_3(j_3+1)m_1$ $-j_1(j_1+1)(m_3-m_2)]$	$F(j_1)=(2j_1+1)$ $\times\{j_1(j_1+1)[--+]$ $+j_5(j_5+1)[++-]$ $+j_6(j_6+1)[+-+]$ $-2j_1(j_1+1)l_1(l_1+1)\}$
Endpoints	$j_{1\min}=\max(\lvert j_2-j_3\rvert,\lvert m_1\rvert)$ $j_{1\max}=j_2+j_3$	$j_{1\min}=\max(\lvert j_2-j_3\rvert,\lvert j_5-j_6\rvert)$ $j_{1\max}=\min(j_2+j_3,j_5+j_6)$
Normalization	$\sum_{j_1}(2j_1+1)f(j_1)^2=1$	$(2j_4+1)\sum_{j_1}(2j_1+1)h(j_1)^2=1$
Sign	$\operatorname{sgn}[f(j_{1\max})]=(-1)^{j_2-j_3-m_1}$	$\operatorname{sgn}[h(j_{1\max})]=(-1)^{j_2+j_3+j_5+j_6}$

The numerical evaluation of these functions are then contingent on the evaluation of the scalar spherical harmonics and the Clebsch-Gordan coefficients. The first was covered in the previous appendix and we will soon tend to the second.

The scalar spherical harmonics can simply be written as

$$Y_\ell^m(\theta,\varphi)=P_\ell^m(\cos\theta)e^{im\varphi} \tag{C.31}$$

where P_ℓ^m is the normalized version of the associated Legendre polynomials [137]. They are related to the usual Legendre polynomials $\widetilde{P}_\ell^m$ through

$$P_\ell^m(x)=\sqrt{\frac{2\ell+1}{4\pi}\frac{(\ell-m)!}{(\ell+m)!}}\widetilde{P}_\ell^m(x) \tag{C.32}$$

To numerically evaluate the spherical harmonics, then, we must safely evaluate the associated Legendre polynomials. One of the only stable recurrence relation is [137]

$$P_\ell^m(x) = \sqrt{\frac{4l^2-1}{l^2-m^2}}\left[xP_{\ell-1}^m(x) - \sqrt{\frac{(l-1)^2-m^2)}{4(l-1)^2-1}}P_{\ell-2}^m(x)\right] \tag{C.33}$$

The initial conditions are provided by

$$P_m^m(x) = (-1)^m\sqrt{\frac{2m+1}{4\pi(2m)!}}(2m-1)!!(1-x^2)^{m/2} \tag{C.34}$$

$$P_{m+1}^m(x) = x\sqrt{2m+3}P_m^m(x) \tag{C.35}$$

At first sight, it might seem dangerous to evaluate $P_m^m(x)$ because of the division of two factorial functions. However, by taking the square of the expression and looking at the factorial functions, we have

$$a_m = \frac{[(2m-1)!!]^2}{(2m)!}. \tag{C.36}$$

This can evaluated rather simply by noting that $(2m-1)!! = {}^{(2m)!}/_{2^m m!}$. Rearranging, we get

$$a_m = \frac{(2m)!}{2^{2m}(m!)^2} = \frac{1}{2^{2m}}\binom{2m}{m}.$$

We further notice that

$$\frac{a_{m+1}}{a_m} = \frac{2^{2m}}{2^{2(m+1)}}\frac{\binom{2(m+1)}{m+1}}{\binom{2m}{m}} = \frac{2m+1}{2m+2}. \tag{C.37}$$

We can then safely evaluate $P_m^m(x)$ using the formula

$$P_m^m(x) = \sqrt{\frac{2m+1}{4\pi}\prod_{i=0}^{m-1}\frac{2i+1}{2i+2}(1-x^2)}. \tag{C.38}$$

Our numerical implementation shows machine precision for all spherical harmonics up to $\ell = 3$ (we compared the results of our algorithm with the analytical forms of the spherical harmonics). Moreover, we tested our algorithm against the following sums [146, §5.10]

$$\sum_m \left|Y_\ell^m(\theta,\varphi)\right|^2 = \frac{2\ell+1}{4\pi} \tag{C.39}$$

$$\sum_m m\left|Y_\ell^m(\theta,\varphi)\right|^2 = 0 \tag{C.40}$$

$$\sum_m m^2\left|Y_\ell^m(\theta,\varphi)\right|^2 = \frac{\ell(\ell+1)(2\ell+1)}{8\pi}\sin^2\theta. \tag{C.41}$$

They are verified to a precision of 10^{-7} up to $\ell = 500$. The uncertainty on the sums grows with ℓ. Figure C.5 tells us that the spherical harmonics are computed near to or at machine precision (in `double`). The increasing error is due to error accumulation. At large ℓ, there are a lot of terms to sum, thus increasing the absolute error made in the computation.

C.3.2 Spherical Harmonics Transform

While the Fast Fourier Transform has had hundreds of experts working on it, this is not true of the Fast Spherical Harmonics Transform. The program libraries are scarce and, for the most part, still in their infancy. This is in sharp contrast with the FFT case, where numerous libraries provide algorithms that performs FFTs at a cost of $\mathcal{O}(n \log n)$. `FFTW` is an example of such a mature, robust program library.

Any smooth function can be expanded in a spherical harmonics series (they form a complete basis on the 2-sphere) with [137, §6.7.1]

$$f(\theta, \varphi) = \sum_{\ell=0}^{\ell_{\max}} \sum_{m=-\ell}^{\ell} a_{\ell m} P_\ell^m(\cos\theta) e^{im\varphi} \tag{C.42}$$

Using the orthonormality conditions, we can find an expression for the expansion coefficients

$$a_{\ell m} = \iint_\Omega f(\theta, \varphi) e^{-im\varphi} P_\ell^m(\cos\theta) \sin\theta \, d\theta \, d\varphi \tag{C.43}$$

In the discrete case, then, the integral becomes a quadrature

$$a_{\ell m} = \sum_{i,j} w(\theta_i) f(\theta_i, \varphi_j) e^{-im\varphi_j} P_\ell^m(\cos\theta_i). \tag{C.44}$$

The fastest way to perform the quadrature over φ_j is, of course, to use the FFT. We will perform the quadrature over θ_i by using a Gauss-Legendre quadrature. While the cost of such an algorithm is the worst we could get ($\mathcal{O}(\ell^3)$), it is also the easiest to implement. Faster transforms are available in the literature [156–158].

To find the abscissas of the Gauss-Legendre quadrature (the roots of $P_\ell^0(\cos\theta)$), we perform a few rounds of Newton-Raphson using the following initial guess on the positions of the zeros [135]

$$\xi_{\ell,k} = \left(1 - \frac{1}{8\ell^2} + \frac{1}{8\ell^3}\right) \cos\left(\frac{4k-1}{4\ell+2}\pi\right) + \mathcal{O}\left(\ell^{-4}\right) \tag{C.45}$$

where $\xi_{\ell,k}$ is the kth root (ordered in $[-1, 1]$) of $P_\ell^0(\cos\theta)$.

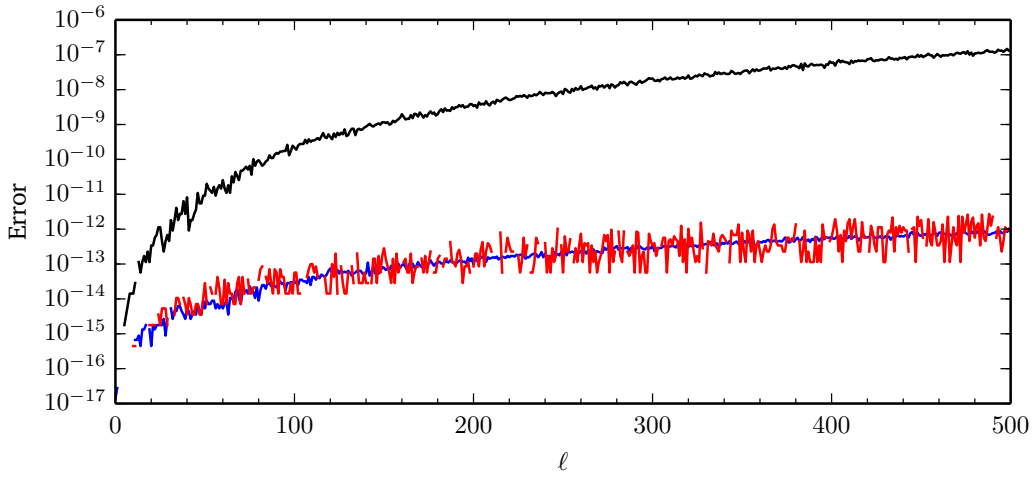

Figure C.5 – Precision of our implementation of the algorithm that evaluates the spherical harmonics. The blue curve corresponds to (C.39), the red curve to (C.40) and the black curve to (C.41).

Bibliography

[1] J.-L. Déziel, J. Dumont, D. Gagnon, L. J. Dubé, S. Messaddeq, and Y. Messaddeq, "Toward the formation of cross-superposed laser-induced periodic surface structures," (2014). arXiv:1410.0583.

[2] D. Gagnon, J. Dumont, J.-L. Déziel, and L. J. Dubé, "Optimization of integrated polarization filters," Opt. Lett. **39**, 5768 (2014).

[3] D. Gagnon, J. Dumont, J.-L. Déziel, and L. J. Dubé, "Ab initio investigation of lasing thresholds in photonic molecules," J. Opt. Soc. Am. B **31**, 1867 (2014).

[4] D. Gagnon, J. Dumont, and L. J. Dubé, "Multiobjective optimization in integrated photonics design," Opt. Lett. **38**, 2181 (2013).

[5] D. Gagnon, J. Dumont, and L. J. Dubé, "Beam shaping using genetically optimized two-dimensional photonic crystals," J. Opt. Soc. Am. A **29**, 2673–2678 (2012).

[6] D. Gagnon, J. Dumont, J.-L. Déziel, and L. J. Dubé, "Adding SALT to Coupled Microcavities: the making of active photonic molecule lasers," in "Proceedings of the 16th International Conference on Transparent Optical Networks," (ICTON 2014).

[7] G. Painchaud-April, J. Dumont, D. Gagnon, and L. J. Dubé, "**S** and **Q** Matrices Reloaded: applications to open, inhomogeneous, and complex cavities," in "Proceedings of the 15th International Conference on Transparent Optical Networks," (ICTON 2013).

[8] D. Gagnon, J. Dumont, and L. J. Dubé, "Coherent beam shaping using two-dimensional photonic crystals," in "Proceedings of the 15th Intertional Conference on Transparent Optical Networks," (ICTON 2013).

[9] D. Gagnon, J. Dumont, and L. J. Dubé, "Optimization in optical systems revisited: Beyond genetic algorithms," Bull. Am. Phys. Soc. **58** (2013).

[10] J. W. Strutt (Lord Rayleigh), *Theory of Sound*, vol. II (MacMillan, London, 1878).

[11] J. W. Strutt (Lord Rayleigh), "The Problem of the Whispering Gallagery," Philos. Mag. **20**, 1001–1004 (1910).

[12] O. Wright, “Gallery of whispers,” Phys. World pp. 31–36 (2012).

[13] Y. Yamamoto and R. E. Slusher, “Optical Processes in Microcavities,” Phys. Today **46**, 66 (1993).

[14] A. Serpengüzel, S. Arnold, and G. Griffel, “Excitation of resonances of microspheres on an optical fiber,” Opt. Lett. **20**, 654–656 (1995).

[15] F. Vollmer, D. Braun, A. Libchaber, M. Khoshsima, I. Teraoka, and S. Arnold, “Protein detection by optical shift of a resonant microcavity,” Appl. Phys. Lett. **80**, 4057 (2002).

[16] D. K. Armani, T. J. Kippenberg, S. M. Spillane, and K. J. Vahala, “Ultra-high-Q toroid microcavity on a chip,” Nature **421**, 925–8 (2003).

[17] F. Vollmer and S. Arnold, “Whispering-gallery-mode biosensing: label-free detection down to single molecules,” Nat. Methods **5**, 591–596 (2008).

[18] M. A. S. Cordoba, S. V. Boriskina, F. Vollmer, and M. C. Demirel, “Nanoparticle-based protein detection by optical shift of a resonant microcavity,” Appl. Phys. Lett. **99** (2011).

[19] R. Blümel and U. Smilansky, “Random-matrix description of chaotic scattering: Semiclassical approach,” Phys. Rev. Lett. **64**, 241–244 (1990).

[20] B. Batistić and M. Robnik, “Quantum localization of chaotic eigenstates and the level spacing distribution,” Phys. Rev. E **88**, 052913 (2013).

[21] S. Dutra and G. Nienhuis, “Quantized mode of a leaky cavity,” Phys. Rev. A **62**, 063805 (2000).

[22] S. M. Dutra and G. Nienhuis, “What Is a Quantized Mode of a Leaky Cavity?” in “Modern Challenges in Quantum Optics,” , vol. 575 of *Lecture Notes in Physics*, M. Orszag and J. C. Retamal, eds. (Springer, 2001), pp. 338–354.

[23] H. Türeci, “Modes of wave-chaotic dielectric resonators,” Prog. Opt. **47**, 75–137 (2005).

[24] M.-W. Kim, S. Rim, C.-H. Yi, and C.-M. Kim, “Chaos-assisted tunneling in a deformed microcavity laser,” Opt. Express **21**, 32508 (2013).

[25] S. Bittner, E. Bogomolny, B. Dietz, M. Miski-Oglu, P. Oria Iriarte, A. Richter, and F. Schäfer, “Experimental test of a trace formula for two-dimensional dielectric resonators,” Phys. Rev. E **81**, 066215 (2010).

[26] Y.-F. Xiao, X.-F. Jiang, Q.-F. Yang, L. Wang, K. Shi, Y. Li, and Q. Gong, “Chaos-induced transparency in an ultrahigh-Q optical microcavity,” (2012). arXiv:1209.4441.

[27] E. G. Altmann, J. S. E. Portela, and T. Tél, “Chaotic Systems with Absorption,” Phys. Rev. Lett. **111**, 144101 (2013).

[28] T.-Y. Kwon, S.-Y. Lee, J.-W. Ryu, and M. Hentschel, "Phase-space analysis of lasing modes in a chaotic microcavity," Phys. Rev. A **88**, 023855 (2013).

[29] J. Le Deunff, A. Mouchet, and P. Schlagheck, "Semiclassical description of resonance-assisted tunneling in one-dimensional integrable models," Phys. Rev. E **88**, 042927 (2013).

[30] C. Löbner, S. Löck, A. Bäcker, and R. Ketzmerick, "Integrable approximation of regular islands: The iterative canonical transformation method," Phys. Rev. E **88**, 062901 (2013).

[31] Y.-F. Xiao, X.-F. Jiang, Q.-F. Yang, L. Wang, K. Shi, Y. Li, and Q. Gong, "Tunneling-induced transparency in a chaotic microcavity," Laser Photon. Rev. **7**, L51–L54 (2013).

[32] G. D. Birkhoff, "On the periodic motions of dynamical systems," Acta Math. **50**, 359–379 (1927).

[33] M. Robnik, "Classical dynamics of a family of billiards with analytic boundaries," J. Phys. A. Math. Gen. **16**, 3971–3986 (1999).

[34] H.-W. Lee, "Theory and application of the quantum phase-space distribution functions," Phys. Rep. **259**, 147–211 (1995).

[35] W. H. Zurek, "Decoherence, einselection, and the quantum origins of the classical," Rev. Mod. Phys. **75**, 715–775 (2003).

[36] A. M. Armani, R. P. Kulkarni, S. E. Fraser, R. C. Flagan, and K. J. Vahala, "Label-Free, Single-Molecule Detection with Optical Microcavities," Science **317**, 783–787 (2007).

[37] J. Ward and O. Benson, "WGM microresonators: sensing, lasing and fundamental optics with microspheres," Laser Photon. Rev. **5**, 553–570 (2011).

[38] C. P. Dettmann, G. V. Morozov, M. Sieber, and H. Waalkens, "Unidirectional emission from circular dielectric microresonators with a point scatterer," Phys. Rev. A **80**, 063813 (2009).

[39] J.-W. Ryu, S.-Y. Lee, and S. Kim, "Coupled nonidentical microdisks: Avoided crossing of energy levels and unidirectional far-field emission," Phys. Rev. A **79**, 053858 (2009).

[40] W. D. Heiss, "The physics of exceptional points," J. Phys. A Math. Theor. **45**, 444016 (2012).

[41] S. Bittner, B. Dietz, H. L. Harney, M. Miski-Oglu, A. Richter, and F. Schäfer, "Scattering experiments with microwave billiards at an exceptional point under broken time-reversal invariance," Phys. Rev. E **89**, 032909 (2014).

[42] Q. Song, L. Ge, J. Wiersig, and H. Cao, "Formation of long-lived resonances in hexagonal cavities by strong coupling of superscar modes," Phys. Rev. A **88**, 023834 (2013).

[43] J. Unterhinninghofen, J. Wiersig, and M. Hentschel, "Goos-Hänchen shift and localization of optical modes in deformed microcavities," Phys. Rev. E **78**, 016201 (2008).

[44] J. Andreasen, A. A. Asatryan, L. C. Botten, M. A. Byrne, H. Cao, L. Ge, L. Labonté, P. Sebbah, A. D. Stone, H. E. Türeci, and C. Vanneste, "Modes of random lasers," Adv. Opt. Photonics **3**, 88 (2010).

[45] J. Ptasinski, S. W. Kim, L. Pang, I.-C. Khoo, and Y. Fainman, "Optical tuning of silicon photonic structures with nematic liquid crystal claddings." Opt. Lett. **38**, 2008–10 (2013).

[46] G. Painchaud-April, "Dielectric Cavities: Scattering Formalism and Applications," Ph. D. thesis, Université Laval. (2013).

[47] L. Novotny and B. Hecht, *Principles of Nano-Optics* (Cambridge University Press, 2012), 2nd ed.

[48] J. A. Stratton, *Electromagnetic Theory* (McGraw-Hill, 1941).

[49] J. D. Jackson, *Classical Electrodynamics* (John Wiley & Sons, 1962).

[50] D. Colton and R. Kress, *Inverse Acoustic and Electromagnetic Scattering Theory*, vol. 93 of *Applied Mathematical Sciences* (Springer, New York, 2013), 3rd ed.

[51] H. G. L. Schwefel, "Directionality and Vector Resonances of Regular and Chaotic Dielectric Microcavities," Ph. D. thesis, Yale University (2004).

[52] R. Dubertrand, E. Bogomolny, N. Djellali, M. Lebental, and C. Schmit, "Circular dielectric cavity and its deformations," Phys. Rev. A **77**, 013804 (2008).

[53] L. S. Rodberg and R. M. Thaler, *Introduction to the Quantum Theory of Scattering* (Academic Press, 1967).

[54] C. J. Joachain, *Quantum Collision Theory* (North-Holland, 1975).

[55] R. G. Newton, *Scattering Theory of Waves and Particles* (Springer-Verlag, New York, 1982), 2nd ed.

[56] L. Ge, Y. D. Chong, and A. D. Stone, "Steady-state ab initio laser theory: Generalizations and analytic results," Phys. Rev. A **82**, 063824 (2010).

[57] L. Ge, "Steady-state Ab Initio Laser Theory and its Applications in Random and Complex Media," Ph. D. thesis, Yale University (2010).

[58] F. T. Smith, "Lifetime Matrix in Collision Theory," Phys. Rev. **118**, 349–356 (1960).

[59] L. Eisenbud, "The Formal Properties of Nuclear Collisions," Ph. D. thesis, Princeton University (1948).

[60] H. Nussenzveig, "Time Delay in Quantum Scattering," Phys. Rev. D **6**, 1534–1542 (1972).

[61] C. A. A. de Carvalho and H. M. Nussenzveig, "Time delay," Phys. Rep. **364**, 83–174 (2002).

[62] H. M. Nussenzveig, "Time delay in electromagnetic scattering," Phys. Rev. A **55**, 1012–1019 (1997).

[63] H. Haberzettl and R. Workman, "Time delay in a multichannel formalism," Phys. Rev. C **76**, 058201 (2007).

[64] P. A. Martin, "Scattering theory with dissipative interactions and time delay," Nuovo Cim. B **30**, 217–238 (1975).

[65] E. C. Le Ru, W. R. C. Somerville, and B. Auguié, "Radiative correction in approximate treatments of electromagnetic scattering by point and body scatterers," Phys. Rev. A **87**, 012504 (2013).

[66] J. Muga, J. Palao, B. Navarro, and I. Egusquiza, "Complex absorbing potentials," Phys. Rep. **395**, 357–426 (2004).

[67] I. Shimamura, "Complete separation of resonance and nonresonance channel spaces," J. Phys. B: At. Mol. Opt. Phys. **44**, 201002 (2011).

[68] I. Shimamura, "Chapter 4 – Quasi-Bound States of Electronic and Positronic Few-Body Systems: Analysis of Multichannel Scattering Information," Adv. Quantum Chem. **63**, 165—-245 (2012).

[69] M. Simonius, "Overlapping resonances and unitarity of the scattering matrix," Nucl. Phys. A **218**, 53–60 (1974).

[70] D. Savin and H.-J. Sommers, "Delay times and reflection in chaotic cavities with absorption," Phys. Rev. E **68**, 036211 (2003).

[71] Y. V. Fyodorov, D. V. Savin, and H.-J. Sommers, "Scattering, reflection and impedance of waves in chaotic and disordered systems with absorption," J. Phys. A. Math. Gen. **38**, 10731–10760 (2005).

[72] S. Joffily, "Poles of the S-matrix for a complex potential," Nucl. Phys. A **215**, 301–313 (1973).

[73] L. Kok and H. van Haeringen, "On the theory of complex potential scattering," Ann. Phys. (N. Y). **131**, 426–450 (1981).

[74] W. Cassing and M. Stingl, "Scattering with absorptive interaction," Phys. Rev. C **26**, 22–33 (1982).

[75] A. I. Rahachou and I. V. Zozoulenko, "Scattering Matrix Approach to the Resonant States and Q Values of Microdisk Lasing Cavities," Appl. Opt. **43**, 1761–1772 (2004).

[76] M. Greenberg, *Advanced Engineering Mathematics* (Pearson, 1998).

[77] C. D. Meyer, *Matrix Analysis and Applied Linear Algebra* (SIAM: Society for Industrial and Applied Mathematics, 2001).

[78] D. Jackson, "On the Order of Magnitude of the Coefficients in Trigonometric Interpolation," Trans. Am. Math. Soc. **21**, 321–321 (1920).

[79] M. Hentschel and K. Richter, "Quantum chaos in optical systems: The annular billiard," Phys. Rev. E **66**, 056207 (2002).

[80] M. I. Mishchenko, L. D. Travis, and A. A. Lacis, *Scattering, Absorption and Emission of Light by Small Particles* (Cambridge University Press, 2002), 3rd ed.

[81] H. E. Türeci, "Wave Chaos in Dielectric Resonators : Asymptotic and Numerical Approaches," Ph. D. thesis, Yale University (2003).

[82] D. Gagnon, "Modélisation ondulatoire de structures optiques résonantes: Application aux microcavités diélectriques bidimensionnelles," Master's thesis, Université Laval (2011).

[83] S. Bittner, E. Bogomolny, B. Dietz, M. Miski-Oglu, and A. Richter, "Experimental Observation of Localized Modes in a Dielectric Square Resonator," p. 5 (2013).

[84] W.-H. Guo, Y.-Z. Huang, Q.-Y. Lu, and L.-J. Yu, "Whispering-gallery-like modes in square resonators," IEEE J. Quantum Electron. **39**, 1106–1110 (2003).

[85] S.-Y. Lee, M. Kurdoglyan, S. Rim, and C.-M. Kim, "Resonance patterns in a stadium-shaped microcavity," Phys. Rev. A **70**, 023809 (2004).

[86] J. U. Nöckel, "Resonances in nonintegrable open systems," Ph. d. thesis, Yale University (1997).

[87] H. G. L. Schwefel, N. B. Rex, H. E. Tureci, R. K. Chang, A. D. Stone, T. Ben-Messaoud, and J. Zyss, "Dramatic shape sensitivity of directional emission patterns from similarly deformed cylindrical polymer lasers," J. Opt. Soc. Am. B **21**, 923 (2004).

[88] T. Hisch, M. Liertzer, D. Pogany, F. Mintert, and S. Rotter, "Pump-Controlled Directional Light Emission from Random Lasers," Phys. Rev. Lett. **111**, 023902 (2013).

[89] F.-J. Shu, C.-L. Zou, and F.-W. Sun, "An Optimization Method of Asymmetric Resonant Cavities for Unidirectional Emission," J. Light. Technol. **31**, 2994–2998 (2013).

[90] H. Kwak, Y. Shin, S. Moon, and K. An, "Observation of resonance-assisted dynamical tunneling in an asymmetric microcavity," (2013). arXiv:1305.6019.

[91] B. Schutz, *A First Course in General Relativity* (Cambridge University Press, 2009), 2nd ed.

[92] V. A. Toponogov, *Differential Geometry of Curves and Surfaces: A Concise Guide* (Birkhäuser, 2005).

[93] M. Hentschel and H. Schomerus, "Fresnel laws at curved dielectric interfaces of microresonators," Phys. Rev. E **65**, 045603 (2002).

[94] S. Saïdi, "Étude d'une nouvelle classe de billards inhomogènes et son apport aux microcavités laser," Ph. D. thesis, Université Pierre et Marie Curie Paris 6 (2005).

[95] Y. D. Chong and A. D. Stone, "General Linewidth Formula for Steady-State Multimode Lasing in Arbitrary Cavities," Phys. Rev. Lett. **109**, 063902 (2012).

[96] R. W. Boyd, *Nonlinear Optics* (Academic Press, 2003), 2nd ed.

[97] R. W. Boyd, *Nonlinear Optics* (Academic Press, 2008), 3rd ed.

[98] H. Haken, *Light*, vol. 2 (North-Holland, 1985).

[99] S. Esterhazy, D. Liu, M. Liertzer, A. Cerjan, L. Ge, K. G. Makris, A. D. Stone, J. M. Melenk, S. G. Johnson, and S. Rotter, "A scalable numerical approach for the Steady-State Ab-Initio Laser Theory," (2013). arXiv:1312.2488.

[100] I. Gohberg and S. Goldberg, *Basic Operator Theory* (Birkhäuser, Boston, 1981).

[101] M. Catrysse, R. Puers, C. Hertleer, L. Van Langenhove, H. van Egmond, and D. Matthys, "Towards the integration of textile sensors in a wireless monitoring suit," Sensors Actuators A Phys. **114**, 302–311 (2004).

[102] M. I. Jais, M. F. Jamlos, M. Jusoh, T. Sabapathy, and M. R. Kamarudin, "A Novel Beam Steering of Hybrid Switchable Beam Textile Antenna," Microw. Opt. Technol. Lett. **55**, 1893–1897 (2013).

[103] R. S. Elliott, *Antenna Theory and Design*, IEEE Press Series on Electromagnetic Wave Theory (Wiley-Interscience, 2003).

[104] "Std. 145-1993," IEEE Stand. Defin. Terms Antennas. p. 40 (1993).

[105] P. P. Delogne and A. A. Laloux, "Theory of the Slotted Coaxial Cable," IEEE Trans. Microw. Theory Tech. **28**, 1102–1107 (1980).

[106] J. H. Wang and K. K. Mei, "Theory and analysis of leaky coaxial cables with periodic slots," IEEE Trans. Antennas Propag. **49**, 1723–1732 (2001).

[107] D. H. Kim and H. J. Eom, "Radiation of a Leaky Coaxial Cable With Narrow Transverse Slots," IEEE Trans. Antennas Propag. **55**, 107–110 (2007).

[108] G. Addamo, R. Orta, and R. Tascone, "Bloch wave analysis of long leaky coaxial cables," IEEE Trans. Antennas Propag. **56**, 1548–1554 (2008).

[109] C. R. Paul, *Analysis of Multiconductor Transmission Lines* (Wiley, 2007), 2nd ed.

[110] H. Shigesawa and M. Tsuji, "A new equivalent network method for analyzing discontinuity properties of open dielectric waveguides," IEEE Trans. Microw. Theory Tech. **37**, 3–14 (1989).

[111] D. K. Cheng, *Field and Wave Electromagnetics* (Addison-Wesley, 1989), 2nd ed.

[112] K. Mitzner, "Effective boundary conditions for reflection and transmission by an absorbing shell of arbitrary shape," IEEE Trans. Antennas Propag. **16**, 706–712 (1968).

[113] J. van Bladel, *Singular Electromagnetic Fields and Sources* (Oxford University Press, New York, 1991).

[114] P. A. Martin, "Acoustic Scattering by Inhomogeneous Obstacles," SIAM J. Appl. Math. **64**, 297–308 (2003).

[115] A. F. Oskooi, D. Roundy, M. Ibanescu, P. Bermel, J. Joannopoulos, and S. G. Johnson, "Meep: A flexible free-software package for electromagnetic simulations by the FDTD method," Comput. Phys. Commun. **181**, 687–702 (2010).

[116] J.-P. Berenger, "A perfectly matched layer for the absorption of electromagnetic waves," J. Comput. Phys. **114**, 185–200 (1994).

[117] A. Konrad, "Vector Variational Formulation of Electromagnetic Fields in Anisotropic Media," Microw. Theory Tech. IEEE Trans. **24**, 553–559 (1976).

[118] M. Koshiba, K. Hayata, and M. Suzuki, "Vectorial finite-element method without spurious solutions for dielectric waveguide problems," Electron. Lett. **20**, 409–410 (1984).

[119] M. Koshiba, K. Hayata, and M. Suzuki, "Improved Finite-Element Formulation in Terms of the Magnetic Field Vector for Dielectric Waveguides," Microw. Theory Tech. IEEE Trans. **33**, 227–233 (1985).

[120] G. Hower, R. Olsen, J. Earls, and J. Schneider, "Inaccuracies in numerical calculation of scattering near natural frequencies of penetrable objects," IEEE Trans. Antennas Propag. **41**, 982–986 (1993).

[121] A. Hoekstra, J. Rahola, and P. Sloot, "Accuracy of Internal Fields in Volume Integral Equation Simulations of Light Scattering," Appl. Opt. **37**, 8482 (1998).

[122] S. V. Boriskina, P. Sewell, T. M. Benson, and A. I. Nosich, "Accurate simulation of two-dimensional optical microcavities with uniquely solvable boundary integral equations and trigonometric Galerkin discretization," J. Opt. Soc. Am. A **21**, 393 (2004).

[123] M. Oxborrow, "Traceable 2-D Finite-Element Simulation of the Whispering-Gallery Modes of Axisymmetric Electromagnetic Resonators," IEEE Trans. Microw. Theory Tech. **55**, 1209–1218 (2007).

[124] M. I. Cheema and A. G. Kirk, "Accurate determination of the quality factor and tunneling distance of axisymmetric resonators for biosensing applications." Opt. Express **21**, 8724–35 (2013).

[125] R. Blümel and U. Smilansky, "Classical irregular scattering and its quantum-mechanical implications," Phys. Rev. Lett. **60**, 477–480 (1988).

[126] R. Jalabert, H. Baranger, and A. Stone, "Conductance fluctuations in the ballistic regime: A probe of quantum chaos?" Phys. Rev. Lett. **65**, 2442–2445 (1990).

[127] R. Landauer, "Electrical conductivity in inhomogeneous media," AIP Conference Proceedings **40**, 2–45 (1978).

[128] K. Fuchs, "The conductivity of thin metallic films according to the electron theory of metals," Math. Proc. Cambridge Philos. Soc. **34**, 100–108 (1938).

[129] E. Sondheimer, "The mean free path of electrons in metals," Adv. Phys. **1**, 1–42 (1952).

[130] J. Purswani and D. Gall, "Electron scattering at single crystal Cu surfaces," Thin Solid Films **516**, 465–469 (2007).

[131] B. Curran, "Loss Modeling in Non-Ideal Transmission Lines for Optimal Signal Integrity," Ph. D. thesis, Technischen Universität Berlin (2012).

[132] T. S. Kuhn, *The Structure of Scientific Revolutions* (University of Chicago Press, 1996), 3rd ed.

[133] C. Sanderson, "Armadillo: An Open Source C++ Linear Algebra Library for Fast Prototyping and Computationally Intensive Experiments." Technical report (2010).

[134] M. Geissbuehler and T. Lasser, "How to display data by color schemes compatible with red-green color perception deficiencies." Opt. Express **21**, 9862–74 (2013).

[135] M. Abramowitz and I. A. Stegun, *Handbook of Mathematical Functions* (Dover Publications, 1965).

[136] A. Cuyt, V. B. Petersen, B. Verdonk, H. Waadeland, and W. B. Jones, *Handbook of Continued Fractions for Special Functions* (Springer, 2008).

[137] W. H. Press, S. A. Teukolsky, W. T. Vetterling, and B. P. Flannery, *Numerical Recipes : the Art of Scientific Computing* (Cambridge University Press, 2007), 3rd ed.

[138] J. Stoer and R. Bulirsch, *Introduction to Numerical Analysis* (Springer, 2002).

[139] J. Wiersig, "Boundary element method for resonances in dielectric microcavities," J. Opt. A Pure Appl. Opt. **5**, 53–60 (2003).

[140] L. M. Delves and J. L. Mohamed, *Computation Methods for Integral Equations* (Cambridge University Press, 1985).

[141] E. N. Economou, *Green's Functions in Quantum Physics* (Springer, 2006), 3rd ed.

[142] A. Ben-Menahem and S. J. Singh, "Eigenvector Expansions of Green's Dyads with Applications to Geophysical Theory," Geophys. J. Int. **16**, 417–452 (1968).

[143] A. Yaghjian, "Electric dyadic Green's functions in the source region," Proc. IEEE **68**, 248–263 (1980).

[144] J. R. de Lasson, J. Mø rk, and P. T. s. Kristensen, "Three-dimensional integral equation approach to light scattering, extinction cross sections, local density of states, and quasi-normal modes," J. Opt. Soc. Am. B **30**, 1996 (2013).

[145] M. Fall, S. Boutami, A. Glière, B. Stout, and J. Hazart, "Multilevel fast multipole method based on a potential formulation for 3D electromagnetic scattering problems," J. Opt. Soc. Am. A **30**, 1273 (2013).

[146] D. A. Varshalovich, A. N. Moskalev, and V. K. Khersonskii, *Quantum Theory of Angular Momentum: Irreducible Tensors, Spherical Harmonics, Vector Coupling Coefficients, 3nj Symbols* (World Scientific, 1988).

[147] D. E. Amos, "Algorithm 644: A portable package for Bessel functions of a complex argument and nonnegative order," ACM Trans. Math. Softw. **12**, 265–273 (1986).

[148] N. M. Temme, "The numerical computation of the confluent hypergeometric function $U(a,b,z)$," Numer. Math. **41**, 63–82 (1983).

[149] I. Thompson and A. Barnett, "Coulomb and Bessel functions of complex arguments and order," J. Comput. Phys. **64**, 490–509 (1986).

[150] D. M. Brink and G. R. Satchler, *Angular Momentum* (Oxford University Press, 1993), 3rd ed.

[151] C. Cohen-Tannoudji, B. Diu, and F. Laloë, *Mécanique quantique*, vol. 2 (Hermann, 1973).

[152] A. P. Yutsis, I. B. Levinson, and V. V. Vanagas, *Mathematical Apparatus of the Theory of Angular Momentum* (Israel Program for Scientific Translations, Jerusalem, 1962).

[153] K. Schulten, "Exact recursive evaluation of 3j- and 6j-coefficients for quantum-mechanical coupling of angular momenta," J. Math. Phys. **16**, 1961 (1975).

[154] K. Schulten and R. Gordon, “Recursive evaluation of 3j and 6j coefficients,” Comput. Phys. Commun. **11**, 269–278 (1976).

[155] J. Luscombe and M. Luban, “Simplified recursive algorithm for Wigner 3j and 6j symbols,” Phys. Rev. E **57**, 7274–7277 (1998).

[156] V. Rokhlin and M. Tygert, “Fast Algorithms for Spherical Harmonic Expansions,” SIAM J. Sci. Comput. **27**, 1903–1928 (2006).

[157] M. Tygert, “Fast algorithms for spherical harmonic expansions, II,” J. Comput. Phys. **227**, 4260–4279 (2008).

[158] M. Tygert, “Fast algorithms for spherical harmonic expansions, III,” J. Comput. Phys. **229**, 6181–6192 (2010).

[159] J. P. Crutchfield, “The dreams of theory,” WIREs Comput. Stat. **6**, 75–79 (2014).

Index